# Systematic analysis of the crystal structure, chemical ordering, and microstructure of Ni–Mn–Ga ferromagnetic shape memory alloys

by

Marc Louis Richard

Submitted to the Department of Materials Science and Engineering
in partial fulfillment of the requirements for the degree of

Doctor of Science in Metallurgy

at the

MASSACHUSETTS INSTITUTE OF TECHNOLOGY

September 2005

Author . . . . . . . . . . . . . . . . . . . . . . . . . . . . . . . . . . . . . . . . . . . . . . . . . . . . . . . . . .
Department of Materials Science and Engineering
August 31, 2005

Certified by . . . . . . . . . . . . . . . . . . . . . . . . . . . . . . . . . . . . . . . . . . . . . . . . . . . . . .
Samuel M. Allen
POSCO Professor of Physical Metallurgy
Thesis Supervisor

Certified by . . . . . . . . . . . . . . . . . . . . . . . . . . . . . . . . . . . . . . . . . . . . . . . . . . . . . .
Robert C. O'Handley
Senior Research Scientist
Thesis Supervisor

Accepted by . . . . . . . . . . . . . . . . . . . . . . . . . . . . . . . . . . . . . . . . . . . . . . . . . . . . . .
Gerbrand Ceder
R.P. Simmons Professor of Materials Science and Engineering
Chair, Departmental Committee on Graduate Students

# Systematic analysis of the crystal structure, chemical ordering, and microstructure of Ni–Mn–Ga ferromagnetic shape memory alloys

by

Marc Louis Richard

Submitted to the Department of Materials Science and Engineering
on August 31, 2005, in partial fulfillment of the
requirements for the degree of
Doctor of Science in Metallurgy

## Abstract

Ni–Mn–Ga based ferromagnetic shape-memory alloys (FSMAs) have shown great promise as an active material that yields a large output strain over a range of actuation frequencies. The maximum strain has been reported to be 6% in the tetragonal martensitic phase and up to 10% in the orthorhombic phase. There has been a large body of work exploring the engineering properties of these alloys but less extensive work in the understanding of the underlying structure and its connection to the material properties. This is particularly true for the off-stoichiometry compositions that are of most practical interest.

The crystal structure of Ni-Mn-Ga ferromagnetic shape-memory alloys is extremely sensitive to composition. Several martensitic structures including tetragonal (5-layer), orthorhombic (7-layer) and non-modulated tetragonal have been identified. A systematic exploration of the composition-structure relationship has been performed using x-ray diffraction on samples taken from several single crystals with different compositions. A room temperature phase diagram has been constructed delineating the fields where the tetragonal and orthorhombic martensites are found.

Temperature-dependent magnetic and x-ray measurements have revealed markedly different transformation behavior in the tetragonal and orthorhombic materials. The orthorhombic material shows a much larger difference between the martensite start and finish temperatures as compared to tetragonal martensite. The observed difference in transformation behavior has been shown not to be related to composition inhomogeneity or the presence of intermediate martensitic phases. A thermodynamic model is proposed to explain the differences in the transition behavior by including strain energy effects in the two martensite phases that may arise during the transformation.

Single-crystal and powder neutron diffraction have been employed to study for the first time the chemical ordering in the austenite and martensite phases in off-stoichiometric alloy compositions. A comparison of compositions with close to 50 at%

Ni and those further from stoichiometry revealed the need for a more complex model for the site occupancy in alloys with a significant excess or deficiency of Ni.

The microstructure of several different Ni–Mn–Ga alloys was analyzed using transmission electron microscopy providing new microstructural data that has not been shown elsewhere. The superstructures of the different compositions has been confirmed, complementing the x-ray measurements. A hierarchal twin structure has been observed along with several second-phase particles resulting from impurities. The composition and source of the impurities has been analyzed. The twin-boundary pinning strength of the second phase particles has been estimated using the Orowan approach. This information can be used to understand why certain crystals with weak pinning sites show field-induced strain while others with very strong defect strengths do not show any actuation under an applied magnetic field.

Thesis Supervisor: Samuel M. Allen
Title: POSCO Professor of Physical Metallurgy

Thesis Supervisor: Robert C. O'Handley
Title: Senior Research Scientist

# Acknowledgments

I would first like to thank both of my advisors, Samuel M. Allen and Robert C. O'Handley for their continued support throughout my stay at MIT. They provided excellent guidance in the development of my thesis research project and were always supportive in my desire to gain teaching experience. From the beginning of my time here they strived to ensure my experience at MIT was tailored towards my future professional goals. I will always be extremely grateful for their advice, guidance, and encouragement. Many thanks to my thesis committee as well, Professors John Vander Sande and Bernhardt Wuensch. They both provided excellent advice in preparing my thesis and helped my improve the presentation and explanation of my research results.

I must also thanks many of the current and past member of the Magnetic Materials group at MIT. Jorge Feuchtwanger was always willing to help me with my machining needs and our conversations were always a valuable tool in exploring our common research interests. Without his help, along with Brad Peterson, my microscopy work would have been delayed significantly. Miguel Marioni was always willing to share some of his extensive research experience and saved me countless hours of heading down the wrong path in the lab. David Bono was always willing to stop what he was doing to help me with the construction of electronics and was a great teacher in the process. David Paul was always only a short walk away and our frequent conversations were always quite valuable. I was also lucky to work with two excellent undergraduate students, Joanna Natsios and Marc Fernandes who allowed me to teach them about our research while they assisted with some of my work as well. I was also quite fortunate to work with some of our visitors from other institutions, including: Professor Jose M. Barandiaran, Dr. Xue-Jun Jin, Dr. Pablo Garcia Tello, and Dr. Kee Ahn Lee. Their experience and insight were invaluable part of our group and my research project as well. I would also like to thank the other members of our group: Josh Chambers, Ratchatee Techapiesancharoenkij, Jesse Simon, Zil Lyons, Chirs Henry, and Steve Murray.

I also would like to acknowledge the help of many of the technical staff in the various labs and centers I had the privilege to work in during my stay at MIT. Michael Frongillo in the CMSE Electron Microscopy facility was always willing to help and his training on the various microscopes at MIT was extremely valuable. It was always enjoyable to work with Mike and hear his many stories about his experiences at MIT and beyond. I would also like to thank Dr. Anthony Garratt-Reed, also in the CMSE microscopy facility, who assisted in the operation of the STEM and helped with the fine-scale composition analysis that is an important component of my thesis research. Joe Adario and Yin-Lin Xie deserve a great deal of thanks for their help in the training and operation of equipment which I used during my thesis research. I was very fortunate to have the opportunity to work with Dr. Virgil Solomon and Professor David Smith at Arizona State University. I am grateful for the time they spent helping me with high-resolution electron microscopy. I would also like to thank Toby Bashaw for all his help with my work in the foundry. I have learned a great deal about metal casting from Toby and will always be grateful for the time he spent with me, especially on the DMSE medallion casting project.

I was very lucky to have had the opportunity to be involved in the teaching with many different faculty in our department. I would like to thank them all for the opportunity to work with them and for all they were able to teach me: Sam Allen, Craig Carter, Gerbrand Ceder, Donald Sadoway, and Bernhardt Wuensch. I would like to thank Professors Heather Lechtman and Dorothy Hosler, along with Dr. Elizabeth Hendrix for introducing me to materials research in archeology and for allowing me to work in the CMRAE performing research on ancient Moche artifacts. I am extremely grateful for all their help in helping this metallurgist quickly come up to speed on some of the basics of archeological research.

I would also like to acknowledge the financial support which has enabled me to study and perform research over the past 6 years at MIT. The chart on the following page details the groups I owe thanks to for their support: the Materials Science Department, MIT, and the Office of Naval Research (ONR MURI N00014-01-10758). Also, I wanted to include a pie chart somewhere in my thesis and this was my sole opportunity to do so.

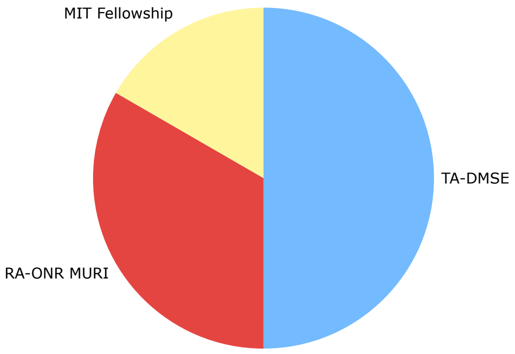

Finally, I would never have been able to complete this work without the continued support of my family, especially my parents, my brothers Stephen, Jeffrey, and Marc, and of course my partner Matthew. Although they knew little of what this mad scientist was doing in the lab all day, they were always there for me, especially when things were not going well. They were always there to pick me up and help me remember things would always get better.

# Contents

# List of Figures

# List of Tables

# Chapter 1

# Introduction

## 1.1 Active materials

Active materials respond mechanically to applied external fields. The energy input can be in the form of an electric field, a magnetic field, or heat. Piezoelectrics (ex: PZT) are a class of active materials that respond to an applied electric field through the motion of ions away from their equilibrium positions resulting a macroscopic shape change [15, 16]. Under an applied magnetic field, magnetostrictive materials (ex: Terfenol-D) produce a strain output through the coupling of the crystal structure and the magnetization orientation [17]. Piezoelectrics and magnetostrictive materials yield small output strains of about 0.1–0.2% but can function over a large frequency range.

Materials that exhibit the shape-memory effect comprise another important class of active materials. The main phenomenon behind the thermoelastic shape-memory effect, also known as the conventional shape-memory effect, is martensitic transformation (Figure 1-1). At high temperatures, these materials are in a higher symmetry phase, termed austenite. Upon reaching the martensite start temperature, $T_m^s$, the material transforms into the lower symmetry martensitic phase. In those martensites that favor deformation by twinning it is possible for several different variants of martensite to form, each with a different crystallographic orientation. However, unless some other outside force biases the system, the variant distribution is random.

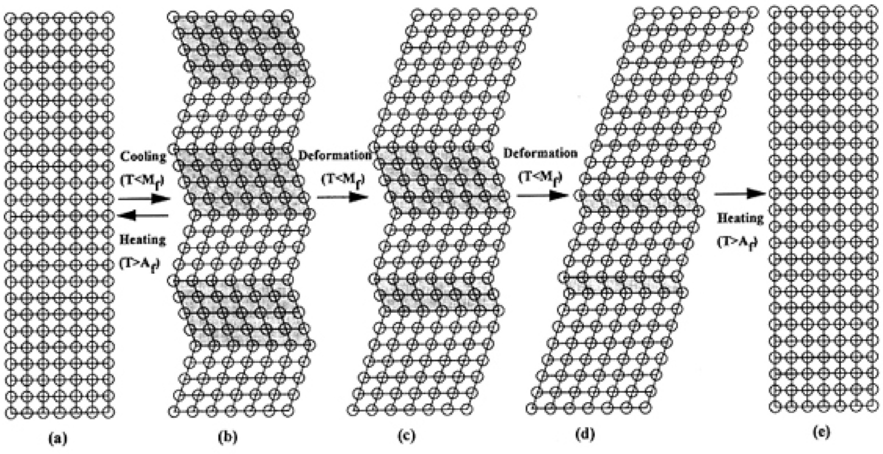

Figure 1-1: Mechanism of the thermoelastic shape memory effect. (a) Original parent crystal (austenite), (b) transformation into martensite, (c,d) deformation in the martensitic phase, (e) transformation back to austenite and original shape. From Otsuka et al. [1]

Thus the gross shape is retained when going from austenite to martensite. When the material is deformed in the martensitic phase, the twin boundaries move to accommodate the applied stress. Upon re-heating, the material returns to the original shape in the austenite phase. This is the one-way shape-memory effect (SME). Some martensites exhibit a two-way SME in which cooling back to the marteniste restores the deformation that was erased on heating to austenite.

Conventional shape-memory alloys are attractive active materials due to the large strain which accompanies the martensitic transition. Strains on the order of 10 percent are possible depending on the particular material being used [1, 18]. However, a temperature change is needed in order to achieve the phase transformation and obtain the desired output strain. Due to the slow kinetics of this type of driving mechanism the response frequency of conventional shape-memory alloys is limited; this reduces the number of potential applications.

As a recent addition to this class of active materials, ferromagnetic shape-memory alloys (FSMA) are being studied intensively due to the large output strain and frequency response possible. Unlike thermoelastic shape-memory alloys, the magnetic shape-memory effect occurs entirely in the martensitic state through the reorganization of martensitic twin variants (see Section 1.4). Only two alloy systems have demonstrated field-induced strain, 0.5% in Fe–Pd [19] and 6–10% in Ni–Mn–Ga, with the majority of research focused on the Ni–Mn–Ga due to the larger strains possible and the absence of expensive elements like Pd. Other alloys systems, such as Co–Ni–Ga [20], Ni–Fe–Ga [21], and Co–Ni–Al [22], have been studied but have yet to show any magnetic field-induced strain.

## 1.2 Development of Ni–Mn–Ga Ferromagnetic Shape-Memory Alloys

Ullakko [23, 24] and James [25] first described the possibility of obtaining magnetic field-induced strain from Ni–Mn–Ga alloys. These alloys exhibited both a martensitic transformation and ferromagnetism. By replacing the need for heat flow to induce a transformation by the application of a magnetic field, the upper-bound for actuation frequency would be greatly increased. Ullakko [24, 26] and Murray [27] were the first to demonstrate 0.2% magnetic field-induced strain in single crystals of $Ni_2MnGa$ in the martensitic phase.

Since the initial demonstration of the possibility of field-induced actuation, the maximum output strain achieved has increased from the original 0.2% to 6%, which is close to the theoretical maximum dictated by the tetragonal crystal structure [3, 28]. Also, compositions were adjusted to high Mn content in place of Ga in order to have the martensitic phase stable at room temperature, removing the need to cool samples to below 0°C to achieve magnetic-field actuation. More recently Sozinov [29, 30] and Mullner [31] have reported strains of close to 10% in alloy compositions exhibiting the orthorhombic martensitic phase. Despite intense research activity aimed at testing the potential engineering application of FSMAs, there is relatively little structural and microstructural data in the literature, particularly on the technically important off-stoichiometric compositions.

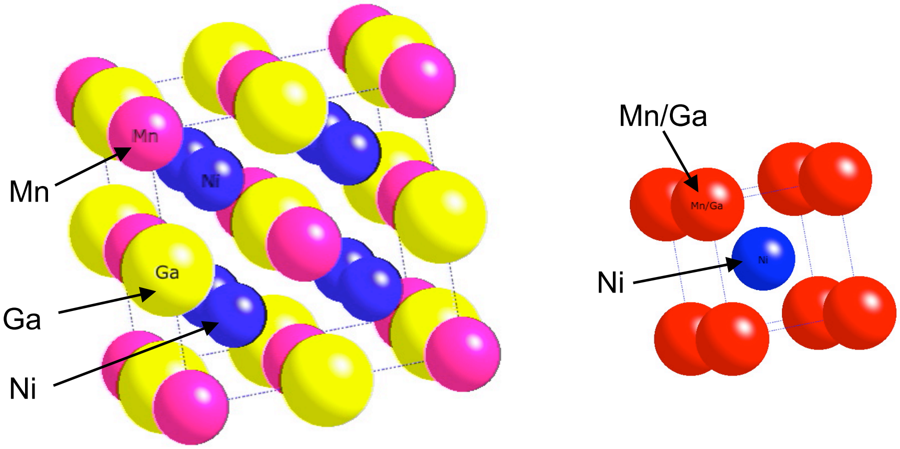

(a) (b)

Figure 1-2: Model of the (a) cubic ($Fm\overline{3}m$) austenite structure showing $L2_1$ ordering and the (b) $B2$ structure with $Pm\overline{3}m$ symmetry.

## 1.3 Ni–Mn–Ga Crystal Structure

$Ni_2MnGa$ is an intermetallic compound that displays the Heusler structure [32]. The austenite phase, which exists at room temperature for the stoichiometric composition, exhibits $Fm\overline{3}m$ symmetry with $L2_1$[1] chemical ordering as shown in Figure 1-2a [12]. At temperatures above approximately 800°C, Mn and Ga atoms become disordered, transforming to a $B2$ structure with $Pm\overline{3}m$ symmetry as seen in Figure 1-2b. $Ni_2MnGa$ exhibits a paramagnetic/ferromagnetic transition with a Curie temperature of around 373 K [32, 33].

At lower temperatures, $Ni_2MnGa$ undergoes a martensitic transformation which reduces the symmetry from cubic to tetragonal [34, 35, 36, 37, 38]. The new martensite unit cell has a body-centered tetragonal cell with $I4/mmm$ symmetry as shown in Figures 1-3. However, the martensite is usually described as a face-centered tetragonal cell related to the austenitic cubic $Fm\overline{3}m$ cell by a simple contraction along the $c$-axis forming a tetragonal structure. In this case $c/a < 1$ and this allows for the easy determination of the maximum strain:

---

[1] The Structurbericht notation is commonly used in this field.

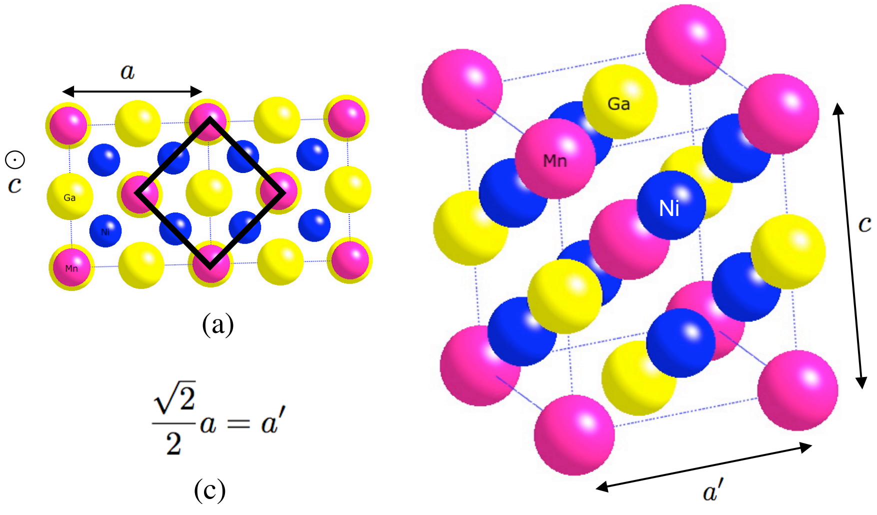

(a)

(c)

(b)

Figure 1-3: (a) Top view of original cubic unit cell showing its relation to the tetragonal cell of the martensite, outlined in black. (b) Tetragonal unit cell with $I4/mmm$ symmetry and $c/a' > 1$. (c) Relation between the $a$-axes in the two reference frames for the tetragonal cell.

$$\varepsilon_{max} = 1 - \frac{c}{a} \tag{1.1}$$

As the composition deviates from stoichiometry the martensite structure begins to change as well. Both tetragonal and orthorhombic structures have been found, with the majority of work focusing on Ni-rich compositions [39]. The martensitic transformation temperature as well as the c/a (and c/b for the orthorhombic phase) ratio has also been shown to be sensitive to composition. By changing the composition many alloys have been found that transform to martensite above room temperature and thus permit room-temperature actuation [26, 38, 40, 41].

## 1.4 Mechanism for Magnetic Field-Induced Strain

The macroscopic field-induced strain achievable in Ni–Mn–Ga alloys is the result of field-induced twin-boundary reorganization. In order for field-indeuced twin-boundary motion to occur the material must exhibit the following characteristics:

- *Mobile twin boundaries* — The stress required to move twin boundaries must be small, no greater than 1–2 MPa. If the twinning stress it too high, the applied magnetic field will unable to initiate twin-boundary motion.

- *Ferromagnetic martensite* — The transition from the paramagnetic to ferromagnetic state must precede the martensitic transition [42]. The material must also be in the martensitic state in the desired application environment.

- *Strong magnetocrystalline anisotropy* ($K_u$) — The orientation of the magnetic moment must be strongly linked to a particular crystallographic direction (the easy axis). $K_u$ is a measure of the energy required to rotate the magnetization to align with a field directed away from the easy axis.

These requirements can me summarized with the following mathematical relation:

$$K_u > M_s H > \sigma_{ex}\varepsilon_0 > \sigma_0\varepsilon_0 \tag{1.2}$$

where $K_u$ is the anistropy energy, $M_s H$ is a measure of magnetic energy input through the applied field ($M_s$ is the saturation magnetization and $H$ is the applied field), $\sigma_{ex}\varepsilon_0$ is a measure of the mechanical energy input through an applied external stress ($\sigma_{ex}$) and $\sigma_0\varepsilon_0$ is a measure of the energy necessary to move twin boundaries ($\sigma_0$ is the twinning stress and $\varepsilon_0$ is the twinning strain, see Figure 1-4).

Upon transformation to martensite, the preferred method of deformation in Ni–Mn–Ga alloys is through the formation and propagation of twins [27, 43, 44]. A schematic representation of a twin boundary is shown in Figure 1-5 for a tetragonal unit cell. The characteristic mirror symmetry at the twin boundary can be seen as well as the change in direction of the shorter $c$-axis and the longer $a$-axis. The different orientations of the martensitic unit cell are referred to as twin variants [45, 46].

Due to the large value for magnetocrystaline anisotropy, $K_u$, in Ni–Mn–Ga alloys, the magnetic moment aligns with the shorter $c$-axis in the absence of an applied magnetic field. Figure 1-5 shows the net magnetization vector $\mathbf{M}$ aligned with the $c$-axis and therefore changing directions across the twin boundary.

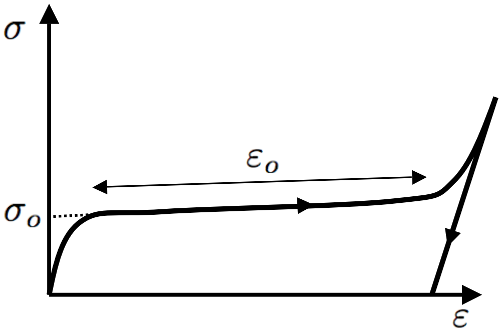

Figure 1-4: Schematic stress–strain diagram for Ni–Mn–Ga under a compressive stress. The flat portion of the curve corresponds to deformation through twin-boundary motion. $\sigma_0$ is the twinning stress and $\varepsilon_0$ is the twinning strain.

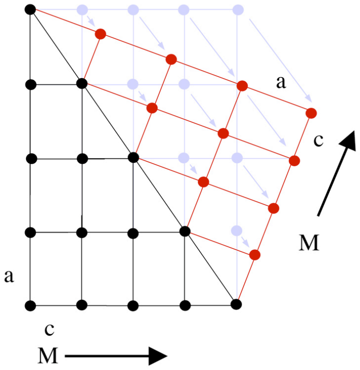

Figure 1-5: A two-dimensional schematic diagram of a twin boundary in a material with a tetragonal unit cell. The $a$- and $c$-axes in each variant are labeled, along with the direction of magnetization. The grey atoms represent the starting positions and the arrows indicate the necessary shear to produce the second variant.

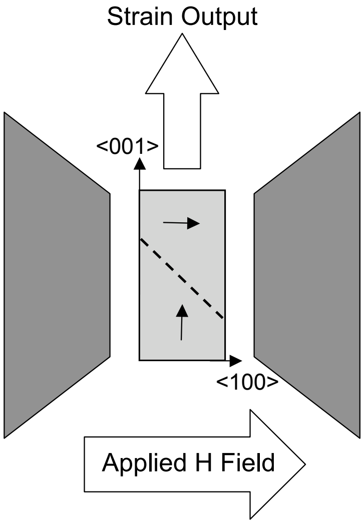

Figure 1-6: Schematic representation of an oriented single crystal containing two twin variants, the direction of applied magnetic field, and the direction of the resulting output strain. Dashed line indicates a single twin boundary with arrows indicating the direction of magnetization in each twin variant.

With a single crystal in a suitable orientation (as shown in Figure 1-6), an applied magnetic field will favor twin variants which have their magnetization vector aligned with the field. The system can lower its energy by growing favorable variants at the expense of unfavorable ones through the motion of partial dislocations [47]. The driving force for twin-boundary motion increases as the applied field increases until the anisotropy field, $H_a$ is reached. The anisotropy field, $H_a$, is the magnetic field necessary to saturate the material in the hard direction, i.e. away from the easy axis. At this point, the field is sufficiently large to overcome the anisotropy energy, thus rotating all the magnetization vectors into alignment with the applied field. Therefore, the magnitude of $K_u$ introduces an upper limit to the amount of magnetic driving force that can be introduced to the system.

The applied field produces a physical torque on the atoms of the unaligned variant equal to $\mathbf{M} \times \mathbf{H}$ [48]. This force produces a shear along the boundary that is capable of moving atoms from one equilibrium position to another, as shown in Figure 1-7. This motion of atoms advances the twin boundary one atomic plane. The motion of

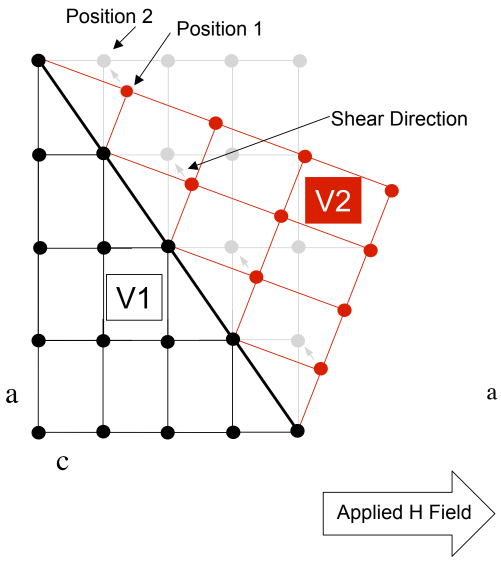

Figure 1-7: Mechanism for the advance of twin-boundary motion. Variant 1 (V1) has its magnetization aligned with the applied field while variant 2 (V2) does not. The applied field produces a torque which is resolved as a shear stress (shown with arrows) parallel to the twin boundary. This shear moves atoms in V2 from position 1 to position 2, thus increasing the size of V1, lowering the energy of the system, and advancing the twin boundary one step.

the twin boundary is able to reduce the Zeeman energy ($\mathbf{M} \cdot \mathbf{H}$) while avoiding an increase in magneto-crystalline anisotropy energy by keeping the magnetization along the easy *c*-axis.

## 1.5 Phonon Softening

There have been several studies of the martensitic transition focusing on the phonon-softening seen prior to the transformation of $Ni_2MnGa$ [2, 49, 50, 51, 52, 53]. Inelastic neutron scattering of the stoichiometric alloy compositions has revealed a phonon softening of the $[\xi, \xi, 0]$-TA2 branch as seen in Figure 1-8. This softening has been associated with a premartensitic transformation into a intermediate phase upon cooling. The reverse transformation has been observed to be directly into the austenite phase without an intermediate transition. The softening has been connected to the appearance of a periodic superstructure in the martensitic phases. The periodic struc-

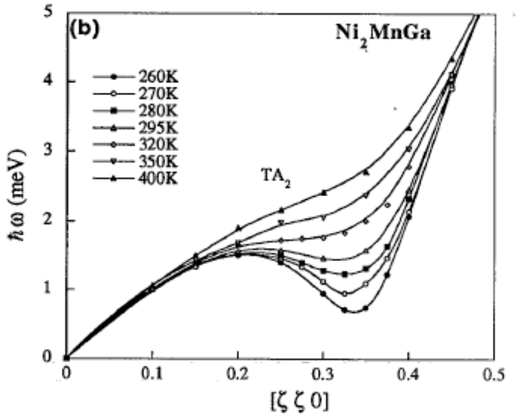

Figure 1-8: Inelastic neutron scattering from Ni$_2$MnGa of the $[\xi, \xi, 0]$-TA2 phonon branch as a function of temperature showing the softening as the martensitic transition is approached [2].

ture will be addressed in more detail in Section 2.3.1. More recently, Mañosa et al. have done similar experiments on off-stoichiometric compositions, revealing a larger degree of softening when the transition occurs in the ferromagnetic state as opposed to the paramagnetic state [54].

## 1.6 Review of Static, Dynamic and Pulsed-field Actuation Behavior

### 1.6.1 Static Actuation

Murray et al. studied the magnetic field-induced strain of Ni–Mn–Ga single crystals under various applied static uniaxial stresses [3, 28]. A plot of output strain versus applied magnetic field for various static loads is shown in Figure 1-9. For the smallest load, 0.34 MPa, the material displays the maximum strain expected from the tetragonal martensite structure, namely 6%, but does not return to the original state upon the removal of the magnetic field. In this case, the applied magnetic field is able to overcome the external mechanical stress, but the applied stress is not large enough to

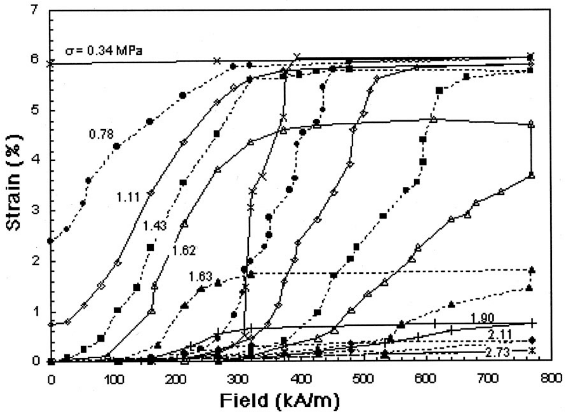

Figure 1-9: Magnetic field-induced strain versus applied field for different applied static uniaxial stresses. Each curve represents measured strain output under the indicated static stress (indicated in MPa), from Murray, et al. [3].

reset the sample back to the starting configuration. As the static load is increased, the amount of reset increases as well, with full reset achieved at about 1.43 MPa. As the load is increased beyond 1.43 MPa, the field-induced strain begins to decrease. In this case, the magnetic field cannot overcome the entire applied load and thus full extension is not possible. At loads of over 2 MPa, very little strain is observed because the magnetic energy input into the system cannot overcome the applied load.

It is important to note that increasing the applied field to a higher level will not produce any additional strain output at any compressive bias stress orthogonal to H. As discussed in section 1.4, the anisotropy energy, $K_u$ places an upper limit on the amount of magnetic energy that can be input to the system. Another important feature to note is the presence of a threshold field for magnetic actuation. No strain is observed until a critical magnetic field is reached. After the threshold field is achieved, the sample elongates to a value dictated by the magnetic-field strength and the applied external load.

### 1.6.2 Dynamic Actuation

The dynamic strain response of Ni–Mn–Ga FSMAs was characterized by Henry et al. [4, 55, 56, 57]. In these experiments, the static load was replaced by a spring to allow for AC actuation. Figure 1-10 shows several field-induced strain loops for various levels of average applied stress from the spring. For small external stresses, the output stress is also small because the sample does not reset completely, as was seen in the case of static loading. As the external stress increases up to about 1.5 MPa, the amount of reset also increases as well as the output strain. Higher values of the applied stress lead to blocking of twin-boundary motion and a decrease in the output strain.

As was seen previously with the case of static loading, the field-induced strain response displays threshold behavior. Until a critical field is reached, no strain is observed. Also, the maximum strain measured under AC loading is significantly smaller than that measured by Murray under static loading. It is believed the smaller dynamic output strain is a result of a reduction of active volume due to the constraints put on the ends of the sample by the testing fixture. If the strain calculation is adjusted to account for a smaller portion of the sample being active in the magnetic field, the resulting strain does increase, but not to the maximum of 6%. Henry also notes that the applied bias stress may prevent certain variants from elongating because the applied field cannot overcome the applied external stress [4], thus resulting in a lower output strain. Currently, Peterson et al. are attempting to increase the dynamic output strain and decrease the threshold field by the application of acoustic energy through the coupling of an FSMA crystal with a piezoelectric stack [58].

### 1.6.3 Pulsed-field Actuation

Marioni et al. have demonstrated pulsed-field actuation in Ni–Mn–Ga single crystals [59]. Using magnetic-field pulses of 620 $\mu$s duration and various peak strengths, the motion of individual twin boundaries was documented, as shown in Figure 1-11 [5]. It is clear from this work that the extension observed is due to movement of individual twin boundaries. The movement of the boundaries is consistent with the presence of discrete obstacles that impede the twin boundarie's motion. Twin boundaries appear to become pinned at defects which are stronger than the applied magnetic field pulse. When the pulse strength (driving force) is increased, some twins are able to

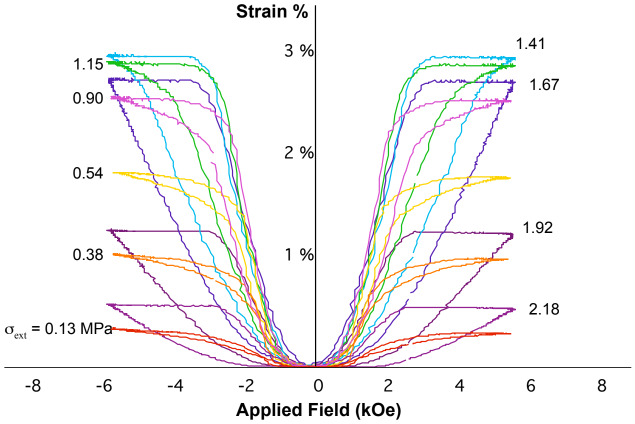

Figure 1-10: Dynamic field versus strain plots for 2 Hz magnetic-field actuation under different average bias stresses [4].

overcome the pinning obstacles and commence motion until a stronger pinning site is encountered. There appears to be a broad distribution of obstacle strengths as seen in Figure 1-11d, and a sharp peak near 0.56 $K_u$.

## 1.7 Modeling of Observed Behavoir

Phenomenological models have been constructed in order to describe the field-induced reorganization of twin variants [60, 61, 62]. These models include the Zeeman energy, magnetic anisotropy energy, an internal restorative elastic energy, and an external applied stress. Using a simple system consisting of two variants, the magnetic-field induced strain can be written as a function of the volume fraction of of each twin variant, $f_i$:

$$\varepsilon(H) = \varepsilon_\circ \delta f = \frac{2K_u h(1 - h/2) - \sigma\varepsilon_\circ}{C_{\text{eff}}\varepsilon_\circ} \tag{1.3}$$

where $\varepsilon_\circ$ is the transformation strain, $\delta f$ is $f_1 - 1/2$, $h$ is the reduced field defined as:

$$h = \frac{M_s H}{2K_u} \tag{1.4}$$

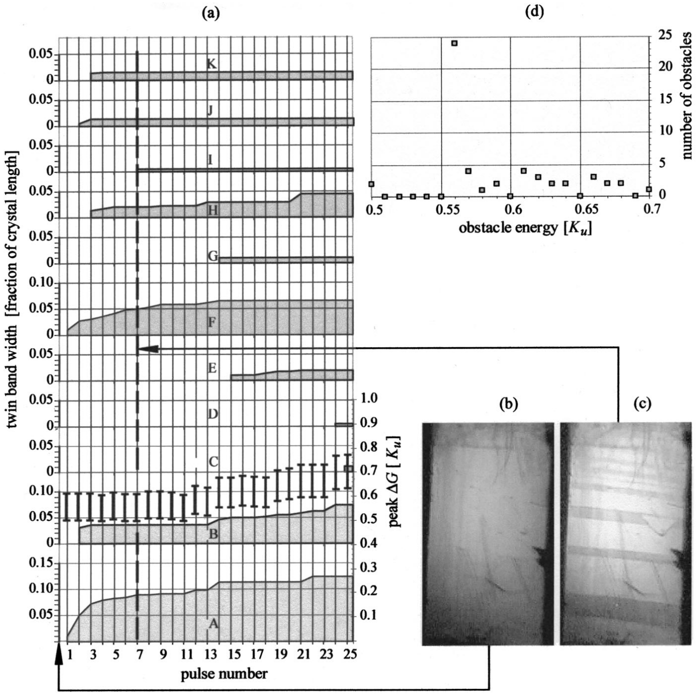

Figure 1-11: (a) Evolution of twin band thickness for a series of individual magnetic-field pulses applied without resetting the crystal. Vertical lines indicate pules height and are referenced to the right scale. The initial and intermediate twin structure is shown in (b) and (c). The distribution of defect strengths is shown in (d). From Marioni et al. [5].

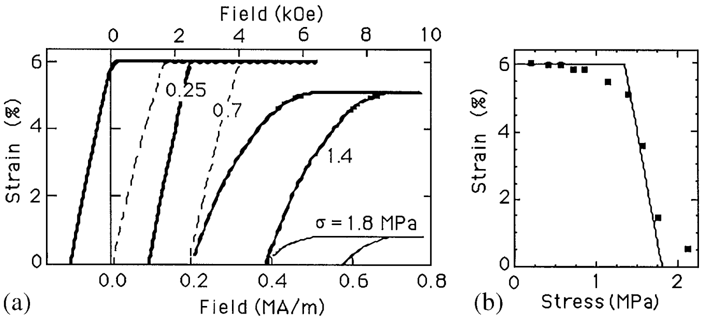

Figure 1-12: (a) Calculated strain versus applied field curves from Equation 1.3 and (b) calculated output strain versus applied external stress (solid line) overlaid with experimental data (points), from Murray et al. [3].

and $C_{\text{eff}}$ is the effective modulus of the twinned material taking into account areas that are not active [60, 63].

Plots of the calculated strain versus applied field are shown in Figure 1-12a and can be compared to the experimental results depicted in Figure 1-9 [3]. At first the applied load is not sufficient to reset the sample. As the applied stress is increased, the sample begins to reset and further increases in stress results in a decrease in the calculated output strain due to blocking by the external stresses. Figure 1-12b compares the measured maximum output strain with those calculated with the model under different applied external stress, showing good agreement. One shortcoming of this thermodynamic model is the absence of the threshold behavior observed in the experiments. The threshold behavior in Figure 1-12a was described by subtracting or adding an arbitrary field to $H$ on increasing and decreasing field cycles. It should be noted that these thermodynamic models describe an equilibrium variant distribution that may not be achieved for kinetic reasons in the presence of defects.

Micromagnetic models describing twin-boundary motion have been developed by Paul which address many facets of magnetic shape-memory effect that are not amenable to macroscopic, thermodynamic phenomenology [64, 65]. The initial work described the interaction of the twin boundary and magnetic domain wall, finding that under an applied magnetic field the domain wall moves ahead of the twin boundary. Paul's work also deals with the interaction of the twin boundary with a dislocation-like defect. Defects tend to hinder the motion of twin boundaries and defects of sufficient strength are capable of pinning the twin boundary. More recent work has been focused on the microscopic understanding of the thermal activation of twin-boundary motion [66].

## 1.8 Goals and Scope of Thesis

The objective of the present study is to perform a more fundamental investigation of the structure of Ni–Mn–Ga alloys to compliment the extensive engineering/actuation properties research that has been performed previously. Through a better understanding of the crystallography and microstructure of these alloys, an important outcome will be the impact this work could have on the practical performance of Ni–Mn–Ga FSMAs. The specific goals and areas of investigation are to:

- Systematically explore the structure-composition relationship over a range of Ni–Mn–Ga alloys using x-ray diffraction. Determine the composition ranges of stability for the different martensitic structures with particular focus on the range of compositions used in single-crystal actuation experiments.

- Characterize the martensitic transformation behavior of the tetragonal and orthorhombic phases using magnetic measurements and x-ray diffraction. Develop a model to explain the differences observed.

- Evaluate the state of chemical order of several different alloy compositions through the use of powder neutron diffraction. Evaluate the site occupancies to determine the state of order in the off-stoichiometric alloys.

- Examine the microstructure of several Ni–Mn–Ga alloys of different compositions to better understand the crystal structure, types of twinning, and types of defects present. Relate the observed microstructural features to the field-induced strain behavior of the specific alloy compositions.

## 1.9 Overview of Thesis Document

There has been a great deal of research that has focused on the attaining the maximum field-induced strain in ferromagnetic shape-memory alloys under both static and dynamic conditions. This information is extremely useful when attempting to design devices that involve Ni–Mn–Ga for specific applications. It is also necessary to understand the structure of Ni–Mn–Ga alloys as well as how the structure changes with composition because the evidence indicates that the actuation of these alloys depends on the martensite structure.

As mentioned previously, some work has been done on a variety of compositions, mostly nickel-rich. However, there has been limited study of the composition range which has shown the most promise for field-induced actuation. Chapter 2 details a systematic exploration of the structure–composition relationship over a range that spans different crystal structures and also different observed actuation behavior. Mapping of the room-temperature martensitic phase fields is essential in trying to select alloy compositions for specific applications. For example, if a larger strain and low stress is required, alloys exhibiting the orthorhombic martensite phase would be suitable. In contrast, if a larger stress and lower strain is needed, tetragonal martensite would be a better choice. Also a phase diagram of the different martensitic structures will provide essential data for crystal production by delineating composition ranges where each phase is present. This will provide specific limits on acceptable composition inhomogeneities to ensure crystals contain only a single martensitic phase.

The martensitic transformation temperature is also connected to the alloy composition in the Ni–Mn–Ga system. By characterizing the transition behavior of the alloy compositions studied by x-ray diffraction, the potential operating environments of specific alloys can be identified. Chapter 3 details the experiments performed in order to characterize the martensitic transformation. Low-field susceptibility measurements provide a simple way to measure the transformation temperatures due to the change in symmetry in going from austenite to martensite. It is clear from the evidence presented here that the transition temperature is not as much connected to the alloy composition but rather the nature of the transition is linked to the underlying martensitic phase present. It is typical to identify a single transformation temperature for a particular alloy composition, either the start, finish or an average of the two. If the transition behavior of the martensitic phases is different, then more detailed information of the transformation is required when assessing the suitability of particular alloys compositions for specific application environments.

The crystal structure–composition relationship is only one facet of the impact that structure has on Ni–Mn–Ga alloys. The chemical order is also affected as the composition changes, especially as one moves further from the stoichiometric $Ni_2MnGa$ composition. Previous published work in this area, presented in Chapter 4, has dealt mainly with the austenite phase and with the stoichiometric composition. There has been little study of the martensite phase and also compositions containing greater or less than 50 atomic percent Ni.

Since many of the compositions which show magnetic-field induced strain are far from stoichiometery, the role of the state of chemical order may play an important role in the material performance. A small degree of chemical disorder may introduce defects of a structural or magnetic nature that impact the motion of twin boundaries, and in turn, affect the output strain obtained. The degree of order can impact the twinning behavior by affecting the resistance to slip. Because slip creates high-energy antiphase boundaries in an ordered material, deformation by slip would be more difficult in more highly ordered crystals, thus promoting deformation by twinning. Chapter 4 details simulations of x-ray and neutron diffraction and the role ordering plays. Also, results of neutron diffraction experiments on several different alloy compositions are presented and interpreted. It is unclear at this point what role chemical order plays in the performance of Ni–Mn–Ga alloys, but more information will help in understanding why certain alloy compositions show field-induced strain while others do not.

Finally, there has been limited work on understanding the microstructure of Ni–Mn–Ga alloys. Many of the studies that employed transmission electron microscopy have only reported electron diffraction results as they help identify the crystal structure. Little is known about the types of twinned structures that are present in these alloys and what types of defects exist. It is clear from the work of Marioni, cited earlier, that twin-boundary motion is a stochastic process (analogous to magnetic-domain wall motion). The motion of twin boundaries is essentially limited by the strength and distribution of dects. The interaction between moving twin boundaries and defects, such as inclusions or precipitates, will influence the ability to obtain the maximum output strain. Direct observation of different pinning sites will complement the work done by Marioni (Section 1.6.3) and help explain why some crystals show relatively easy twin-boundary motion under an applied magnetic field and others fail to show any field-induced strain. Transmission electron microscopy is the ideal tool for characterizing microstructural features, providing both detailed images and crystallographic information.

Chapter 5 presents results related to the microstructure of Ni–Mn–Ga alloys observed through transmission electron microscopy. Twinning on several different length scales is documented along with the discovery of several different kinds of second-phase particles arising from impurities such as S, Ti and Ta. These inclusions and precipitates will certainly impact the strain output observed from these crystals by impeding twin-boundary motion and approximations of the relative strength of these defects is presented.

# Chapter 2

# Crystal Structure Analysis

## 2.1 Experimental Details

The Ni–Mn–Ga crystals used in this study were grown by the Bridgman technique at the Ames Laboratory [67]. High-purity nickel, manganese and gallium were arc melted into buttons and then drop cast into a chilled copper mould. In some crystals, manganese was further purified to remove excess sulfur. The as-cast ingots were placed in an alumina crucible and heated to 1350° for one hour and allowed to homogenize. The crucible was then withdrawn from the hot zone at a rate of 5.0 mm/h. In order to minimize evaporation of manganese during crystal growth, the furnace was back-filled to a positive pressure of $6.8 \times 10^5$ Pa with purified argon gas after the chamber had been outgassed at 1350°C under vacuum.

A piece was cut along the entire length from each crystal received at MIT and then heat-treated for 24 hours at 900$^o$C under a purified argon atmosphere. This is the typical heat treatment used in the preparation of single-cystal specimens used for actuation experiments. The composition of each piece was then determined using wavelength-dispersive x-ray spectroscopy on a JEOL JXA-733 Electron Probe Microanalyzer. The measurement was made along the length of the crystal at approximately 1 mm intervals.

Individual samples of approximately uniform size were cut from each piece and crushed into powders. In order to relieve the stress imparted by mechanical grinding, the powders were then annealed for 3 hours at temperatures from 500–700°C. The lowest temperature was selected in order to minimize the possibility of any changes in composition. Compositions of the powders were measured again after annealing using WDS as well as energy-dispersive spectroscopy on a Leo352 and found to differ by less than 0.5-1%.

Crystal structure analysis of the powders was carried out using a Rigaku rotating-anode x-ray diffractometer with copper target operated at 60 kV, with a current of 300 mA and a monochrometer isolating Cu-K$\alpha$ radiation. Background and peak locations were determined using the Jade software. Martensite transformation and Curie temperatures were determined by measuring low-field magnetization as a function of temperature and will be discussed further in Chapter 3.

## 2.2 Compositions Analyzed

A representative plot of the composition measured in the longitudinal direction along the crystal boule is shown in Figure 2-1. A moderate concentration gradient can be observed along the entire length of the crystal. This is in contrast to the relative uniformity of the composition in the transverse direction as seen in Figure 2-2. This variation in composition along the length of the crystal enabled the preparation of many samples of different compositions for structure determination.

Pieces cut from the single crystal boule were heat treated in a manner similar to that used to prepare oriented single-crystals for actuation experiments. The composition of one of these pieces was measured before and after heat treatment and the results are displayed in Figure 2-3. The composition can be seen to vary slightly before and after heat treatment. This could be the result of a small degree of oxidation during the annealing. Because of the possibility of a slight composition change after heat treatments, the composition of each sample was verified after any significant heating. This was especially important in the case of the crushed powder which required a short anneal to relieve the stresses induced by power preparation.

A representative plot of the composition of actual powder diffraction specimens

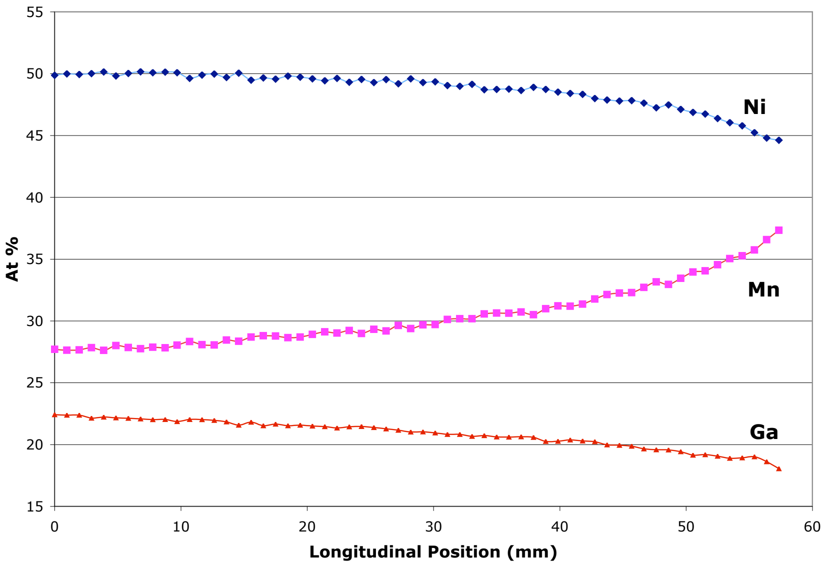

Figure 2-1: Composition measured longitudinally of one Ni–Mn–Ga single crystal boule (TL-3).

is shown in Figure 2-4. Pieces cut from the single crystal were cut small enough (2-3 mm) in order to achieve a sample of uniform composition. The composition profile is similar to that measured on the single crystal (Figure 2-1).

## 2.3 Powder Diffraction

Crushed powder had a large amount of stress built up due to the force used to prepare them from single crystals. The real structure can only be revealed after a short heat treatment to relieve stress. In order to minimize any composition changes, the lowest temperature and shortest time for the stress-relief anneal was chosen. Figure 2-5 shows a representative x-ray pattern from sample before and after heat treatment. Several broad peaks in the as-crushed pattern are characteristic of material containing significant residual stresses. After treatment, many more, sharper peaks can be seen.

Two representative patterns of the tetragonal and orthorhombic martensite are shown in Figure 2-6. The indexing scheme used throughout is referenced to the parent cubic phase which is the common convention when reporting results for these

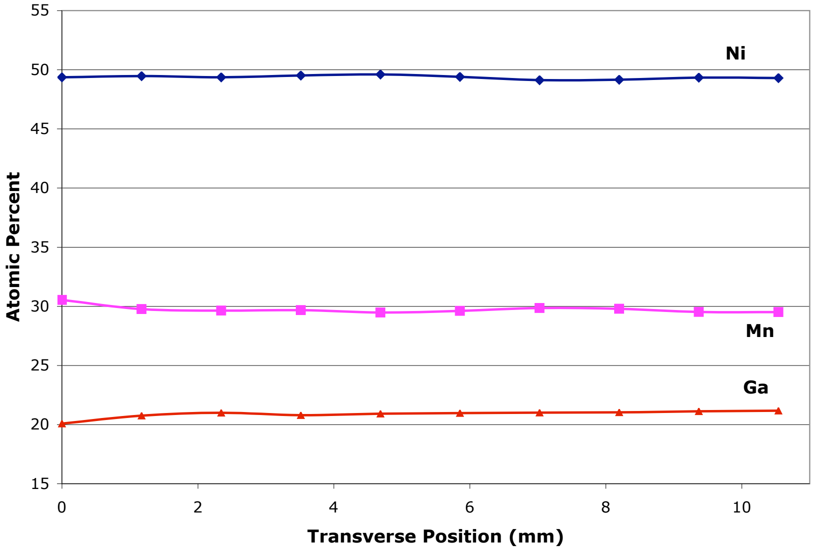

Figure 2-2: Composition measured in the transverse direction of one Ni–Mn–Ga single crystal boule (TL-3).

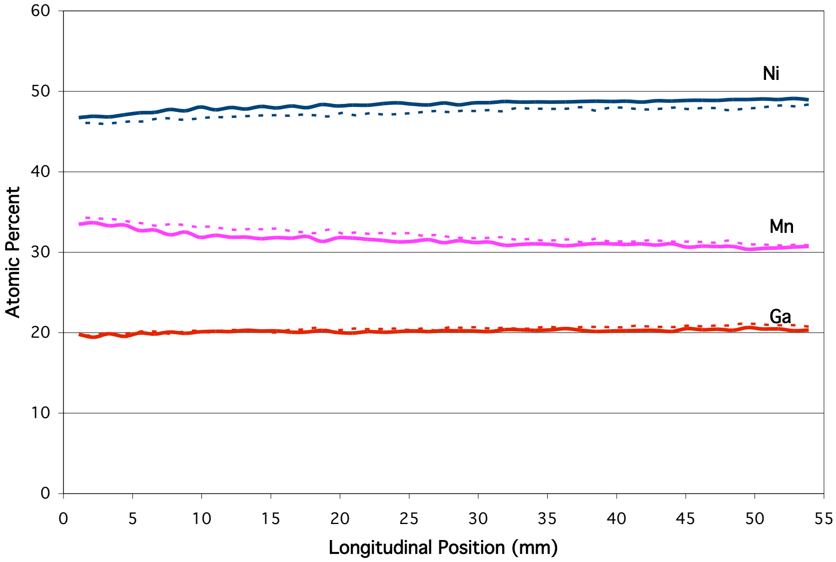

Figure 2-3: Longitudinal composition of one Ni–Mn–Ga single crystal boule (TL-5) before (solid) and after (dashed) heat treatment at 900°C.

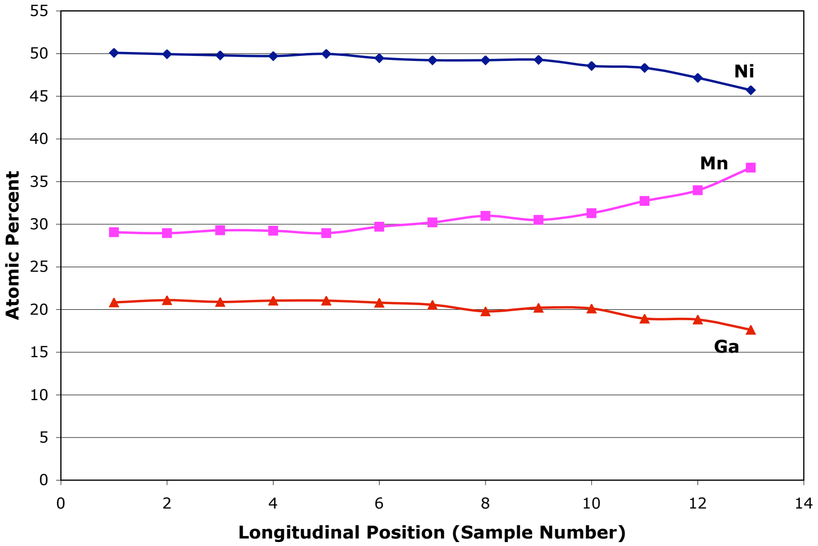

Figure 2-4: Composition of powder x-ray samples take from crystal TL-3 used in the structure determination.

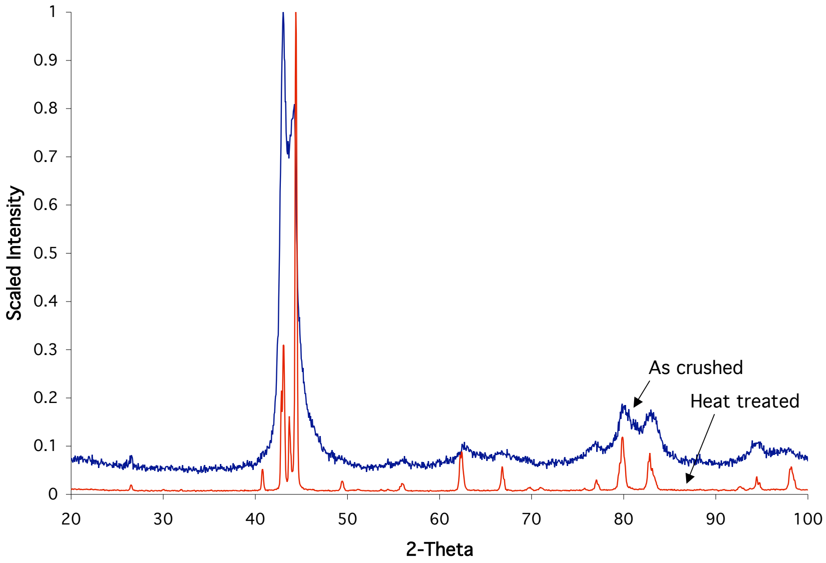

Figure 2-5: Measured x-ray patterns from as-crushed and heat treated powder showing stress relief.

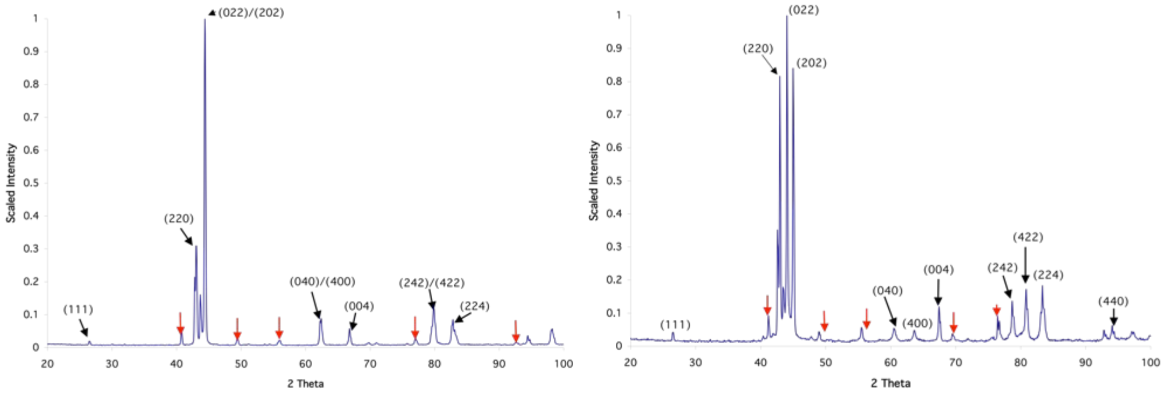

(a) (b)

Figure 2-6: Representative patterns of the (a) tetragonal and (b) orthorhombic martenisitic structures. Peaks indexed with respect to parent austenite unit cell. Red arrows indicate extra peaks which arise due to the superstructue.

alloys. The additional peak splitting due to the unique *b*-axis is indicative of the orthorhombic phase. The additional peaks in each pattern which are not indexed result from the presence of a long-period superstructure, referred to as 5M or 10M for the tetragonal phase and 7M or 14M for the orthorhombic (see Section 2.3.1). This more complex structure actually has a unit cell which is quite large, but it is common to use the simpler tetragonal and orthorhombic unit cells. This facilitates a better understanding of the structural aspects of the field-induced strain behavior. Evidence of the superstructure can also be seen using electron diffraction, as shown in Figure 2-7, and will be discussed in Chapter 5.

### 2.3.1 Superstructures ("Modulated" Structures)

There have been two approaches to describe the long-range periodic structures that are found in certain compositions of Ni–Mn–Ga alloys. Martynov et al. [35] attempts to describe the structure as a modulation of atomic positions while Pons et al. [8] view the structure as a periodic stacking of close-packed planes.

It is important to note that the term "modulation" is incorrectly applied in this case. In a true crystallographic description, the periodic structure observed in Ni–

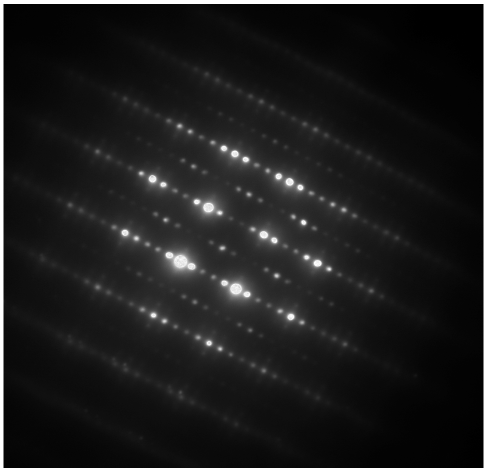

Figure 2-7: Representative electron diffraction patternshowing five-layered structure (100 zone axis). The four extra satellite peaks between fundamental spots are characteristic of the periodic structure.

Mn–Ga is referred to as a superstructure because it is connected to the periodicity of the lattice. The superstructure is a larger lattice that can be specified as a linear combination of the translations of the parent structure [68]. The term "modulated structure" typically refers to a variation (atomic positions or composition) that is incommensurate with the lattice. However, in the literature describing the structure of Ni–Mn–Ga alloys the term "modulated" is used as opposed to the correct description of the structure as a superstructure.

The Martynov —"modulated"— description of the structure starts with the tetragonal distortion of the original parent phase into martensite. However, in order to describe extra diffraction peaks observed in experiments, a periodic shuffling is included along the $(110)[1\bar{1}0]_A$ system, with a period of 5 lattice planes of $(110)_A$ type.[1] However, the unit cell of the martensite is redefined to that of a body-centered tetragonal structure with new axes along $[1\bar{1}0]_A$, $[001]_A$ and $[110]_A$. The displacement of each atomic plane (j) along the new $a$-axis ($[1\bar{1}0]_A$) is given by a function $\Delta_j$ which contains three terms and is shown in Equation 2.1.

$$\Delta_j = A\sin\left(\frac{2\pi j}{L}\right) + B\sin\left(\frac{4\pi j}{L}\right) + C\sin\left(\frac{6\pi j}{L}\right) \tag{2.1}$$

---

[1] The subscript "A" indicates indices referenced to the parent austenite unit cell.

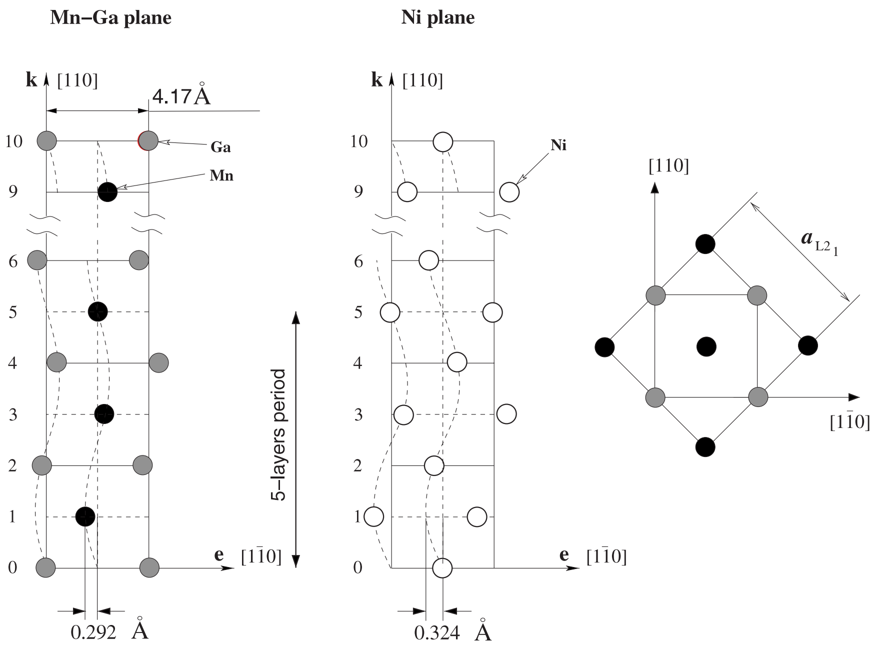

Figure 2-8: Projection of the 5-layer modulated structure, from Zayak et al. [6].

L defines the modulation period and the coefficients A, B, and C are adjusted in order to match the position and intensities of the extra reflections found. A projection of the atom positions in the modulated structure is shown in Figure 2-8. It can be seen that the period of the modulation is 5 atomic layers, and after one period the atomic positions correspond to the expected positions in the non-modulated tetragonal structure. A similar picture can be obtained for the of the seven-layer 7M structure.

The same type of structure has also been described as a packing of close-packed planes, similar to the approach used to describe long-period martensites in Ni–Al alloys [69, 70, 71]. The structure is constructed by stacking planes derived from the $\{110\}_A$ with the sequences $(5\bar{2})$ and $(3\bar{2})$. This notation describes the structure as 5 planes stacked with offsets in one direction, 2 in the opposite direction, which is given the designation 14M, while the other is denoted as 5M. This stacking sequence can be easily identified in simulated high resolution electron micrographs as shown in Figure 2-9. Pons has also identified another martensite stacking sequence, namely

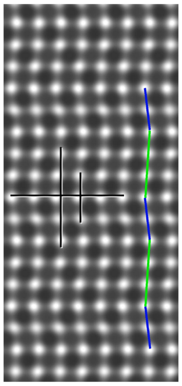

Figure 2-9: Simulated image of the 5-layer stacking sequence, $(3\bar{2})$, from Pons et al. [7]

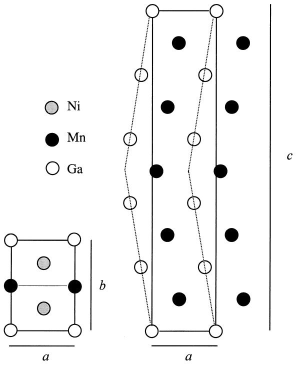

Figure 2-10: Schematic representation of the unit cell in 10-layer martensite, $(5\bar{5})$ stacking sequence, from Pons et al. [8].

the $(5\bar{5})$ for ten-layered martensite (Figure 2-10).

Each model of the martensitic superstructure can be used to explain the extra satellite peaks observed in both x-ray and electron diffraction. However, each approach is slightly different and yields distinct atomic positions as seen in Figure 2-11. In this figure, the atomic positions are plotted using both approaches to explain the periodic structure. Both models predict similar atomic positions, but they do not overlap exactly. Until recently, both models were accepted and used in studying these alloys. Combining image simulation with high resolution electron microscopy, Pons has determined that for the case of the seven-layered martensite, the stacking model matches the true structure, while the modulation approach does not. In the case of

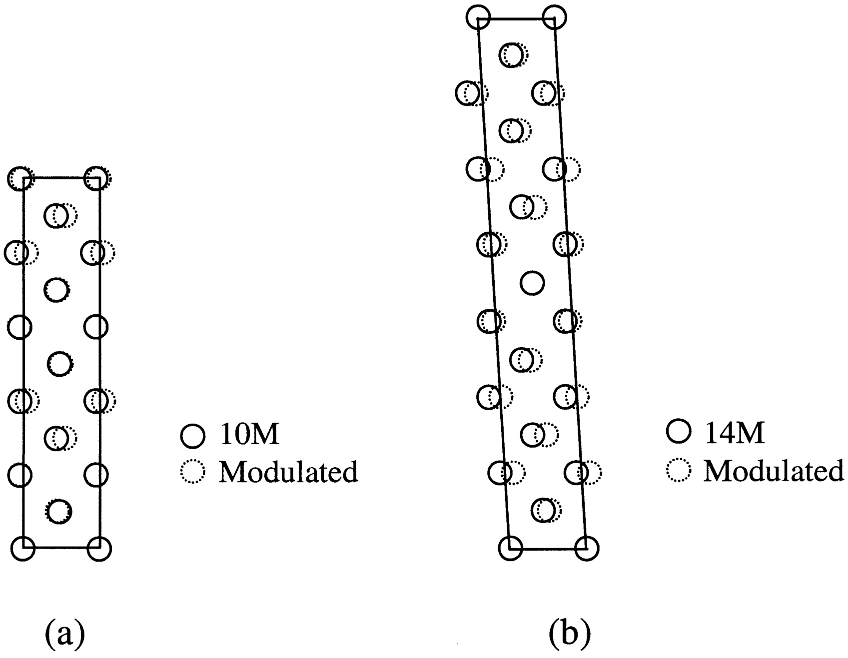

Figure 2-11: Comparison of the two approaches to the periodic martensitic structure of Ni–Mn–Ga, (a) five-layered and (b) seven-layered, from Pons et al. [8].

the five-layer structure, the imaging and simulation are unable to discern between the two models.

### 2.3.2 Compilation of X-ray Measurements

Of the four large crystals studied, two displayed both the tetragonal and orthorhombic structures as the composition changes along the length, TL2 and TL3, shown in Figures 2-12 and 2-13. As can be seen from the series of diffraction patterns, one end of the crystal displays the tetragonal structure while the other end shows the orthorhombic phase. Both crystals contain areas that consist both phases, however it is difficult to determine the relative amounts of each phase present in these samples.

On the other hand, the two other crystals examined, TL5 and TL8, both exhibit a uniform structure along the entire crystal boule. Figure 2-14 shows the structure of TL5 as orthorhombic while Figure 2-15 clearly reveals the tetragonal structure along

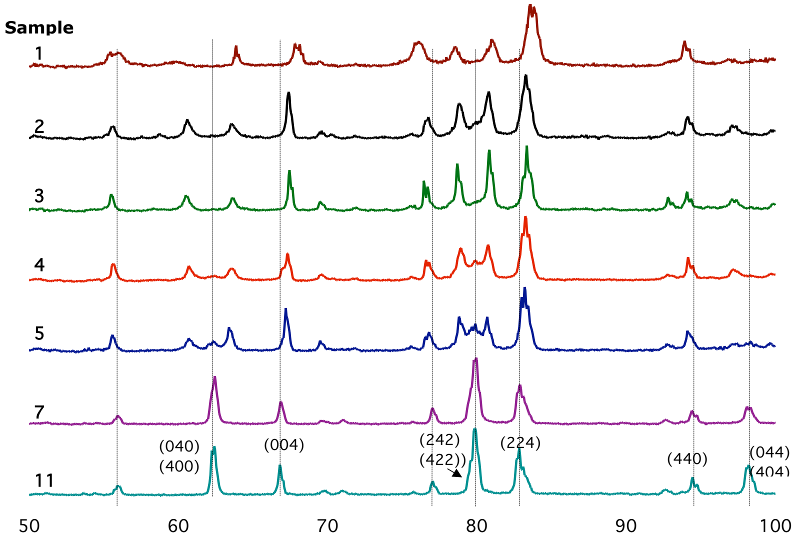

Figure 2-12: Power x-ray diffraction patterns taken along the length of TL-2 showing the transition from tetragonal (5M) to orthorhombic (14M). Two mixed phase samples can also be seen containing both of these structures. (Note: Intensities have been scaled and the baseline is offset for each composition.)

the length. The composition of these two boules are more uniform as compared to TL2 and 3 owing to improvements in the crystal growth technique [72]. This resulted in large crystals which were homogenous in composition. A summary of data from all the compositions studied is displayed in Table 2.1.

Lattice constants for each sample, calculated with the Cohen [73] analytical method, confirm that the $c/a$ ratio for the tetragonal samples is approximately 0.94. This matches the observed limit of 6% for the maximum magnetic field-induced strain. For the orthorhombic samples, the $c/b$ ratio ($b$ being the longest unit cell axis as per crystallographic convention) was about 0.90 for all the samples.This allows for a maximum strain of about 10% which corresponds to values reported in the literature [74].

The values calculated for $c/a$ and $c/b$ are plotted versus electrons per atom ($e/a$) in Figure 2-16. These values were calculated using the following values for number of electrons per atom: 10 for Ni, 7 for Mn, and 3 for Ga. $e/a$ is often used as a single parameter in the characterization of Ni–Mn–Ga alloys. For example, a linear relationship between martensitic transformation temperature and $e/a$ has been demonstrated

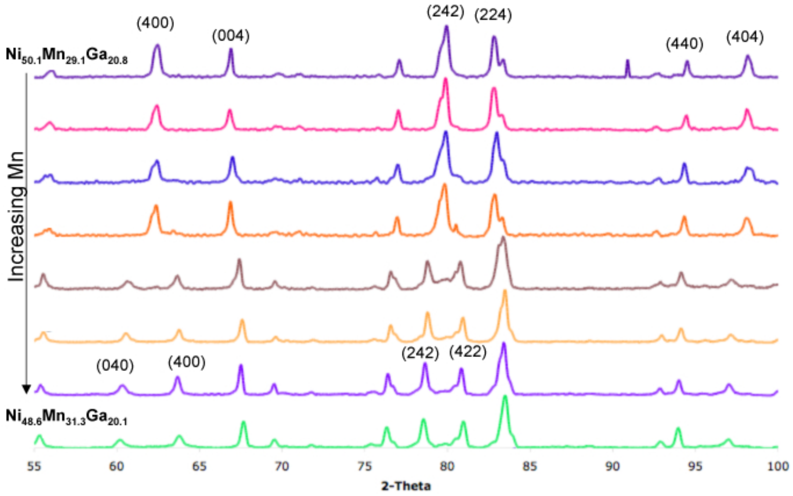

Figure 2-13: Power x-ray diffraction patterns taken along the length of TL-3 showing the transition from tetragonal (5M) to orthorhombic (14M). A mixed phase sample can also be seen containing both of these structures. (Note: Intensities have been scaled and the baseline is offset for each composition.)

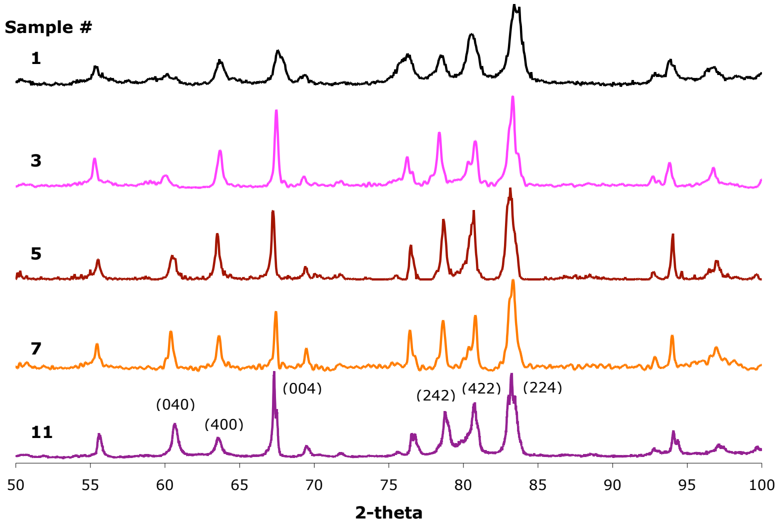

Figure 2-14: Power x-ray diffraction patterns taken along the length of TL-5 which is orthorhombic (14M) along the entire length. (Note: Intensities have been scaled and the baseline is offset for each composition.)

Table 2.1: Compositions of powders after stress-relief treatment (in atomic percent), transformation temperatures ($^o$C), room temperature structures, and relevant lattice constants (Å) for all samples. 5M indicates tetragonal, 14M is orthorhombic, and Mixed indicates both phases were present. A typical austenite lattice parameter is 5.8472 Å.

| Sample | Ni | Mn | Ga | $T_m^s$ | Structure | a | b | c | c/a | c/b |
|---|---|---|---|---|---|---|---|---|---|---|
| TL2-1 | 48 | 31.9 | 20.1 | 50 | 14M | 5.8158 | 6.1530 | 5.5203 | 0.95 | 0.90 |
| TL2-2 | 49.1 | 30.5 | 20.3 | 46 | 14M | 5.8432 | 6.0968 | 5.5559 | 0.95 | 0.91 |
| TL2-3 | 49.3 | 30.3 | 20.4 | 38 | 14M | 5.8384 | 6.1068 | 5.5502 | 0.95 | 0.91 |
| TL2-4 | 49.2 | 30.1 | 20.7 | 37 | Mixed | 5.8470 | 6.0875 | 5.5627 | 0.95 | 0.91 |
| TL2-5 | 49.6 | 29.9 | 20.5 | 36 | Mixed | 5.8551 | 6.0860 | 5.5668 | 0.95 | 0.91 |
| TL2-6 | 49.5 | 29.5 | 21 | 35 | 5M | 5.9832 | - | 5.6295 | 0.94 | - |
| TL2-7 | 50.1 | 28.9 | 21.1 | 34 | 5M | 5.9425 | - | 5.5997 | 0.94 | - |
| TL2-8 | 50.1 | 28.6 | 21.3 | 34 | 5M | 5.9400 | - | 5.6075 | 0.94 | - |
| TL2-9 | 50 | 28.3 | 21.7 | 33 | 5M | 5.9413 | - | 5.6133 | 0.94 | - |
| TL2-11 | 50 | 28.9 | 21.1 | 34 | 5M | 5.9419 | - | 5.6034 | 0.94 | - |
| TL3-1 | 50.1 | 29.1 | 20.8 | 32 | 5M | 5.9353 | - | 5.5977 | 0.94 | - |
| TL3-2 | 49.9 | 29 | 21.1 | 32 | 5M | 5.9403 | - | 5.6001 | 0.94 | - |
| TL3-3 | 49.8 | 29.3 | 20.9 | 36 | 5M | 5.9462 | - | 5.5869 | 0.94 | - |
| TL3-4 | 49.7 | 29.2 | 21.1 | 39 | 5M | 5.9453 | - | 5.5973 | 0.94 | - |
| TL3-5 | 50 | 29 | 21.0 | 44 | 5M | 5.9443 | - | 5.599 | 0.94 | - |
| TL3-6 | 49.5 | 29.7 | 20.8 | 49 | Mixed-5M | 5.9472 | - | 5.5701 | 0.94 | - |
| TL3-6 | 49.5 | 29.7 | 20.8 | 49 | Mixed-14M | 5.8404 | 6.0794 | 5.5658 | 0.95 | 0.92 |
| TL3-7 | 49.2 | 30.2 | 20.6 |  | 14M | 5.8393 | 6.0920 | 5.5501 | 0.95 | 0.91 |
| TL3-8 | 49.2 | 31 | 19.8 |  | 14M | 5.8260 | 6.1020 | 5.5384 | 0.95 | 0.91 |
| TL3-9 | 49.3 | 30.5 | 20.2 |  | 14M | 5.8333 | 6.1201 | 5.5433 | 0.95 | 0.91 |
| TL3-10 | 48.6 | 31.3 | 20.1 |  | 14M | 5.8230 | 6.1236 | 5.5337 | 0.95 | 0.90 |
| TL3-11 | 48.3 | 32.7 | 19 |  | 14M | 5.8124 | 6.1435 | 5.4908 | 0.94 | 0.89 |
| TL3-12 | 47.2 | 34 | 18.8 |  | 14M | 5.8274 | 6.2120 | 5.4934 | 0.94 | 0.88 |
| TL3-13 | 45.7 | 36.6 | 17.7 |  | 14M | 5.8472 | 6.2125 | 5.4828 | 0.94 | 0.88 |
| TL5-1 | 47.3 | 33.1 | 18.6 | 50 | 14M | 5.8466 | 6.1432 | 5.5391 | 0.95 | 0.90 |
| TL5-3 | 48.2 | 31.7 | 20.1 | 45 | 14M | 5.8333 | 6.1466 | 5.5478 | 0.95 | 0.90 |
| TL5-5 | 48.9 | 30.5 | 20.6 | 42 | 14M | 5.8507 | 6.1035 | 5.5651 | 0.95 | 0.91 |
| TL5-7 | 48.7 | 21.1 | 20.2 | 40 | 14M | 5.8375 | 6.1153 | 5.5498 | 0.95 | 0.91 |
| TL5-9 | 49 | 30.3 | 20.8 | 40 | 14M |  |  |  |  |  |
| TL5-11 | 49 | 30.6 | 20.4 | 37 | 14M | 5.8450 | 6.0951 | 5.5602 | 0.95 | 0.91 |
| TL8-1 | 50.5 | 27.9 | 21.6 | 30 | 5M | 5.9414 | - | 5.6184 | 0.95 | - |
| TL8-5 | 50.3 | 28.2 | 21.5 | 29 | 5M | 5.9315 | - | 5.6057 | 0.95 | - |
| TL8-7 | 50.1 | 28.4 | 21.5 | 32 | 5M | 5.9294 | - | 5.5862 | 0.94 | - |
| TL8-9 | 50.1 | 28.8 | 21.1 |  | 5M | 5.9435 | - | 5.6094 | 0.94 | - |
| TL8-11 | 50.4 | 28.1 | 21.5 | 28 | 5M | 5.9325 | - | 5.6055 | 0.94 | - |

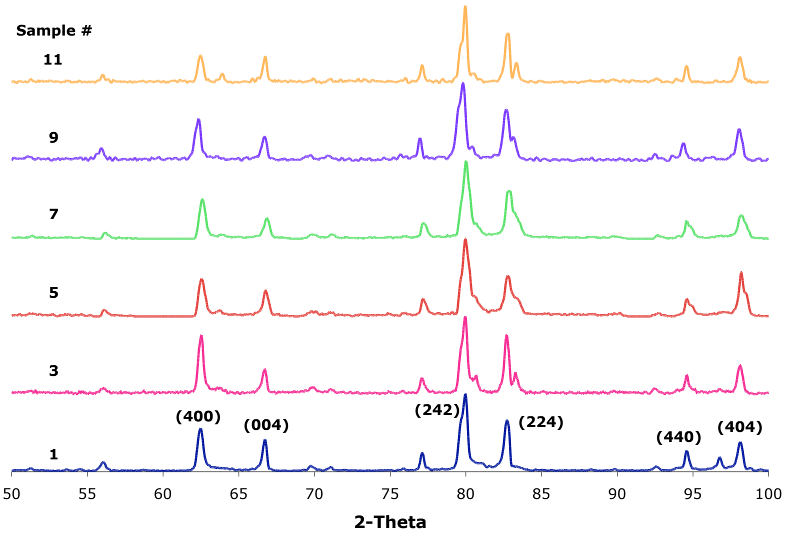

Figure 2-15: Power x-ray diffraction patterns taken along the length of TL-8 which is tetragonal (5M) along the entire length. (Note: Intensities have been scaled and the baseline is offset for each composition.)

[10]. However, as can been seen in Figure 2-16, this parameter is not adequate to predict the martensite crystal structure as compositions with similar $e/a$ values may display different structures. The one success of this type of analysis, by Chernenko [9], can be seen in values of $e/a > 7.7$ which clearly show the non-modulated structure and a $c/a$ ratio greater than 1.

A more useful way to graphically display structural and composition information is shown in Figure 2-17, which is a type of phase diagram in the vicinity of room-temperature. By plotting the data in this manner, it can be seen that the alloys exhibiting the 5M tetragonal structure and those with the 14M orthorhombic are distributed in two distinct regions of the composition space. All but one of the mixed phase compositions falls between these two areas. The tetragonal structure is seen in compositions close the 50-nickel line (shown as dashed), while samples with the 14M structure lie to the right of the 50 atomic percent nickel line, indicating they are nickel-poor compositions. Others have shown [8, 75] that the non-modulated structure is found in nickel-rich compositions, although no similar alloys were studied in this work.

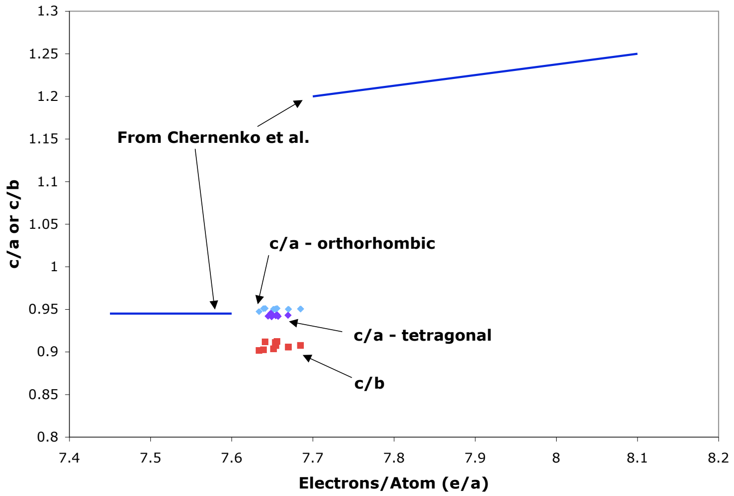

Figure 2-16: $c/a$ and $c/b$ versus electrons per atom $(e/a)$ for the alloys studied. Solid lines taken from Chernenko et al. [9]. The $c/a$ values greater than one are for the non-modulated structure.

Transition temperatures are shown by the solid lines, and represent a large amount of data taken from the literature and analyzed by Jin et al. [10]. The compositions represented on this plot fall in a region with transformation temperatures at or above room temperature, which is consistent with the measurements performed. However, the transition behavior of the two types of martensite structures display a unique character and will be discussed further in Chapter 3.

Materials falling within the tetragonal zone have been shown to be active in a magnetic field and be capable of yielding up to 6% field-induced strain. These compositions appear to be the easiest to actuate, while the crystals presented here from the orthorhombic region have not shown any field-induced strain. Others [74] have documented up to 10% field-induced strain in some 14M compositions, however the majority of documented studies on actuation behavior focus on the tetragonal martensite. The difficulty in actuating these particular 14M crystals may be related to specific microstructural features, such as defects, and will be explored in Chapter 5. The larger strain possible with the 14M martensite is an attractive feature of these compositions, but understanding the difficulty of magnetic field actuation must be overcome.

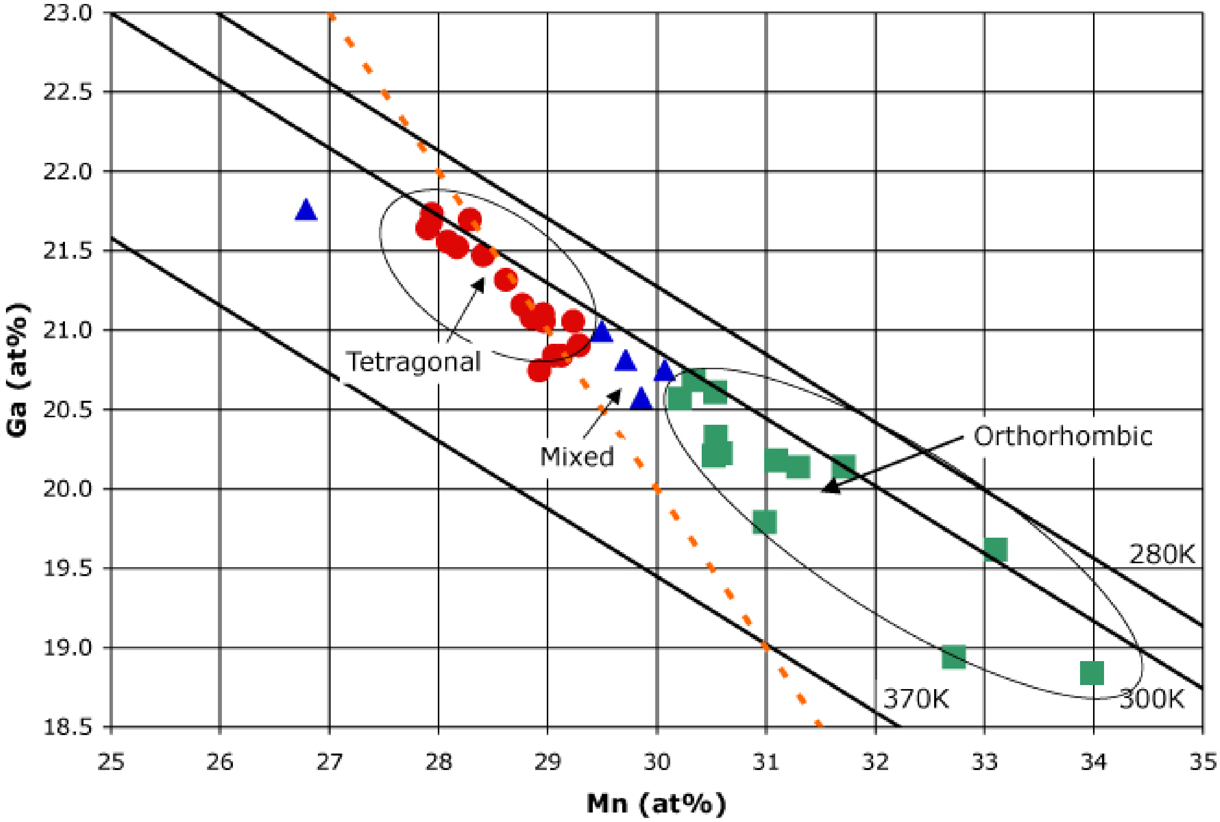

Figure 2-17: Composition dependence of structure for various alloys studied with x-ray diffraction. Solid lines indicate martensite transformation temperatures [10] and dashed line indicates 50 atomic percent nickel.

# Chapter 3

# Martensitic Transformation Behavior

## 3.1 Experimental Details

The Curie and martensitic transformation temperatures of all of the alloy compositions presented in Chapter 2 were measured. These transition temperatures play an important role in assessing the feasibility of using these alloys in devices that require certain operating temperature ranges.

The main tool used to measure these transitions is a vibrating sample magnetometer (VSM). The Curie temperature is easily determined because the paramagnetic to ferromagnetic transition results in a large increase in the magnetization. Due to the reduction of symmetry going from austenite to martensite and the corresponding increase in magnetic anisotropy, the martensitic transition is also easily viewed with the VSM if operated a low field (250–500 Oe). Differential Scanning Calorimetety (DSC) was also used in order to observe the transition behavior without the application of a magnetic field.

Temperature-dependent x-ray diffraction was also employed to explore the structure through the transition. The x-ray experiments were performed on the same samples presented in Chapter 2 through the use of a temperature controlled sample holder. This holder was constructed starting with the standard x-ray powder diffraction sample holder and adding a set of heating resistors to the back plate. These heating elements were then connected to an external temperature controller. In order to ensure the measured temperature was the actual sample temperature, a thermocouple was attached directly to the front face of the sample.

## 3.2 Observed Transition Behavior

Figure 3-1 shows two low-field magnetization versus temperature plots which are representative of those measured on all the alloy compositions studied. It was determined that the alloys that are in the tetragonal (5M) phase at room temperature displayed a much sharper transition than those that are in the orthorhombic (14M) phase. In this case, the terms "sharper" and "broader" refer specifically to the temperature difference between the start and finish of the transition, both for the forward and reverse transformation, i.e. $T_m^s - T_m^f$ and $T_a^s - T_a^f$, where $T_m^s$ is the martensitic transformation start temperature, $T_m^f$ is the martensite finish temperature, $T_a^s$ is the austenite start, and $T_a^f$ is the austenite finish temperature. This difference in transformation width was observed in both powder samples and single-crystals.

To corroborate this finding it was important to measure the same effect in the absence of an external magnetic field, thus removing any possibility that these observations result from a magnetic effect. DSC was performed on several samples of different compositions from each group (5M and 14M) and the representative results are shown in Figure 3-2. This measurement supports the findings from the magnetic measurements.

The temperature-dependent x-ray measurements also revealed a much broader transition in the orthorhombic martensite compared to the tetragonal material. Figure 3-3 shows a set of x-ray patterns taken on a tetragonal sample as it was heated from room temperature. The martensite peaks are indexed with reference to the parent austenite phase. Also, the peaks resulting from the superstructure are indicated and disappear upon heating into the austenite. This confirms their connection to the martensite structure because they disappear concurrently with the fundamental

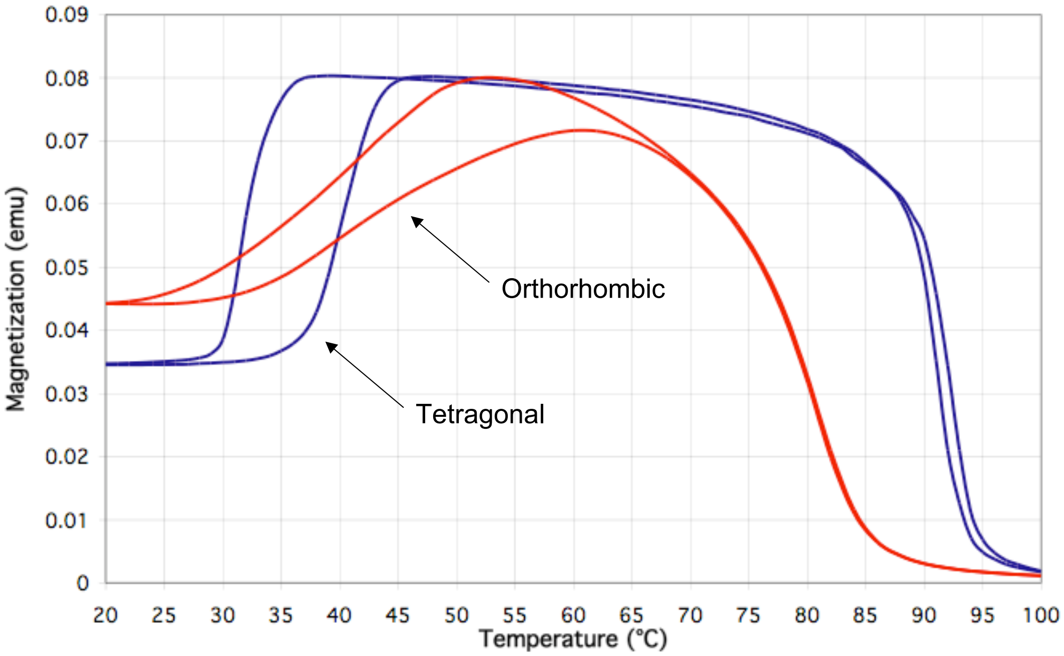

Figure 3-1: Low field magnetization (500 Oe) versus temperature plotted for a tetragonal and orthorhombic sample.

martensite peaks. Figure 3-4 shows a similar set of patterns from an orthorhombic sample. Here the transition is seen to occur over a much larger temperature range. This can be clearly seen when a small area of each is compared as is shown in Figure 3-5.

When the data from all samples are tabulated, as shown in Figure 3-6, it is clear that the difference in transformation is connected to the martensite crystal structure rather than the chemical composition. The change from the sharper to the broader transition is abrupt and does not change smoothly with sample composition. The orthorhombic transitions consistently exhibit transformations which are 10–15°C wider than those observed in the tetragonal martensite.

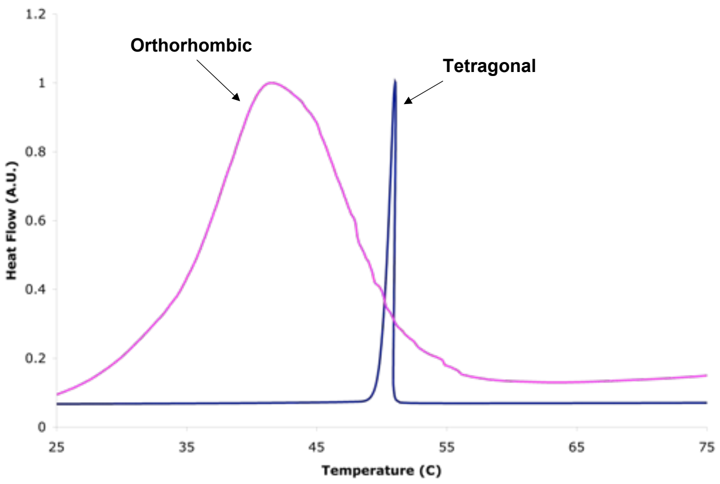

Figure 3-2: DSC curves for a tetragonal and orthorhombic sample showing a much broader transition in the orthorhombic phase. The vertical axis has been scaled to allow for comparison between the two curves.

## 3.3 Interpretation of Results

One possible cause of the broader transitions could be inhomogeneities in the sample composition. If each sample had portions that begin to transform at different temperatures, the expected bulk transition would be broader. However, each sample was prepared from a small portion of single crystal which was determined to have a uniform composition. Also, all the samples were checked after the heat treatment and neither the tetragonal nor the orthorhombic had significant variation in composition. Additionally, tetragonal and orthorhombic samples taken from the same single crystal also showed the same differences in the transformation behavior.

Several studies have revealed many inter-martensitic transformations in different alloy compositions [42, 76, 77, 78, 79]. In some compositions, the tetragonal 5M martensite transformed to the 14M orthorhombic structure at lower temperatures, and when further cooled transformed into the non-modulated structure. The broadness in the transition observed in the orthorhombic martensites could be the result of these types of inter-martensitic transformations occurring at relatively close temperatures. However, the x-ray data presented previously does not indicate the presence of an intermediate phase in either set of samples. The transitions are from the parent

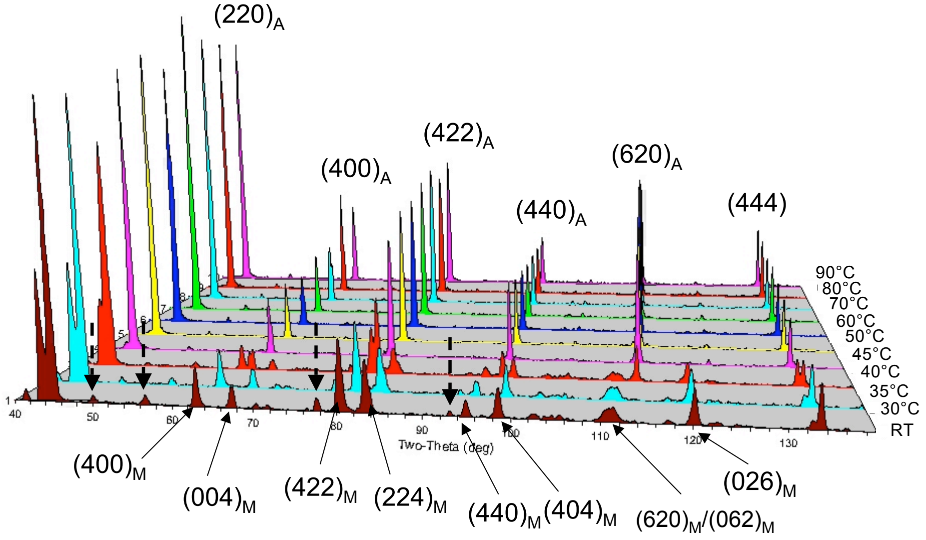

Figure 3-3: X-ray patterns taken at various temperatures for a sample exhibiting the 5M martensite at room temperature. Dashed arrows indicate peaks associated with the periodic structure. Note: Martensite indexing is referenced to distorted austenite structure.

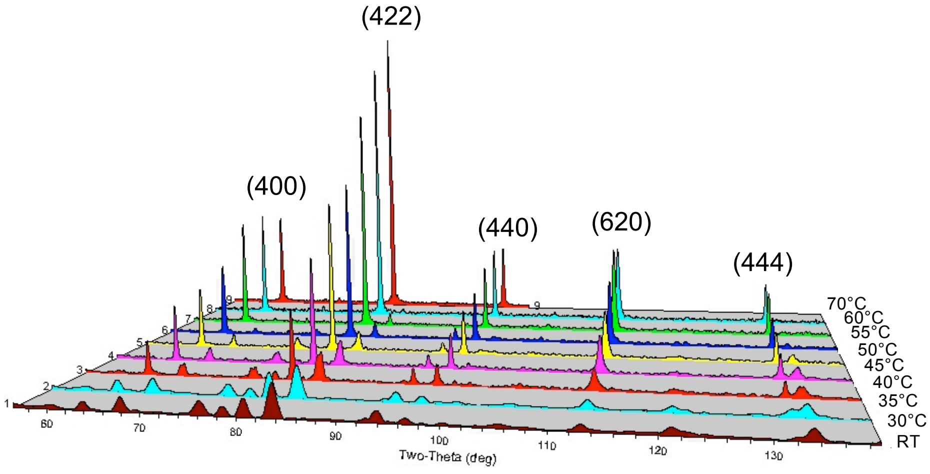

Figure 3-4: X-ray patterns taken at various temperatures for a sample exhibiting the 14M martensite at room temperature.

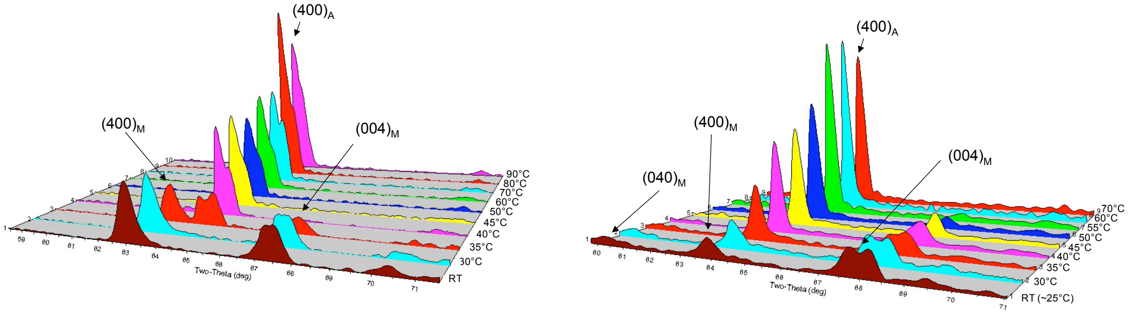

(a) (b)

Figure 3-5: X-ray diffraction patterns taken at various temperatures for (a) 5M and (b) 14M martensites focusing on peaks evolving from the $(400)_A$ peak.

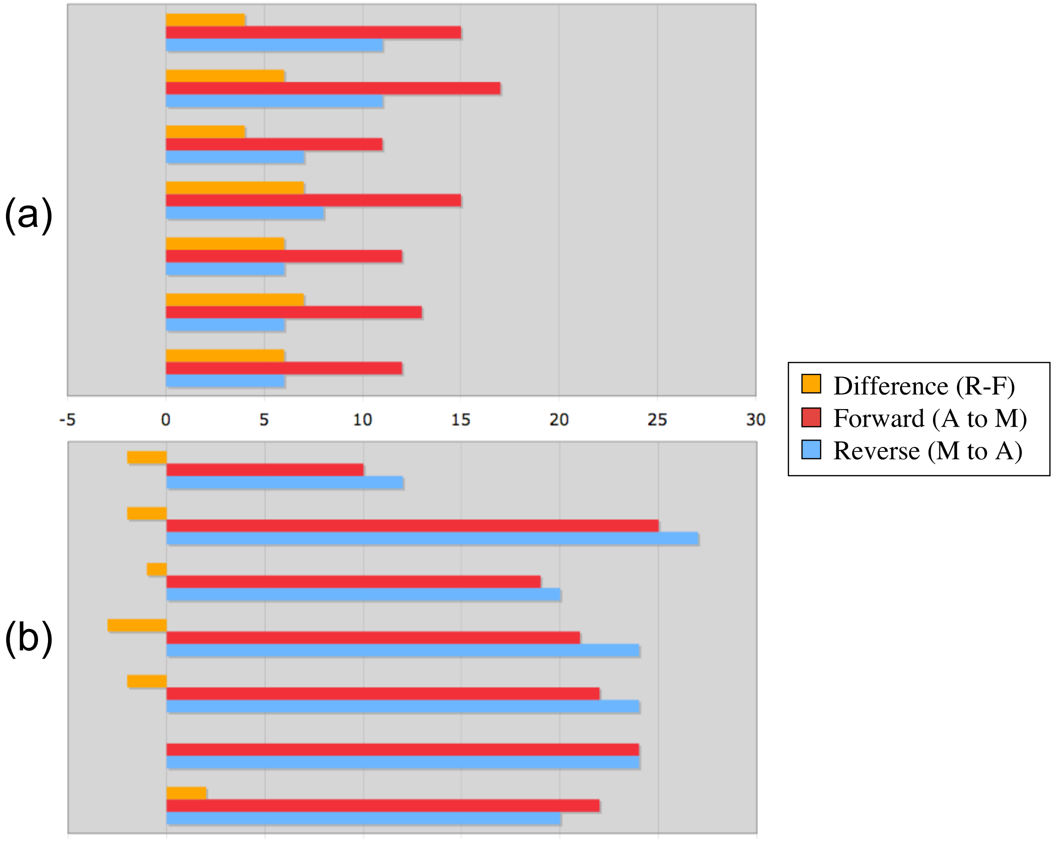

Figure 3-6: Plot showing the forward, reverse transformation widths in degrees Celsius and the difference between the two for (a) tetragonal (5M) and (b) orthorhombic (14M) samples. Each set of bars represents data from one sample.

cubic phase directly to the tetragonal or orthorhombic martensite.

Another possible source of the difference in transformation behavior could be a large degree of incompatibility between the austenite and martensite due to a large volume change. James and Hane present two criteria on the transformation matrix, also known as the lattice deformation or the Bain strain, that indicate the degree of lattice compatibility between the two phases [45]. This approach is used in the search for low hysteresis shape-memory alloys [80], but also could be related to the width of the forward and reverse transition.

The martensitic transformation matrix for each phase can be written as:

$$U_{\text{tetragonal}} = \begin{pmatrix} \alpha & 0 & 0 \\ 0 & \alpha & 0 \\ 0 & 0 & \beta \end{pmatrix} \tag{3.1}$$

$$U_{\text{orthorhombic}} = \begin{pmatrix} \alpha & 0 & 0 \\ 0 & \beta & 0 \\ 0 & 0 & \gamma \end{pmatrix} \tag{3.2}$$

where $\alpha$, $\beta$, and $\gamma$ transform the parent austenite into the appropriate martensite unit cell. The first criterion is $\frac{1}{3}\text{Trace}(\mathbf{U}) = 1$, which signifies no change in volume on going from austenite to martensite. The second criterion is that the middle eigenvalue of $\mathbf{U}$ (that is the one of intermediate magnitude of the three) should be as close to unity as possible. When this term is equal to one, an undistorted plane exists between the austenite and martensite, which is what Wayman refers to as “condition A” on the transformation geometry [81]. If this condition is met exactly, an additional shear, known as the lattice invariant shear, is not needed to ensure an invariant plane and only rotation is needed.

Using lattice parameters measured in the austenite and martensite phase, the transformation matrix for each phase can be calculated. The transformation matrices for two particular samples, one tetragonal and one orthorhombic are shown below:

$$U_{TL2-8} = \begin{pmatrix} 1.0184 & 0 & 0 \\ 0 & 1.0184 & 0 \\ 0 & 0 & 0.9614 \end{pmatrix} \tag{3.3}$$

$$U_{TL5-1} = \begin{pmatrix} 1.0506 & 0 & 0 \\ 0 & 0.9999 & 0 \\ 0 & 0 & 0.9473 \end{pmatrix} \tag{3.4}$$

with the corresponding traces calculated to be 0.9994 for the TL2-8 (tetragonal) and 0.9993 for TL5-1 (orthorhombic). These values are both almost equal to one, indicating there is a minimal volume difference between the parent and martensite phase in both structures. The orthorhombic phase does have one eigenvalue close to 1 indicating there is a possibility of a relatively low-energy martensite/austenite interface without the additional lattice invariant shear. However, if all the values of the transformation matrix are considered, the orthorhombic phase has a larger transformation strain (5–6%) compared to a maximum of 4% for the tetragonal.

It appears that none of the rationales presented thus far is able to clearly explain the differences in the observed transition behavior. However, it is possible to view this behavior from a thermodynamic standpoint and build upon previous work in the field of martensitic transformations.

## 3.4 Effect of External Stresses on Martensitic Transformation

Patel and Cohen have presented a thermodynamic framework for understanding the effects of external stress on the martensite start temperature [11]. The initial assumption in their model is that the martensitic transformation begins when the driving force reaches a critical negative value. In the absence of external stresses, the driving force is due to the chemical free energy difference of the two phases and can be written as:

$$\Delta G = G_M - G_A \tag{3.5}$$

As the material is cooled below the temperature at which the free energies of both phases are equal, $T_\circ$, the driving force increases. A schematic plot of this is shown in Figure 3-7. In the unstressed case, the critical driving force is reached at $T = T_m^s$ and the transformation begins.

Under an applied stress, there is an additional energy contribution which can either add or subtract energy from the chemical driving force. It is necessary to compute the work done by the external stress which Patel and Cohen define as $U$. This work is comprised of two terms, the shear stress resolved along the potential habit plane in the direction of shear and the normal stress resolved perpendicular to the habit plane. This can be written as:

$$U = \tau\gamma_\circ + \sigma\epsilon_\circ \tag{3.6}$$

where $\tau$ is the applied shear stress resolved along the habit plane, $\gamma_\circ$ is the transformation shear strain, $\sigma$ is the resolved normal stress, and $\epsilon_\circ$ is the normal component of the transformation strain. With this expression it is possible to calculate the maximum work done by an external stress for a particular orientation of martensite. Denoted $U_{max}$, this energy can either add to or subtract from the chemical driving force to either stabilize the martensite or austenite. In Figure 3-7, $U_{max}$ is negative, thus shifting the curve representing the driving force down. This results in the critical driving force being reached at a smaller undercooling and thus raises the transformation start temperature to $M_s'$.

Using this approach, Patel and Cohen were able to calculate the shift in start temperature for several simple stress states, such as uniaxial tension and compression. This work was further expanded by Todinov et al. to include multiple variant orientations and more complex stress states [82]. However the original approach is still a useful starting point in trying to explain the transition behavior observed in Ni–Mn–Ga alloys.

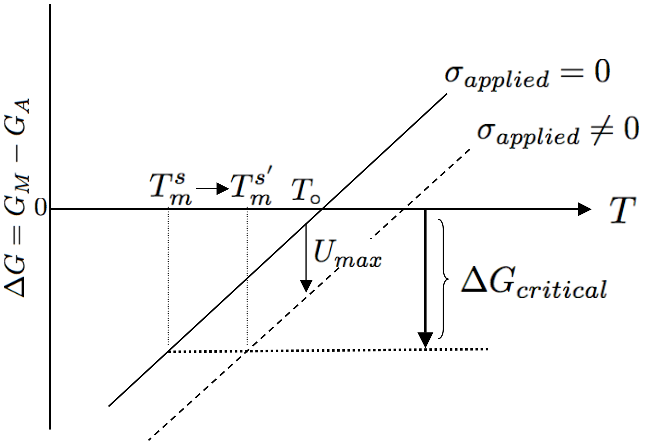

Figure 3-7: Schematic plot demonstrating the affect of external stress on the thermodynamic driving force for the martensite transformation. Here $\Delta G_{critical}$ is the critical driving force required to begin the transformation and $U_{max}$ is the contribution of the applied stress to the free energy of the system (after Patel and Cohen [11]).

## 3.5 Thermodynamic Explanation of Observed Behavior

To begin to explain the observed differences in transformations in the tetragonal and orthorhombic martensites, the free energies of the two phases can be approximated as linear functions of the temperature:

$$G_A = G_A^\circ - m_A T \tag{3.7}$$

$$G_M = G_M^\circ - m_M T + f\Gamma_\sigma \tag{3.8}$$

Here an extra term is added to the martensite energy to account for additional strain energy affects. In this term, $f$ is the volume fraction of material transformed to martensite and $\Gamma_\sigma$ is the extra contributions to G that arise from any strain energy due to the transformed material. This extra energy can arise from a large transformation strain which translates to a large strain across the austenite/martensite interface. It could also result from incompatible variants that form in different locations in the material and then impinge on one another.

Using this framework, the total driving force for the martensitic transformation can be written as the difference in these two energies, namely:

$$\Delta G = G_M - G_A = (G_M^\circ - G_A^\circ) - (m_M - m_A)T + f\Gamma_\sigma \tag{3.9}$$

This expression can be further simplified by using the fact that the driving force vanishes at $T_\circ$ and this the expression for $\Delta G$ simplifies to:

$$\Delta G = (m_M - m_A)(T_\circ - T) + f\Gamma_\sigma \tag{3.10}$$

Equation 3.10 for the driving force is consistent with the thermodynamic behavior through the transition. As the undercooling is increased, the driving force increases (becomes more negative) since the energy difference between the two phases increases. However, the additional term which is a function of the volume transformed acts to decrease the driving force as material transforms, thus requiring further cooling to retain the critical driving force and continue the transformation.

Figure 3-8 is a schematic representation of the proposed thermodynamic behavior that occurs during the transformation. The linear variation of the free energies of the austenite and martensite with no elastic energy effects are plotted as a function of temperature. When the critical driving force, $\Delta G_{critical}$, is reached the transformation begins. The $f\Gamma_\sigma$ term causes an increase in the martensite energy and thus reduces the driving force. The reduction of driving force results in a need for further undercooling to continue the transformation. This treatment is similar to the Patel-Cohen approach to external stress. However, in this case the extra energy term included in the driving force is not static but changes as more material transforms. The proposed model is only valid for austenite transforming to multi-variant martensite. The proposed behavior would not be applicable to a single-interface transition into a single-variant martensitic state. The transition behavior measured in the experiments described previously are multi-variant transformation because no external stress or field has been applied to influence the transforming material.

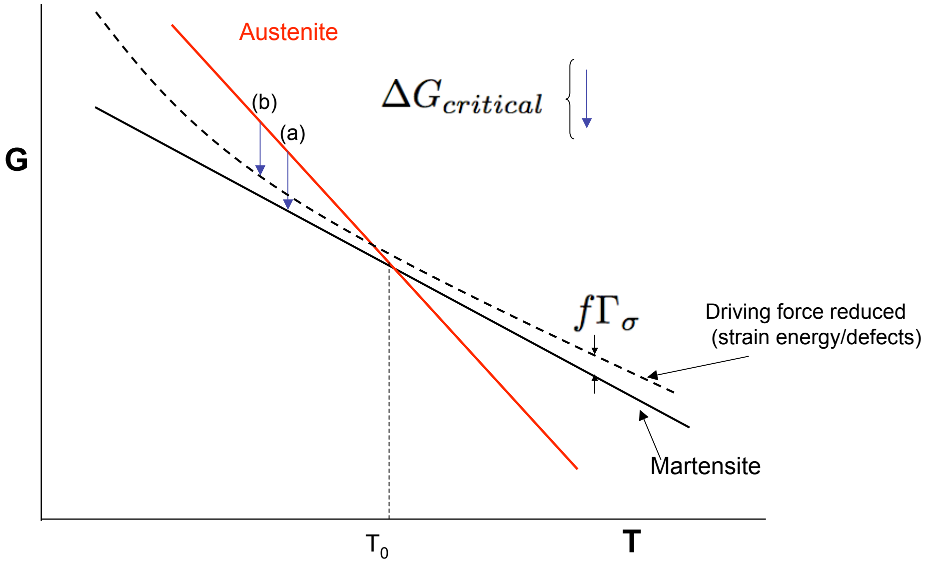

Figure 3-8: Schematic plot showing the strain energy effects which can depend on the fraction of material transformed. The critical driving force could be reached by undercooling to (a), but once the transformation begins, the strain energy can then raise the energy of the martensite phase, reducing the driving force, and requiring a further undercooling to (b) in order to continue the transformation.

This approach explains why thermoelastic martensitic transformations generally do not occur as a spontaneous avalanche once the critical undercooling is reached (the exception being the so-called autocatalytic or"burst transtion" seen in Fe–Ni and other alloys [83, 84]). The transformation will occur gradually over a range of temperatures due to the accumulation of elastic energy that raises the energy of the martensite. Using this approach, the dissimilar transition behavior seen in Ni–Mn–Ga can be attributed to different values of the parameter $\Gamma_\sigma$ for the tetragonal and orthorhombic martensites. The orthorhombic phase exhibits a much larger transformation strain of 5-6% compared to a maximum of 4% in the tetragonal structure. This larger strain could result in interfaces that would be more difficult to move due to the larger elastic energy. In the orthorhombic martensite, there is an additional set of twin planes due to the unique $b$-axis which could lead to more stress being relieved through twinning. However, this could also lead to the intersection of incompatible twin variants, thus locking up the twins and preventing further relief of the transformation strain. The resulting transition in the orthorhombic phase would have to be much broader due to the larger strain energy effects requiring additional undercooling.

Figure 3-9 shows a schematic representation of the effects of changing the $\Gamma_\sigma$ parameter on the character of the martensitic transformation. If the effects of strain energy are ignored, i.e. $\Gamma_\sigma = 0$, then once the critical driving force is reached, the transition would occur in a very sharp manner and would not require additional undercooling to sustain. If $\Gamma_\sigma$ is then increased, the transition would then become broader because the driving force is reduced once material begins to transform. With a further increase the effect continues to widen the transition. Using the arguments presented above, the effects of strain energy would be larger in the orthorhombic phase yielding a much broader transition.

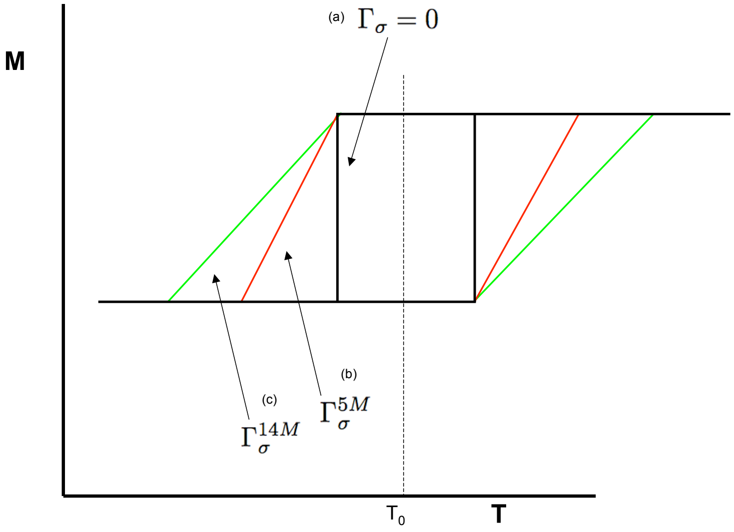

Figure 3-9: Schematic representation of a magnetization versus temperature plot through the martensite transformation for different magnitudes of the strain energy parameter $\Gamma_\sigma$. When only the chemical driving force is considered (a) the transition is quite sharp. For the tetragonal, 5M, marteniste (b) the strain energy effect broadens the transition slightly. The orthorhombic, 14M, (c) has a much larger strain energy contribution and thus has a much broader transition.

# Chapter 4

# Chemical Ordering and Neutron Diffraction

## 4.1 Structure Factor Calculation

The structure factor for the $L2_1$ ordered phase can be calculated starting with the standard equation:

$$F_{hkl} = \sum_{1}^{N} = f_n e^{2\pi i(hu_n + kv_n + lw_n)} \tag{4.1}$$

where $u_n$, $v_n$, and $w_n$ are the atomic positions of the $n$th atom inside the unit cell and $f_n$ is the atomic scattering factor of the $n$th species. For $Ni_2MnGa$ these positions are given in Table 4.1. Using these values, a set of selection rules for various $hkl$ planes can be determined and are shown in Table 4.2.

The rules for allowed reflections are similar to those for a disordered FCC ($A1$) structure. As expected, planes with mixed $hkl$ indices (Type I) are forbidden. In contrast to the FCC structure, the structure of Ni–Mn–Ga is ordered and the allowed diffraction peaks have various intensities depending on their $hkl$ indices. For planes with all odd indices (Type II), the structure factor involves only the atomic scattering factors of Mn and Ga. Thus these peaks are associated with the $L2_1$ (Mn and Ga) ordering. When $h$, $k$, and $l$ are all even, there are two possible forms of $F_{hkl}$ depending on the sum of the indices. If the sum of $h$, $k$, and $l$ is a multiple of two (Type III),

Table 4.1: Atomic positions in the $L2_1$ structure used in the structure factor calculation.

| | u | v | w |
|---|---|---|---|
| Mn | 0 | 0 | 0 |
| | 0 | 1/2 | 1/2 |
| | 1/2 | 0 | 1/2 |
| | 1/2 | 1/2 | 0 |
| Ga | 1/2 | 1/2 | 1/2 |
| | 1/2 | 1 | 1 |
| | 1 | 1/2 | 1 |
| | 1 | 1 | 1/2 |
| Ni | 1/4 | 1/4 | 1/4 |
| | 1/4 | 3/4 | 3/4 |
| | 3/4 | 1/4 | 3/4 |
| | 3/4 | 3/4 | 1/4 |
| | 1/4 | 1/4 | 3/4 |
| | 1/4 | 3/4 | 1/4 |
| | 3/4 | 1/4 | 1/4 |
| | 3/4 | 3/4 | 3/4 |

Table 4.2: Selection rules calculated from the structure factor for the $L2_1$ structure. Notice that because of the values of $f$ for Ni, Mn, and Ga some permitted reflections will be absent.

| Type | Miller Indices | Example | $F_{hkl}$ | F ($\theta = 0$) | Order Type |
|---|---|---|---|---|---|
| I | $h$,$k$,$l$ mixed | (001) | 0 | 0 | - |
| II | $h$,$k$,$l$ all odd | (111) | $4f_{\mathrm{Mn}} - 4f_{\mathrm{Ga}}$ | 24 | $L2_1$ |
| III | $h$,$k$,$l$ all even<br>$h + k + l = 2n$ | (200) | $4f_{\mathrm{Mn}} + 4f_{\mathrm{Ga}} - 8f_{\mathrm{Ni}}$ | 0 | $B2$ |
| IV | $h$,$k$,$l$ all even<br>$h + k + l = 4n$ | (220) | $4f_{\mathrm{Mn}} + 4f_{\mathrm{Ga}} + 8f_{\mathrm{Ni}}$ | 448 | Fundamental |

then the structure factor is proportional to difference between $f_{\mathrm{Mn}}+f_{\mathrm{Ga}}$ and $f_{\mathrm{Ni}}$. This is in contrast to the case where the sum is a multiple of four (Type IV), where $F_{hkl}$ involves a sum of $f_{\mathrm{Mn}}$, $f_{\mathrm{Ni}}$ ,and $f_{\mathrm{Ga}}$. These two sets of peaks (Type III and Type IV) arise from the $B2$ ordering, thus they involve all of the atomic scattering factors.

In the case of $Ni_2MnGa$, the form of the structure factor and selection rules do not fully illuminate the expected diffraction behavior. In order to determine what the expected x-ray diffraction pattern might look like, it is important to look at each of the selection rules and calculate $F_{hkl}$ using atomic scattering factors. When this is done for the stoichiometric alloy composition, additional peaks may effectively vanish due to the similarity of the atomic x-ray scattering factors of Ni, Mn, and Ga. Type II peaks, such as (111), will have an extremely weak intensity compared with the strongest peaks, namely Type IV peaks, for example (220). This effect is even more dramatic in the case of Type III peaks, where the intensity is almost zero.

Table 4.2 shows the value of $F_{hkl}$ for each peak type when $\theta = 0$, namely when the atomic scattering factor is equal to the atomic number. Figure 4-1 expands on this by displaying plots of the calculated intensities for each peak type as a function of $2\theta$. Here, the intensities are approximated as proportional to $F_{hkl}^2$ multiplied by the Lorentz polarization factor. From this plot it is evident that the majority of the peaks present in any x-ray or electron diffraction pattern of Ni–Mn–Ga will be peaks of Type IV, with the possibility of some weak Type II peaks at low diffraction angles.

The similarity in atomic scattering factors makes it extremely difficult to obtain much information about chemical ordering from x-ray diffraction measurements. However, neutron diffraction does not have the same limitation because of different values for the scattering cross-sections of Ni, Mn and Ga. Unlike the atomic scattering factor for x-ray and electron diffraction, which depend mostly on atomic number, the neutron scattering cross-sections vary independently from atomic number. Also, the neutron scattering power is not a function of diffraction angle. As seen in Table 4.3, the cross-sections of Ni, Mn, and Ga are very different and thus will allow all three types of peaks to be observed.

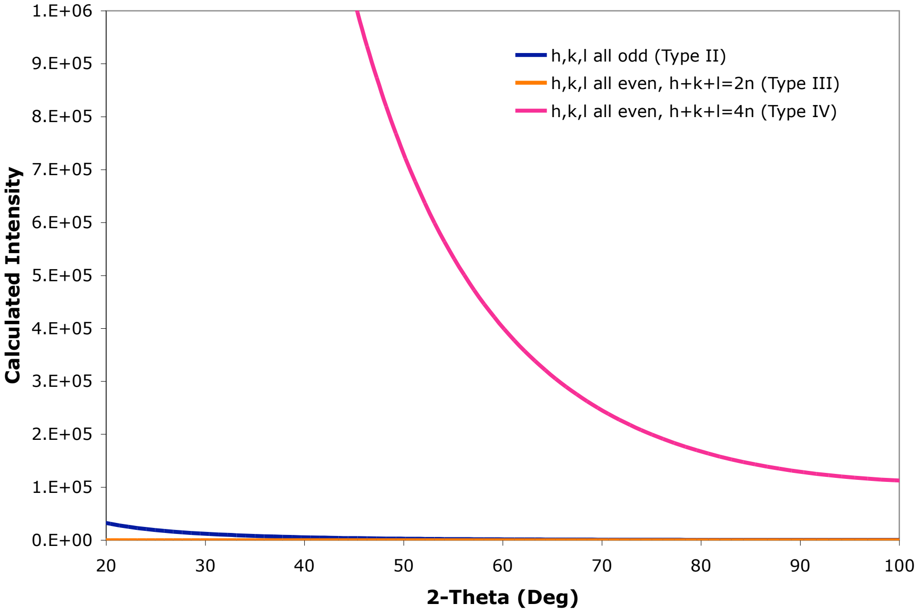

Figure 4-1: Comparison of expected x-ray diffraction peak intensities calculated for the three different peak types determined from the selection rules. The intensity is assumed to be proportional to $F_{hkl}^2 * LP$ where LP is the Lorentz polarization.

Table 4.3: Coherent neutron scattering length and cross-section for Ni, Mn and Ga [14].

| Element | Coherent Scattering Length (fm) | Coherent Scatting Corss-section (barn) |
|---|---|---|
| Mn | -3.73 | 1.75 |
| Ni | 10.3 | 13.3 |
| Ga | 7.288 | 6.675 |

## 4.2 Simulation of X-ray And Neutron Diffraction

Simulations using Cerius2 © were performed in order to determine the changes in the diffraction pattern that might be observed as the chemical order and composition of alloys are changed. The initial simulations were done on the stoichiometric compositions using the simplified tetragonal unit cell. A super-cell of 7 by 7 by 7 individual unit cells was used to facilitate the creation of disordered structures. This structure allowed the substitution of one atom type for another, i.e. some Mn atoms placed on some Ni sites.

Figure 4-2 shows two simulated patterns, $Ni_2MnGa$ and an off stoichiometric composition, along with the difference between them. For the off stocihiometry alloy, the excess Mn was placed on Ga sites and Ni was only placed on Ni sites. As expected from the structure factor calculations, the two patterns are extremely similar and the difference pattern is hardly visible. This simulation confirms that x-ray diffraction reveals very little information on the state of order of Ni–Mn–Ga alloys. A similar plot for diffraction with neutrons is shown in Figure 4-3. With neutrons, many more peaks can be seen and intensities that were quite small in x-ray diffraction, like (111), appear quite strong in neutron diffraction. Additionally, a large difference can be observed between the two patterns thus allowing more information to be obtained about the chemical order of off-stroichiometric alloy compositions using neutrons.

The information available from x-ray diffraction about atomic positions and ordering is not completely absent because the weak (111) can be seen in the simulated patterns and also in experimental observations (Chapter 2). Figure 4-4 shows the intensity ratios calculated from simulated x-ray diffraction patterns of alloy compositions with Ni = 50 atomic percent. As was done previously, the excess Mn was added and assumed to occupy Ga sites. As more Mn is added to Ga sites, the intensity ratios of the (111) peak to Type IV peaks (such as (440) and (224)) decrease. These simulated intensity ratios can be compared to experimentally observed intensities for alloy compositions with close to 50 atomic percent Ni.

Figure 4-5 shows the simulated x-ray peak intensity ratios compared with the

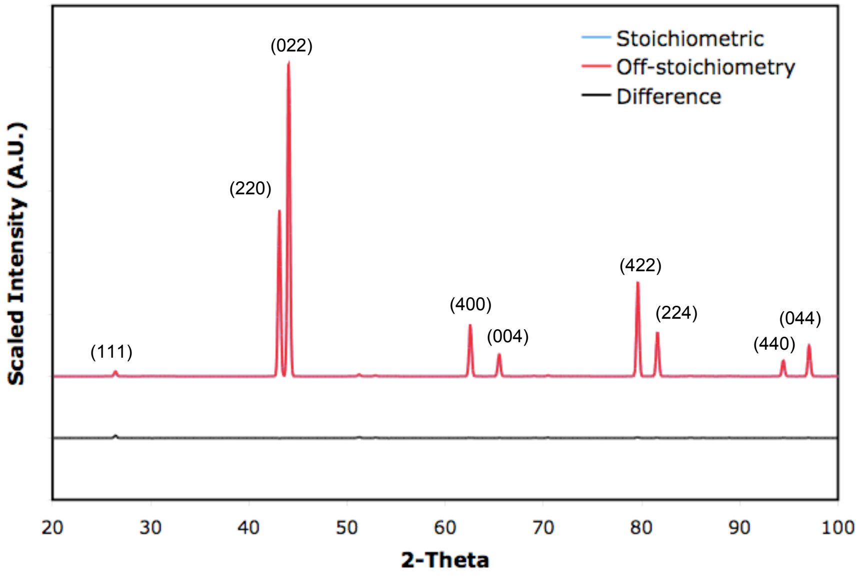

Figure 4-2: Simulated powder x-ray (Cu $K_\alpha$) diffraction pattern from the stoichiometric composition, $Ni_2MnGa$, and an off-stoichiometric composition, approximately $Ni_{50}Mn_{32}Ga_{18}$. The difference between the two is also shown. Note that the two simulated diffraction patterns overlap resulting in a the flat difference curve.

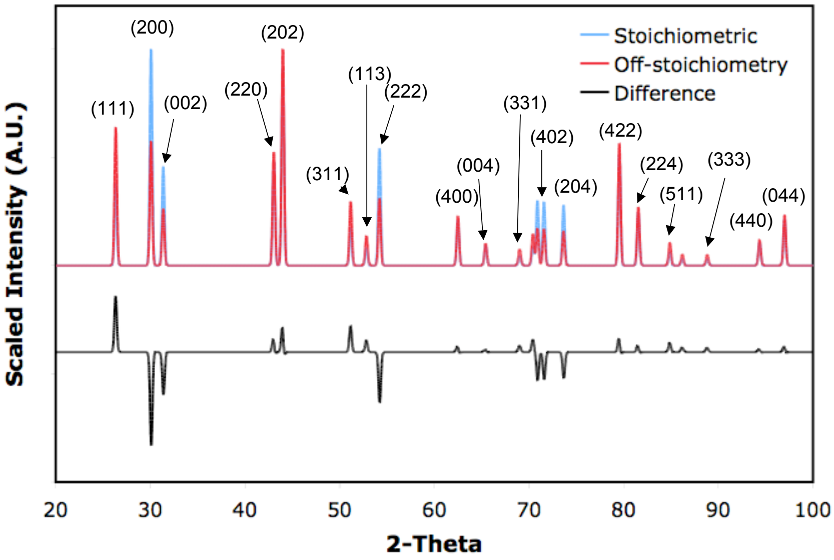

Figure 4-3: Simulated powder neutron ($\lambda = 1.54\mathring{A}$) diffraction pattern from the stoichiometric composition, $Ni_2MnGa$, and an off-stoichiometric composition, approximately $Ni_{50}Mn_{32}Ga_{18}$. The difference between the two is also shown.

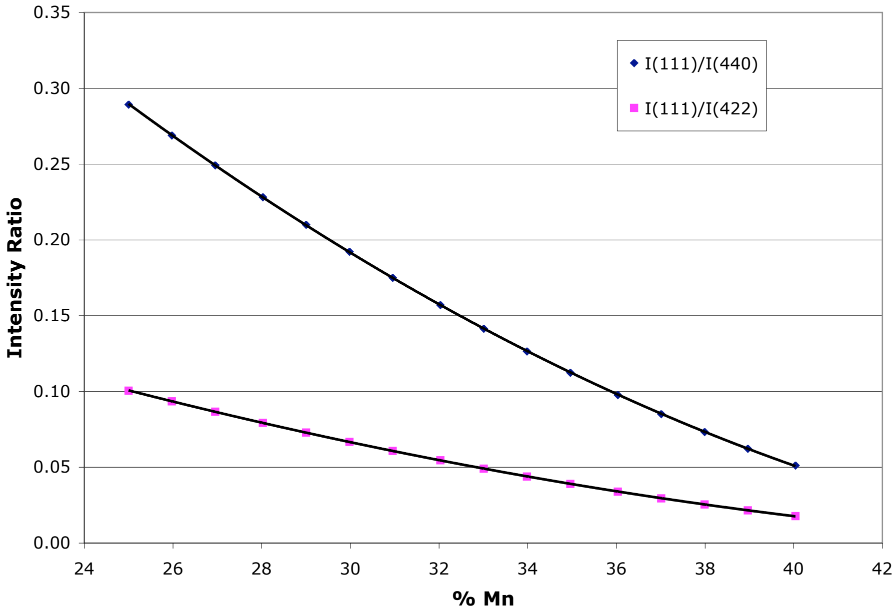

Figure 4-4: Intensity ratios calculated from simulated x-ray diffraction patterns of $Ni_{50}Mn_{25+x}Ga_{25-x}$ alloys. Solid lines show a quadratic fit of the data points.

experimental results for the (111) and (224) peaks. Significant scatter can be seen in the experimental data which can be attributed to the weak intensity of the (111) peak. However, the data are consistent with the trend predicted from the simulations. The large scatter in the experimental measurements makes it difficult to draw conclusions about the site occupancies and thus signifies the need to use neutrons to help better understand the atomic structure of these alloys.

## 4.3 Previous Neutron Diffraction Studies

The majority of neutron diffraction studies performed on Ni–Mn–Ga alloys has been confined to the stoichiometric composition and the austenite phase. Webster [32] and Soltys [85, 86] performed much of the early work in exploring the room temperature structure of $Ni_2MnGa$, which is austenite. The cubic lattice parameter was measured by Soltys as a function of cooling rate after heat treatment and was found to increase slightly as cooling rate decreased. Also, the disorder of the austenite was characterized

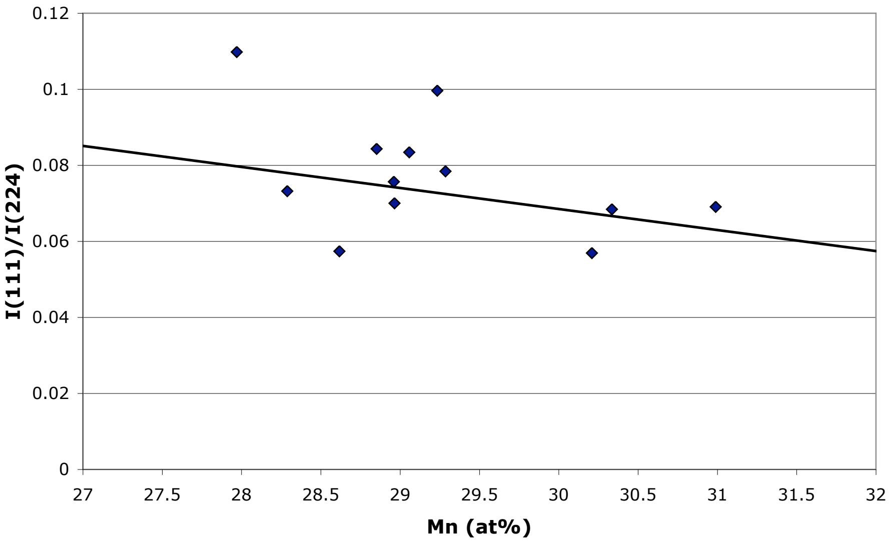

Figure 4-5: Comparison of the simulated x-ray peak intensity ratio (solid line) with experimental data (points, see Chapter 2) for $Ni_{50}Mn_{25+x}Ga_{25-x}$ alloys showing consistency between the simulated and experimental patterns.

as primarily Ni–Ga disorder, which is in contrast to more recent studies. The disorder was seen to increase as cooling rate was decreased. This result is counterintuitive as more order is expected as cooling rate is decreased.

Due to limitations of the diffractometer resolution, the low-temperature martensite phase was not studied extensively until Webster et al. performed further studies in the 1980's [87]. The state of order in the austenitic phase was determined to be 98% of the complete order of the Heusler structure. The low-temperature measurements (4.2K) showed the tetragonal splitting characteristic of the martensite phase. Also, several low-intensity peaks were observed which the authors attributed to superstructure with a long periodicity, i.e. the 5 and 7-layer martensitic phases mentioned previously. Webster also confirmed that the magnetic moment resides mostly on the Mn sites, however it is noted that it is possible that there is a small moment located on Ni sites.

Overholser et al. have reported a study of the ordering transition observed upon cooling several different Ni–Mn–Ga alloy compositions from temperatures above the melting temperature (about 1600 K) to around 400 K [12]. They combined neutron diffraction with DTA measurements to estimate the ordering transition temperatures and the degree of chemical order. Figure 4-6 shows the quasibinary diagram they constructed with their data. The authors observed the $B2$ to $L2_1$ transition to be very rapid. Samples which were quenched from temperatures where the $B2$ structure is stable showed a high degree of $L2_1$ when analyzed after quenching. Thus the $B2$ structure is not easily retained in these alloys, which is in contrast to earlier studies by Webster and Soltys.

No neutron diffraction patterns are presented in the published report. No systematic room temperature measurements of different alloy compositions were performed. The authors also focused only on compositions with 50 atomic percent nickel and various Mn/Ga ratios.

More recently, Glavatska et al. have reported neutron diffraction work with an off-stroichiometric composition, namely $Ni_{49.8}Mn_{28.5}Ga_{21.7}$ in the martensitic state [88]. They determined that this composition displays the 5-layer tetragonal martensitic structure which agrees with the findings from x-ray diffraction presented in Chapter 2. The authors present lattice parameters as a function of temperature calculated from the neutron diffraction patterns. They also show the effect of a magnetic field on the twin variant distribution with the field required for reorientation seen to decrease with increasing temperature. It appears that similar information could have been obtain from x-ray diffraction and that the unique information which could be obtained with neutrons was not addressed.

## 4.4 Experimental Details

Several different compositions were chosen for powder neutron diffraction analysis in an effort to cover the composition range analyzed previously with x-rays (Chapter 2). The compositions selected are shown in Figure 4-7. As in the x-ray studies, powders were prepared by manually crushing single-crystal pieces in order to obtain at least 1 gram of powder. Pieces of single crystal with homogeneous composition were used. After crushing, powders were heat treated for 4 hours at 650°C as a stress relief.

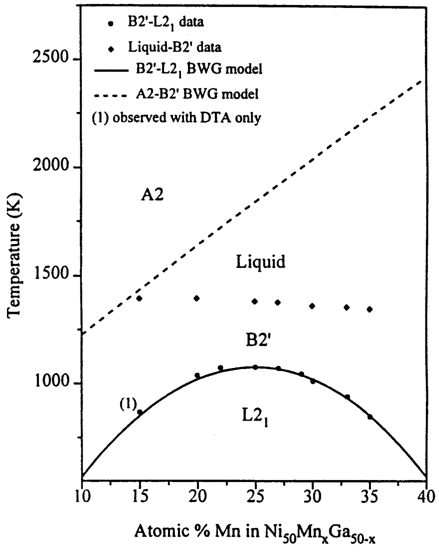

Figure 4-6: Quasi-binary temperature-composition diagram for $Ni_{50}Mn_xGa_{1-x}$ measured using DTA neutron diffraction, from Overhosler, et al. [12]. The solid lines indicate phase boundaries calculated with a Bragg–Willaims–Gorsky-type model.

Compositions were confirmed after heat treatment to ensure homogeneity.

One single-crystal composition (TL11 in Figure 4-7) was selected for analysis by single-crystal neutron diffraction. Only a single composition could be studied due to the longer time required for measurements of single crystals compared to powders. A rectangular prism of 3 mm by 3 mm by 1.5 cm was cut from the large single-crystal boule by electric discharge machining (EDM). This piece was then heat treated at 900°C for 24 hours and then at 500°C for 3 hours in a sealed quartz tube under argon atmosphere. The sample was then cooled to 200°C, removed from the quartz tube, and allowed to cool through the martensitic transition under a load of approximately 5 MPa. This final cooling step was performed in order to ensure the crystal was in a single-variant state. Small cubes of 3 mm by 3 mm by 3 mm were then cut using a EDM with a fine wire.

Neutron diffraction measurements were performed at the Institut Laue-Langevin (ILL) in Grenoble, France. The single-crystal analysis was done on the D10 (Figure 4-8) instrument equipped with a 4-circle goniometer, heating capability of up to 400

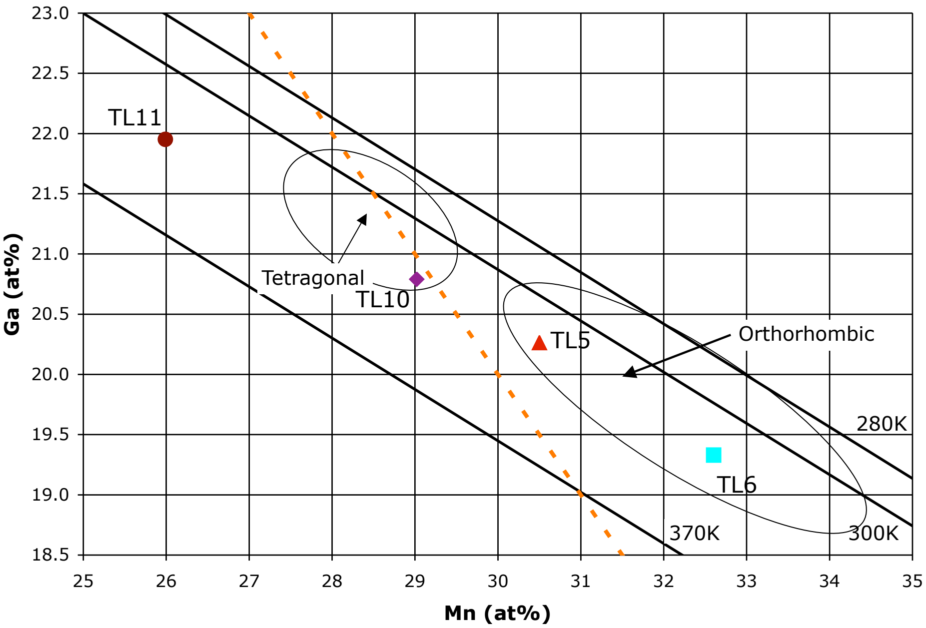

Figure 4-7: Composition of powders used for neutron diffraction at ILL.

K, and a neutron wavelength of 1.25 Å. The powder diffraction was performed on the high-flux D20 (Figure 4-9) instrument with a position-sensitive microstrip gas-detector covering an angular range of about 150 degrees in $2\theta$, with a resolution of 0.1 degrees. The wavelength used was 1.37 Å. Data analysis was performed using CrystalDiffract © for the preliminary intensity analysis and GSAS and TOPAS © for structure refinement [89].

## 4.5 Preliminary Results

### 4.5.1 Powder Neutron Diffraction

Room-temperature powder neutron diffraction data from the four samples is shown in Figure 4-10. As expected, all of the samples are martensitic at room temperature as can been seen from the number of peaks present in the pattern. Two of the samples (TL 10 and 11) are tetragonal and two are orthorhombic (TL5 and 6) as predicted in Figure 4-7. The peaks are indexed with reference to the parent cubic unit cell. Peaks such as (200) and (022) can be seen to split when the symmetry is reduced from

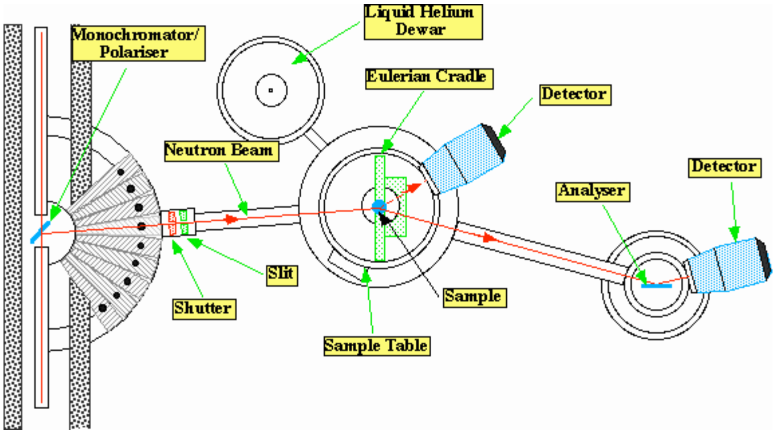

Figure 4-8: Experimental setup of the D10 diffractometer used for single-crystal neutron diffraction measurements [13].

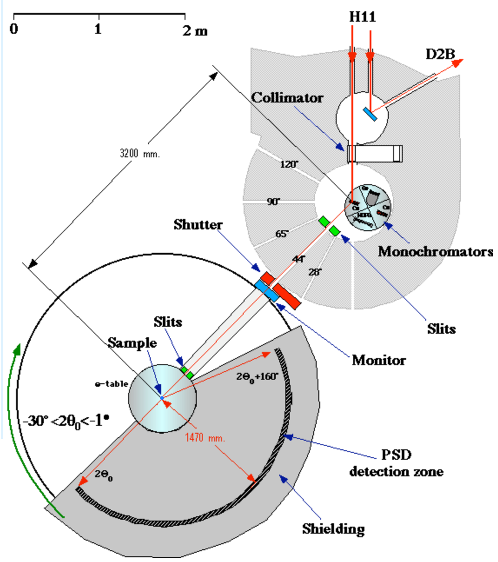

Figure 4-9: Experimental setup of the D20 high-flux diffractometer used for neutron powder diffraction measurements [13].

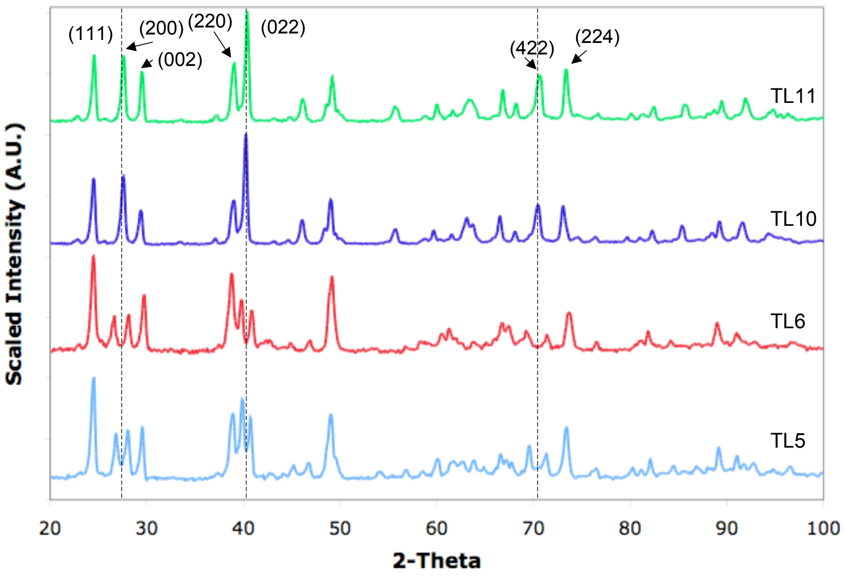

Figure 4-10: Powder neutron ($\lambda = 1.37$ Å) diffraction patterns from each sample. There are two tetragonal samples and two orthorhombic. Indexing has been done with reference to the austenite unit cell. Dashed lines indicate some of the peak splitting due to the reduction in symmetry. Intensities have been scaled and the baseline is offset for each sample.

tetragonal to orthorhombic. Additional peaks are present due to the superstructure as was also seen in x-ray diffraction (Chapter 2).

In order to compare x-ray and neutron diffraction measurements, the diffraction angle ($2\theta$) was converted to interplanar spacings by using the appropriate radiation wavelength. This conversion allowed for the plotting of the measured patterns versus $1/d$ which is independent of wavelength. Figures 4-11 and 4-12 show a comparison of the x-ray and neutron diffraction measurement for two samples; TL10 is tetragonal while TL5 is orthorhombic. Again the peaks have been indexed with reference to the austenite unit cell. The neutron data requires a zero correction due to misalignment of the detector. It is therefore difficult to obtain precise lattice parameters from the neutron data unless the correction is known. In this case, the pattern was offset to obtain agreement between the x-ray and neutron measurements. As expected, many more peaks are present in the neutron patterns in agreement with the previous simulations (see Section 4.2). Intensities of the peaks are also greater. The x-ray

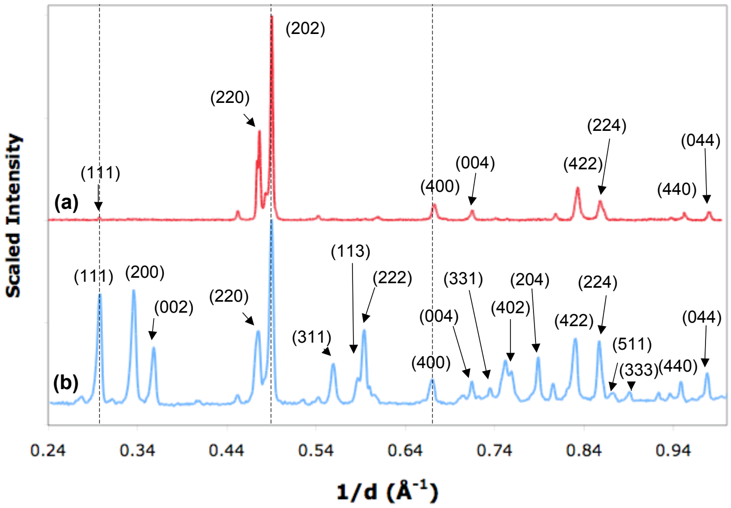

Figure 4-11: Comparison of (a) x-ray and (b) neutron powder diffraction patterns from sample TL10. The neutron pattern has been shifted for zero correction. Indexing has been done with reference to the austenite unit cell. Dashed line indicate some corresponding peaks in two pattern patterns. Intensities have been scaled and the baseline is offset for each sample.

data permit accurate lattice constant determination which will be used later in the structure refinement.

Neutron diffraction patterns of the austenite phase were only collected from three of the four samples due to beam time limitations. The cubic austenite phase has fewer peaks than the martensite and does not contain additional peaks due to a superstructure. Analysis of the austenite data will aid in beginning the refinement of the martensite structure. Also, by measuring the neutron diffraction pattern above the Curie temperature (130–150°C) magnetic scattering by the large Mn magnetic moment is eliminated, further simplifying the structure analysis. The austenite and martensite neutron diffraction pattern from sample TL10 can be found in Figure 4-13. The tetragonal splitting expected from the martensitic transformation as well as the appearance of extra peaks due to the superstructure (Figure 4-14) can be observed.

Initial fits of the austenite patterns were performed with the CrystalDiffraction © software program on samples TL10 and TL5. These two particular compositions were selected because they are the closer to 50 atomic percent nickel which made

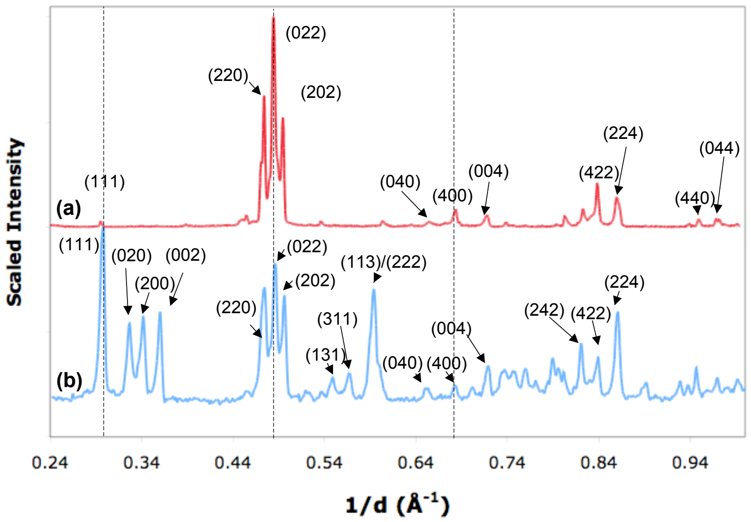

Figure 4-12: Comparison of (a) x-ray and (b) neutron powder diffraction patterns from sample TL5. The neutron pattern has been shifted for zero correction. Indexing has been done with reference to the austenite unit cell. Dashed line indicate some corresponding peaks in two pattern patterns. Intensities have been scaled and the baseline is offset for each sample.

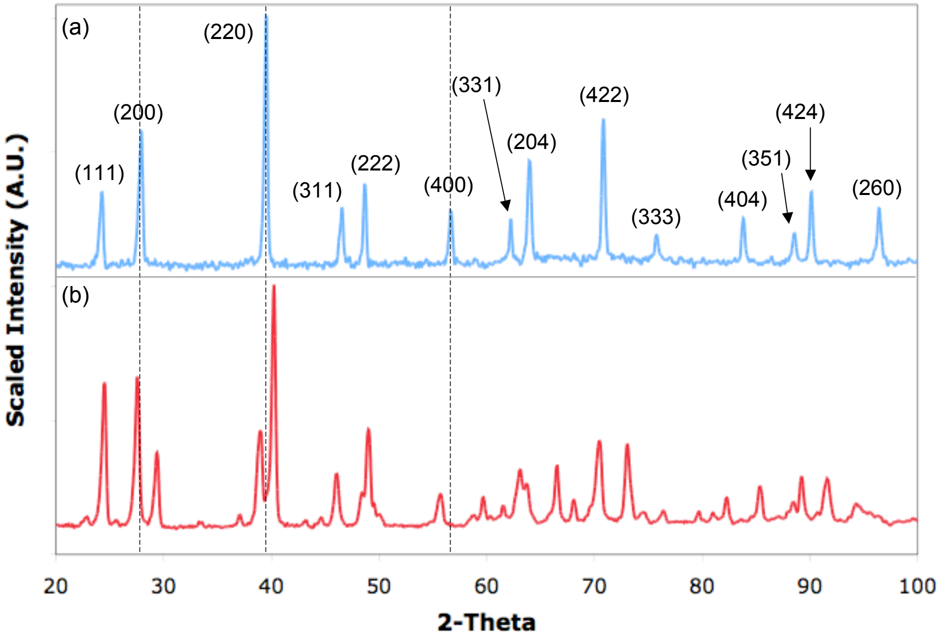

Figure 4-13: Powder neutron diffraction patterns from the (a) austenite phase and (b) martensite phase of sample TL10. Dashed lines indicate some of the peak splitting due to the cubic to tetragonal transformation. Intensities have been scaled and the baseline is offset for each sample.

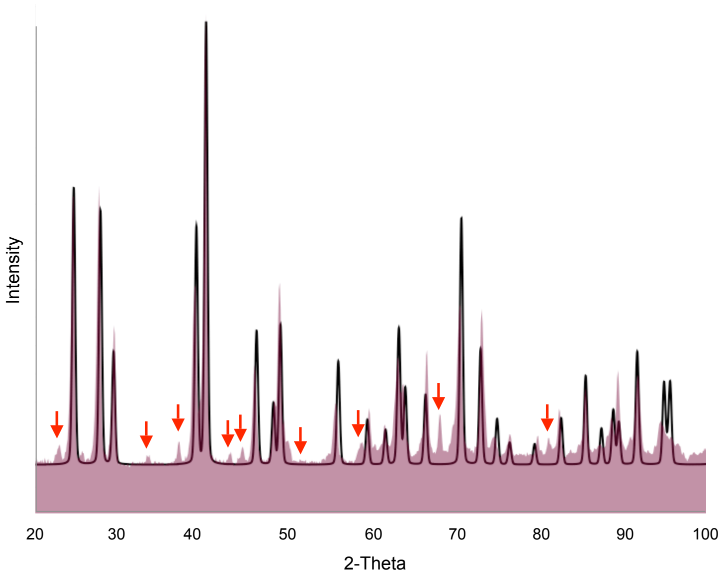

Figure 4-14: Simulated (solid line) and experimental (filled peaks) room temperature neutron diffraction patterns from sample TL10 showing the presence of additional peaks (arrows) arising from the superstructure.

the preliminary analysis much easier. The software allowed for the adjustment of two peak-shape parameters, a simple linear background, and the site occupancies. Sample TL10 is deficient in Ga and the excess Mn and Ni was placed on Ga sites. Sample TL5 is deficient in both Ni and Ga and the excess Mn was placed on Ga and Ni sites. The initial fit is performed assuming no chemical disorder other than that imposed by the off-stoichiometric composition, i.e. no Ga on Mn or Ni sites. The fits for samples TL10 and TL5 are shown in Figures 4-15 and 4-16. A reasonably good agreement between the observed and simulated patterns is obtained in the angular region shown, confirming the previous simulations regarding the expected positions of the excess Mn and Ni. Full pattern fitting of all four samples in the austenite and martensitic phase using the Reitveld method is currently underway and has not been completed.

Sample TL11 was the only sample which contained a significant excess of Ni, about two atomic percent. Figure 4-17 shows the simulated pattern calculated using the same assumptions as with samples TL5 and TL10, namely placing all the excess Ni and Mn on Ga sites. In this case, the simulated pattern matches the intensity of

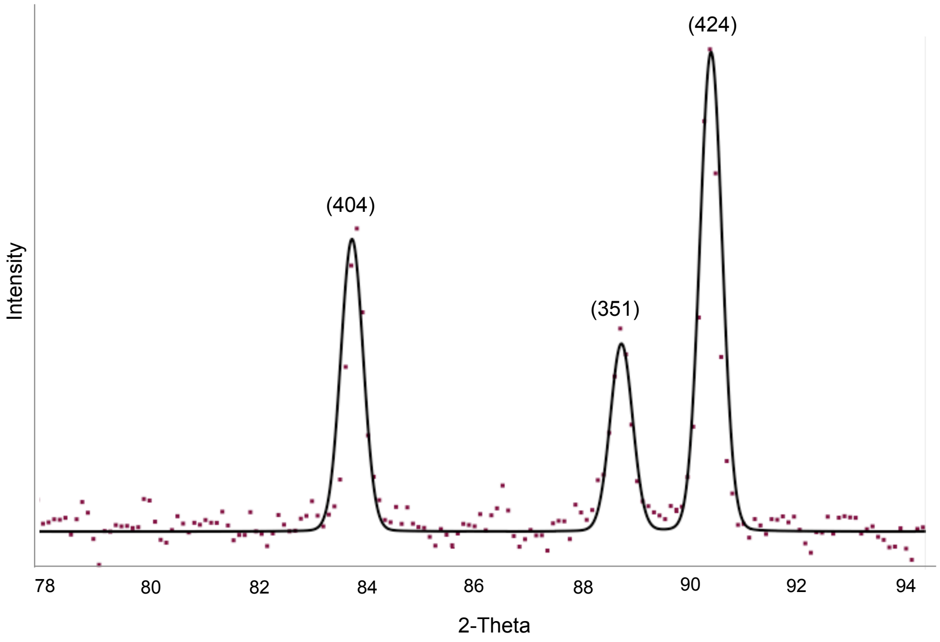

Figure 4-15: Simulated (solid line) and experimental (points) neutron diffraction pattern for sample TL10 ($Ni_{50.2}Mn_{29}Ga_{20.8}$). Indexing shown is referenced to the parent austenite unit cell.

the (404) and (424) peaks, but is not in agreement with the measured intensity of the (351) peak. This may indicate a more complicated site occupation in this alloy and further refinement is necessary. Unfortunately a diffraction pattern in the austenite phase was not collected from sample TL6, which is significantly deficient in Ni (48 atomic percent), due to beam time limitations. Single-crystals cut from TL11 and TL10 have shown magnetic-field induced strain while those from TL5 and TL6 have not. The results obtained so far do not illuminate the difference in the actuation behavior of these two sets of alloys, but further analysis of the existing data and experimentation of more alloy compositions will aid in this determination.

### 4.5.2 Single-Crystal Neutron Diffraction

The aim of the single crystal neutron measurements was to characterize a sample in a single-variant state, heat the sample into austenite and measure again, and then a final measurement after allowing the sample cool back to martensite without any

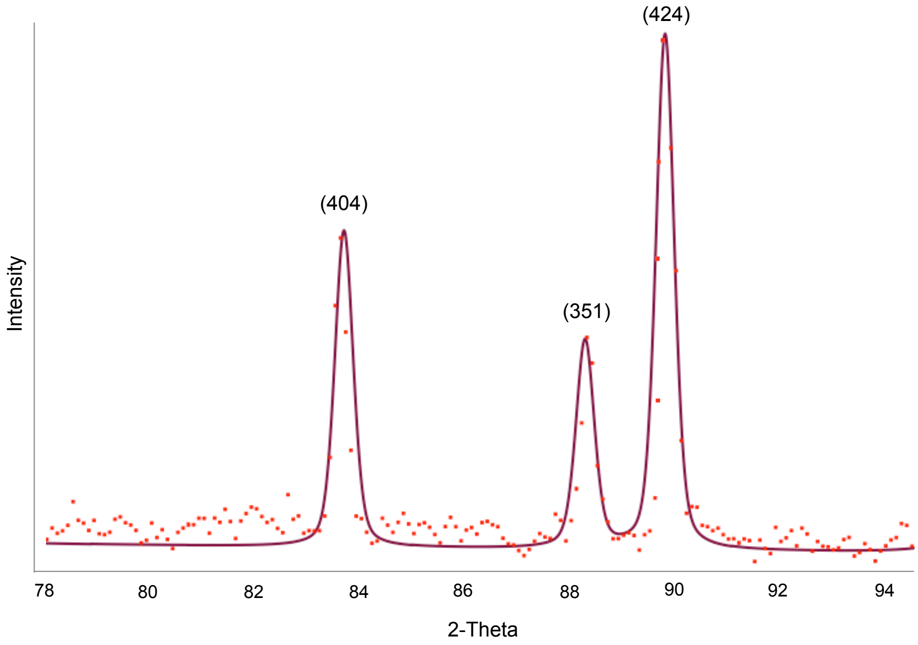

Figure 4-16: Simulated (solid line) and experimental (points) neutron diffraction pattern for sample TL5 ($Ni_{49.2}Mn_{30.5}Ga_{20.3}$). Indexing shown is referenced to the parent austenite unit cell.

external stress or field into a multi-variant state.

Before beginning the single crystal measurements, neutron Laue patterns were collected on the single-crystal sample in order to verify the presence of a single-variant state. The use of neutrons for the Laue diffraction produced a much clearer pattern than obtained with x-rays due to the greater penetrating power of neutrons. Figure 4-19 shows the initial pattern taken with the *c*-axis not aligned properly with respect to the neutron beam. When the sample is rotated with the *c*-axis along the beam direction, the Laue pattern displays the expected four-fold symmetry as seen in Figure 4-20. The two patterns are consistent with a sample in a single-variant state.

The magnetization measurements shown in Figure 4-18 performed on a single-crystal from TL11 also verify that the cube-shaped sample is indeed a single variant. The initial magnetization curve shows no indication of field-induced twin reorganization and has the characteristic shape of an easy-axis magnetization curve. The lower susceptibility is due to the sample shape [90].

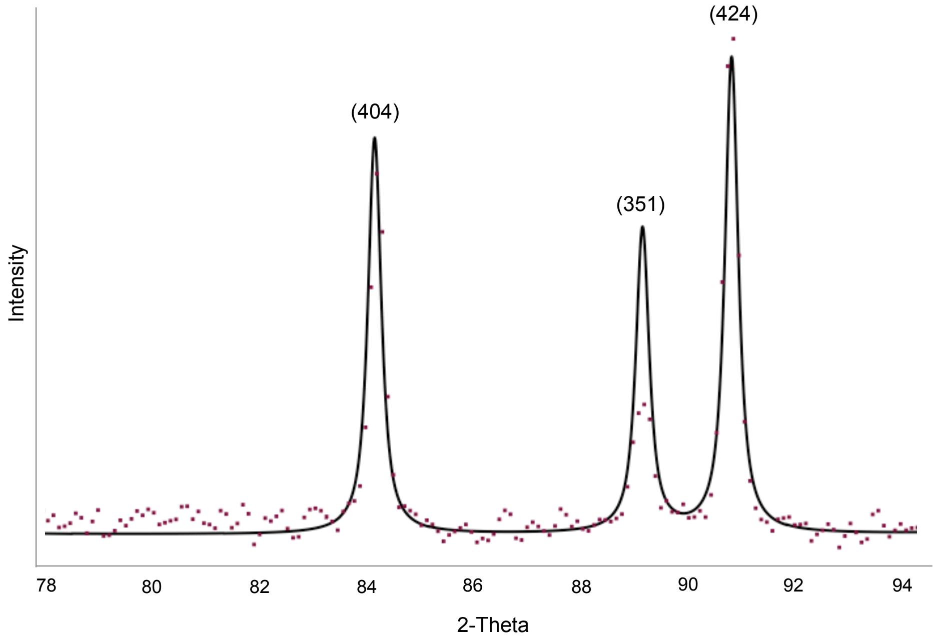

Figure 4-17: Simulated (solid line) and experimental (points) neutron diffraction pattern for sample TL11 ($Ni_{52}Mn_{26}Ga_{22}$). Indexing shown is referenced to the parent austenite unit cell.

The saturation field for a cubic sample of Ni–Mn–Ga with the field aligned with the easy-axis is about 2.5 kOe due to the shape anisotropy, $H_{\text{shape}}$, which is the value measured on the sample from TL11. If the sample was aligned with the applied field perpendicular to the $c$-axis, the resulting magnetization curve would result in a saturation field which is the sum of the shape and magnetocrystaline anisotropy, $H_{\text{shape}} + H_a$, which would be about 7.5 kOe. Therefore it is clear this measurement was performed with the applied field parallel to the $c$-axis and the sample is a single variant.

Figure 4-21 shows a Laue pattern taken after heating the sample into austenite and then allowing it to cool back to martensite without any applied stresses or magnetic field. The pattern is distinct from those seen in Figure 4-19 and 4-20. There are several areas showing double lines and double spots, which indicate a multi-variant state. It would be difficult to align this sample along the $c$-axis due to the presence of many twin variants with different orientations of the $c$-axis. From the Laue patterns

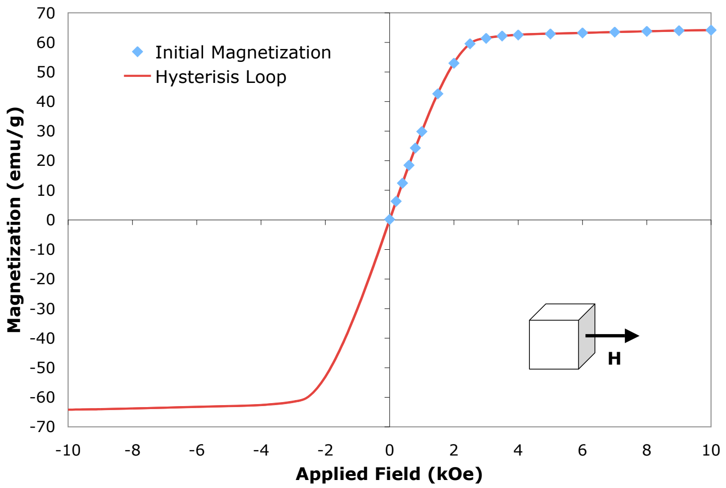

Figure 4-18: Magnetization versus applied field measured on cubic sample from TL11 used for single-crystal neutron diffraction. Both the initial magnetization and the full hysteresis loop are shown.

it was determined the the analysis of the multi-variant state would be too difficult and thus measurements in the single-crystal diffractometer were limited to the single variant martensite and the austenite phase.

Over four hundred spot intensities were measured in the martensite and austenite phases. In order to analyze this data, the powder diffraction analysis must be completed. The peaks from the single-crystal measurements can then be refined to better understand the state of chemical order present. It is also important to note that the magnetic scattering from the Mn magnetic moment will also have to be included in the analysis of the martensitic phase data. The refinement of the single-crystal data is beyond the scope of the thesis project but will be addressed in future work.

### 4.5.3 Discussion

The chemical ordering results presented here represent only the preliminary analysis of the neutron-diffraction data obtained from the ILL. It is clear that the site occupancies of alloys with close to 50 atomic percent nickel suggest that the excess Mn atoms occupy sites of the missing Ga atoms. This result is different from that for compositions which are further away from Ni = 50%. Simple assumptions about the location of the excess Ni and Mn does not agree with the measured diffracted intensities thus indicating a more complex site-occupancy scheme in the off-Ni-stoichiometric alloy compositions. The degree of order may impact the actuation behavior through the connection between composition and defects and thus will influence the performance of the material. A small degree of chemical disorder may introduce magnetic defects in addition to any structural defects. The interaction of these defects with domain walls and twin boundaries may alter the actuation behavior significantly.

Chemical order can also effect the mode of deformation that is active in these material, i.e. the transition from deformation by twinning to deformation by slip. In Al–Ti alloys, the high antiphase boundary (ABP) energy compared to the twinning/stacking-fault energy favors deformation by twinning in the chemically ordered state [91, 92]. A similar effect has been shown in Ni–Al alloys [93, 94]. Therefore, the state of chemical order can affect the number and mobility of twin boundaries, which in turn will impact the actuation performance of the material.

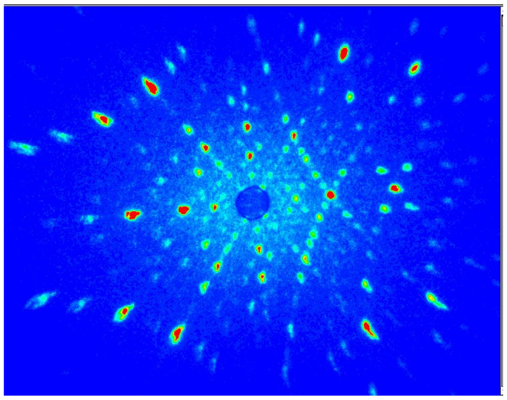

Figure 4-19: Neutron Laue pattern of single-crystal sample in a single variant state. Image taken with sample oriented off of the $c$-axis.

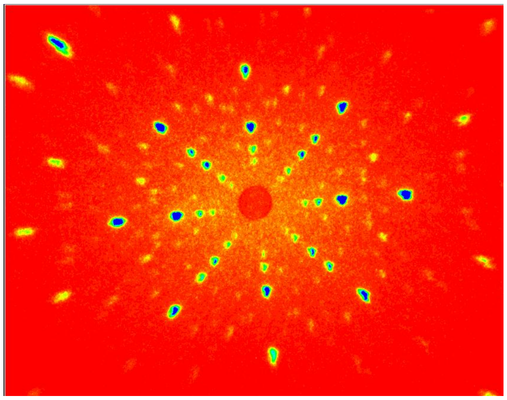

Figure 4-20: Neutron Laue pattern of single-crystal sample in a single variant state. Four-fold symmetry can be seen confirming the sample is aligned along the $c$-axis.

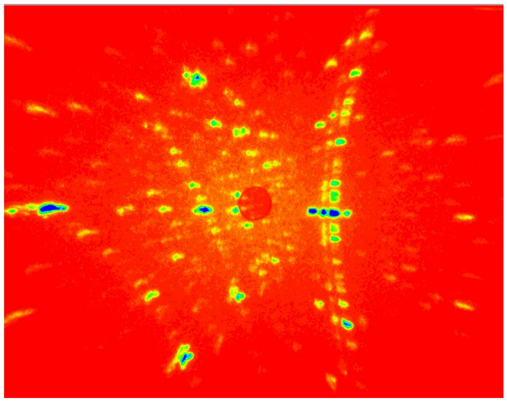

Figure 4-21: Neutron Laue pattern of single-crystal sample taken after one heating and cooling cycle from martensite to austenite. Multiple lines and spots are evidence of a multi-variant state.

# Chapter 5

# Transmission Electron Microscopy

## 5.1 Experimental Details

Samples for transmission electron microscopy were prepared from several single-crystal boules, each with a different composition and crystal structure shown in Table 5.1. 3 mm cylinders were cut from the large single crystals by electric discharge machining using a Charmiles Robofil 240 EDM. The sample size was chosen in order to match standard TEM sample holders. The orientation of the crystal was set before cutting to ensure that the cylinders would have $[100]_A$ normals to the end faces. The cylinders were heat treated in the same manner as the crystals described in Chapter 2.

Individual slices 200–300 microns in thickness were then cut from each cylinder using a fine-wire EDM. The sections were mechanically thinned using SiC grinding paper until a thickness of 50–90 microns was reached. The final thinning step was performed using a model 110 Fischione twin-jet electropolisher. The electrolyte was

Table 5.1: Average composition and crystal structure of samples examined with the TEM, in atomic percent. Sample TL10 was prepared with purified Mn, see Section 5.4.3.

| | Ni | Mn | Ga | Crystal Structure |
|---|---|---|---|---|
| TL5 | 48.6 | 31.0 | 20.4 | 14M |
| TL8 | 50.3 | 28.3 | 21.5 | 5M |
| TL10 | 50.2 | 29.0 | 20.8 | 5M |

a solution of 33% nitric acid and 67% methanol. The solution was cooled down to $-50^\circ$ and a voltage of approximetely 10–15 V was applied to the sample. The cooling was accomplished with a mixture of dry ice and methanol in a model 220 Fischione low-temperature container.

The initial TEM work was performed on a JEOL 200CX equipped with a tungsten filament operating at 200 kV. This microscope was useful for the early observations but was limited in source brightness, magnification, resolution and was not equipped with digital recording capabilities. Also, a tilt-rotate holder was needed because the magnetic nature of the sample prevented the conventional double-tilt holder from operating correctly. However, this microscope remained quite effective in qualifying samples before use in higher performance microscopes.

More recent microscopy work was performed using a JEOL 2011 microscope operated at 200 kV and equipped with a lanthanum hexaboride filament, which provided much brighter illumination as compared to the tungsten. A new model double-tilt holder was also used with this microscope which enabled much easier orientation adjustment. Images were recorded on photographic film as well as on an AMT digital imaging camera.

High-resolution electron microscopy (HRTEM) was performed on several samples at the John M. Cowley Center for High Resolution Electron Microscopy at Arizona State University with the assistance of Dr. Virgil Solomon and Prof. David Smith. A Philips CM200-FEG equipped with a field emission gun was used that enabled high resolution imaging, chemical characterization using EDS, and Lorentz microscopy for imaging of magnetic domains.

Highly localized chemical analysis was obtained using a VG HB603 scanning transmission electron microscope with the assistance of Dr. Anthony J. Garratt-Reed. The microscope was equipped with a field emission gun and operated at 250 kV. Chemical analysis was carried out using an EDS system.

All TEM micrographs and selected-area diffraction patterns displayed here have been corrected for any image rotation that may be present due to microscope mode changes

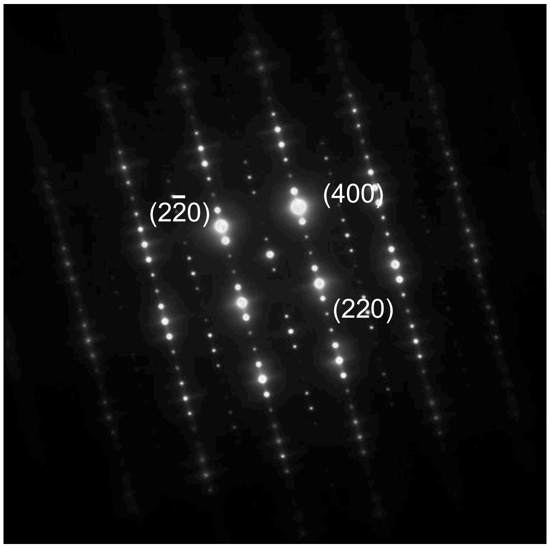

Figure 5-1: Selected-area diffraction pattern showing 5-layered structure with B=[001] taken from a sample from crystal TL8. Indexing is with respect to the parent cubic unit cell.

## 5.2 Superstructure — Imaging and Diffraction

As mentioned in Chapter 2, the periodic structures observed with x-ray diffraction were also seen using electron diffraction in the TEM. The majority of samples examined were from crystal TL8, which exhibits the tetragonal 5M structure. Figure 5-1 displays a representative selected-area electron diffraction pattern showing the 5M structure. The superstructure manifests itself as a set of four extra spots between the fundamental reflections. These extra spots break the region between the fundamentals into five equal sections. The diffraction pattern also confirms that the shuffling of planes is indeed along the [110] direction.

Figure 5-2 illustrates the type of bight-field contrast which was typically encountered in regions showing the 5M structure. The satellite peaks lead to the appearance of regularly spaced, alternating fringes which arise from the alternate stacking of planes in two directions. Also, it is possible to see areas in Figure 5-2 where the stacking sequence seems to be interrupted.

High-resolution imaging enabled the viewing of the stacking sequence directly.

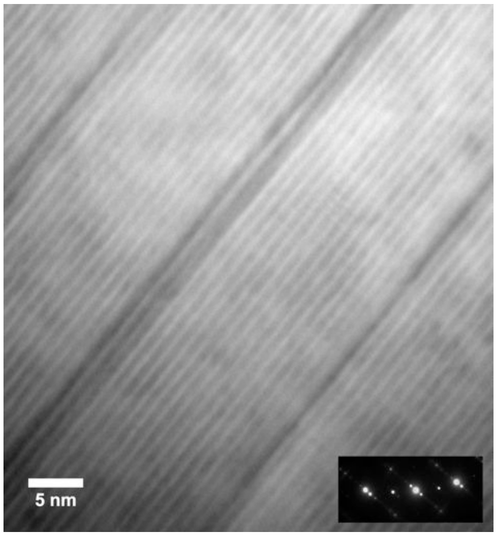

Figure 5-2: Bight field image of region from a sample taken from crystal TL8 showing evidence of the 5-layer superstructure with faults in the stacking sequence also visible. Inset shows selected-area diffraction pattern with g=[400].

Figure 5-3 shows a regions of perfect 5-layered stacking. The alternating dark and light layers arise from the $(3\overline{2})$ staking of (110)-type planes in the [110] direction. Close examination of the alternating layers reveals that they contain 3 atoms stacked in one direction and two in the opposite. The Fast Fourier transform (FFT) of this image reproduces a difractogram with a pattern similar to that shown in Figure 5-1, also indicating the 5-layer structure. In contrast to this image, Figure 5-4 shows another region from the same sample with an interrupted stacking sequence. This can be seen in the high-resolution image as the absence of same sharp contrast between alternating layers like the region shown in Figure 5-3. Also, the coresponding FFT does not contain sharp spots thus indicating that the periodic structure is not as regular in this region as it was in the previous.

Samples from crystal TL5, which was determined to have the orthorhombic 14M structure, were found to have regions that did indeed have the 7-layered stacking as seen in electron diffraction pattern shown Figure 5-5. The electron diffraction pattern shows six extra spots between fundamental spots, breaking up the area into 7 equal parts. The pattern is also compared with a simulated diffraction pattern shown in Figure 5-5b.

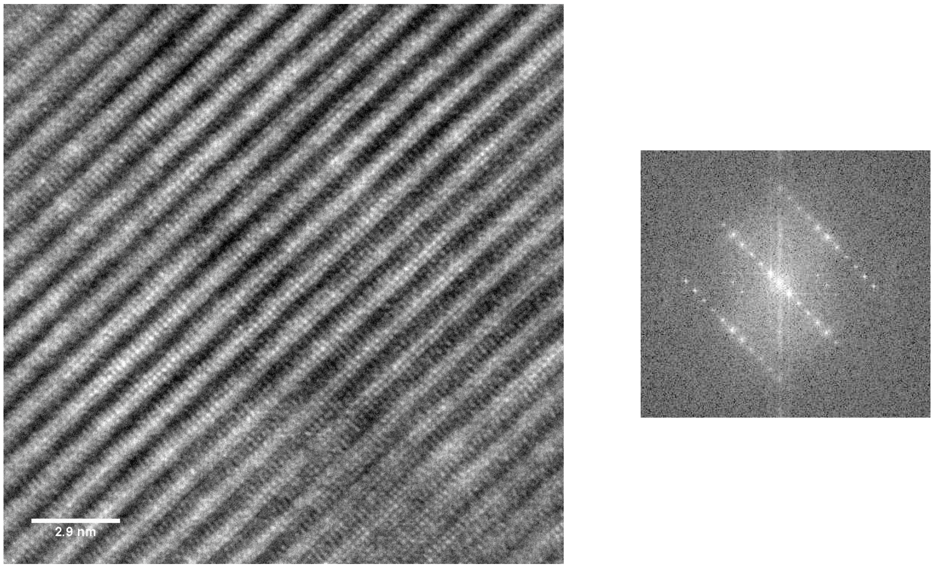

(a) (b)

Figure 5-3: (a) High-resolution transmission electron micrograph of region from a sample from crystal TL8 showing 5-layer stacking sequence $(3\overline{2})$ along with (b) FFT of the image.

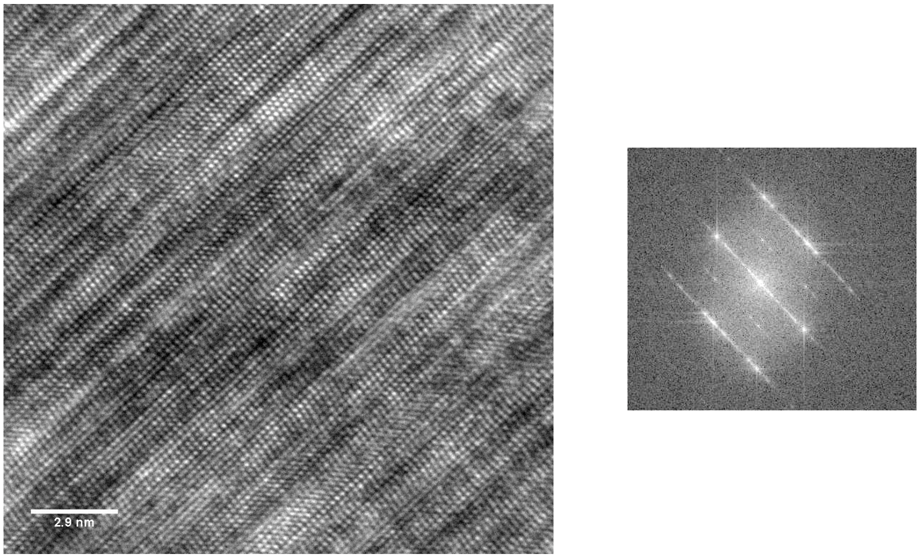

(a) (b)

Figure 5-4: (a) High-resolution transmission electron micrograph of region from a sample from crystal TL8 showing interrupted 5-layer stacking sequence along with (b) FFT of the image.

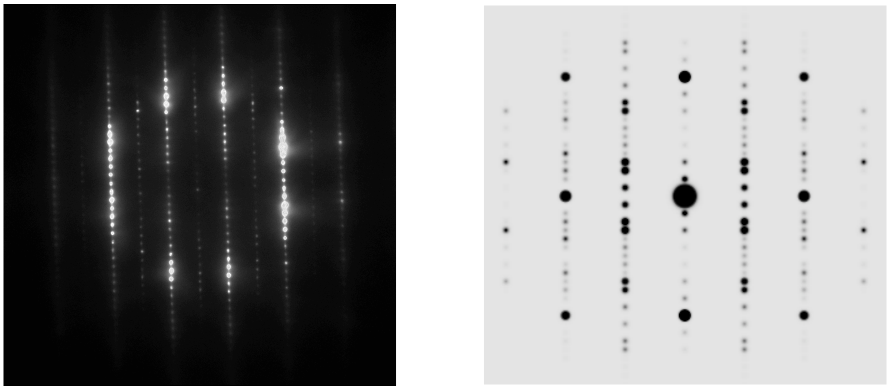

(a) (b)

Figure 5-5: (a) Experimental (sample from crystal TL5) and (b) simulated selected-area diffraction pattern showing seven-layer structure (14M) B=[100].

Some samples taken from both crystal TL8 and TL5 contained regions which had no evidence of the superstructure, as seen in Figure 5-6. The non-modulated structure can be due to the orientation of the particular sample with respect to the incident beam. If the modulation direction is parallel to the electron beam, no evidence of the stacking can be seen in the corresponding electron diffraction pattern. It is also possible that there are regions of the samples which were truly non-modulated as a result of inter-martensitic transformations. Several studies have demonstrated the existence of low temperature transformations from the 5M or 14M to the non-modulated structure [42, 76, 77, 78, 79]. Typically these transformations occur well below 0°C. The presence of low temperature transformation was shown to be composition dependent as well. The final twin-jet polishing of the samples was performed at around -50°C and thus there is a chance that some of the regions transformed into the low-temperature structure during sample preparation.

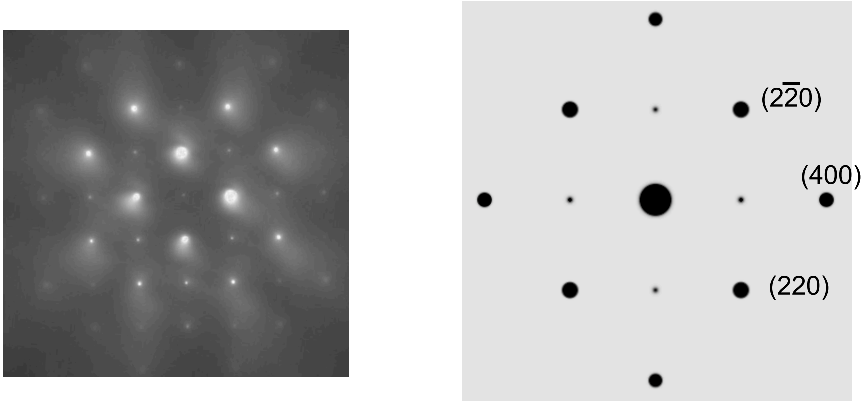

(a) (b)

Figure 5-6: (a) Experimental (sample from crystal TL5) and (b) simulated selected-area diffraction pattern showing non-modulated structure with B=[001]. Pattern has been indexed with respect to the parent cubic unit cell.

## 5.3 Twinning On Multiple Scales

The microscopy investigation revealed several different kinds of twinning that exist on different length scales. The smallest type of twins are on the nano-scale and often referred to as “nano-twins” [7]. These types of features, displayed in Figures 5-3 and 5-7, arise due to the presence of the periodic structure and were found in samples taken from all three crystals. For example, in the 5-layer structure, the $(3\bar{2})$ stacking sequence results in a mirror plane between the 3 and $\bar{2}$ layers. It is apparent from the selected-area diffraction pattern that the nanotwins exist on (220)-type planes. It is unlikely that these types of twins play a role in the magnetic field induced strain. In regions this small, the magnetization could not change direction between variants because it would create a very large number of high-energy domain walls. It would be difficult to form magnetic domains on such a small scale (5–10 Å). Estimates of the domain wall thickness based on the stringth of the uniaxial anisotropy are in the range of 100 Å [95].

On a slightly larger scale, twins of the type illustrated in Figure 5-8 are present in regions which do not show any evidence of a superstructure. As stated earlier, the

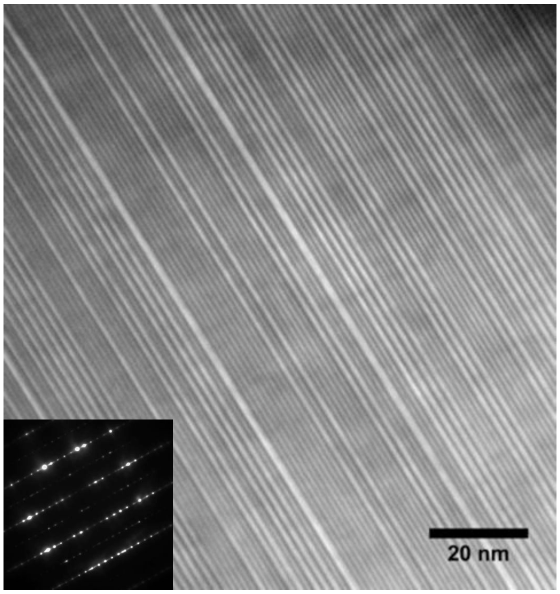

Figure 5-7: Bright-field image of twinning on the nano-scale arising from the modulated structure in a sample taken from TL8. Stacking is not perfect as can be seen from the regions of irregular spacing. Inset shows selected-area diffraction pattern with B=[001].

absence of the superstructure may be due to the presence of a different martensitic phase or the orientation of the periodicity with respect to the electron beam. These types of twins are between 5–100 nm in size with a large variation of thickness. The diffraction pattern inset in Figure 5-8 shows the characteristic spot pattern of a twinned region with the twin plane parallel to the electron the beam [96, 97]. The diffraction spots are related by a mirror symmetry indicated by the dotted line in Figure 5-9a. By indexing only the spots related to a single twin variant (red spots in Figure 5-9b), the twin planes are found to be of the (220)-type which is expected in Ni–Mn–Ga alloys. Again it is not clear if these types of twins are involved in the reorganization process that leads to field-induced strain.

On an even larger scale, there are types of boundaries which appear to be intersections of two martensitic variants with the modulation oriented in different directions. Figure 5-10 shows a boundary which is on a much larger scale than the two types discussed previously. The interface in this case appears to be irregularly shaped with many kinks and steps. The selected area diffraction pattern from each region reveals

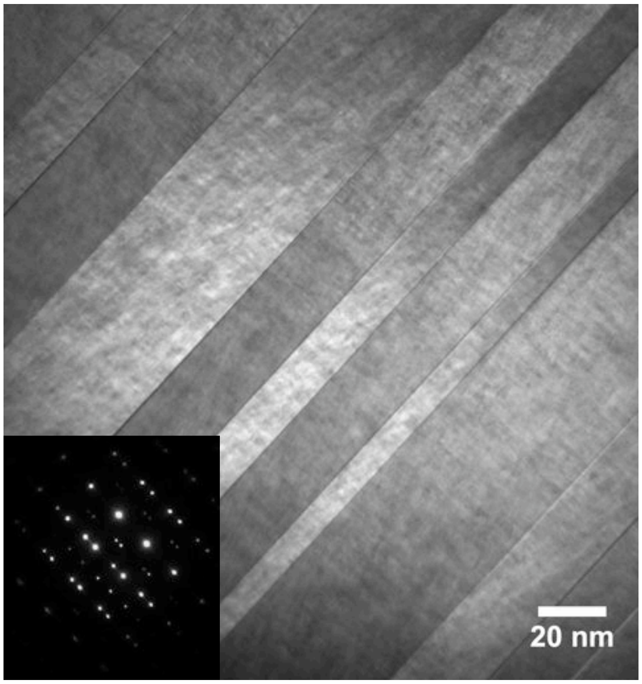

Figure 5-8: Bright-field image from a sample from crystal TL8 of (220)-twins with the beam parallel to the twinning plane. Inset shows characteristic diffraction pattern associated with this condition, B=[010].

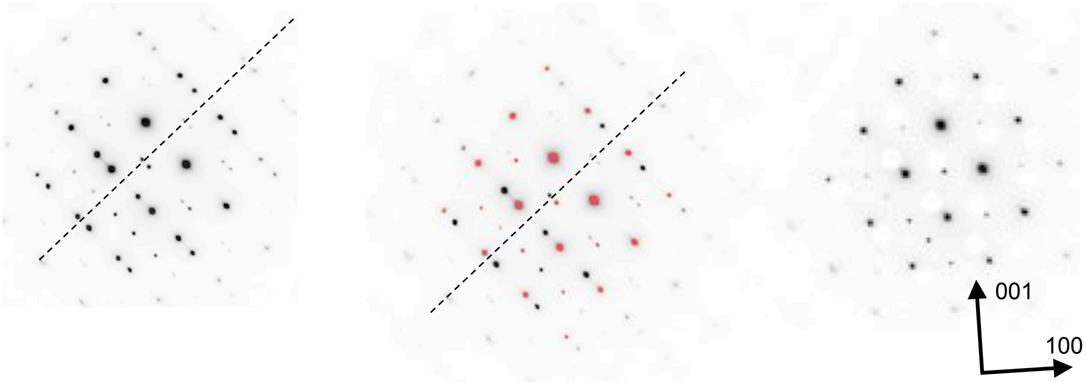

(a) (b) (c)

Figure 5-9: Analysis of the electron diffraction pattern from Figure 5-8. (a) The initial diffraction pattern with the dotted line indicating the mirror plane. (b) The emphasized spots belong to one of the two variants present. (c) With the spots related to the twin symmetry removed, the remaining spots show a [100] zone axis.

an orientation relationship between the two regions of about 90 degrees. This hierarchal twin structure contains nanotwins arising from the superstructure on each side of the larger boundary. The nanotwins appear to contain stacking faults which can be seen as irregular thickness of the fine-scale twinned bands.

It is also interesting to note that the boundary shown in Figure 5-10 is between a region of 5-layer and 7-layer periodicity as seen in selected area diffraction patterns taken from each side of the boundary. This type of boundary could be the result of a composition inhomogeneity, although the bulk composition of this sample lies completely within the tetragonal 5M region. More likely, the 7-layer phase region is a result of an intermartensitic transformation which has not occurred completely.

This type of boundary between 5-layer and 7-layer phases does not appear very often and it is more common to see such large-scale boundaries between two 5-layer regions with a 90 degree rotation, as shown in Figure 5-11. In this case, the nanotwinning on both sides of the boundaries appears very regular with no faults visible. The orientation relationship can be clearly seen in the selected-area diffraction pattern taken from a region spanning the boundary. The nanotwins of each region appear to overlap in the area around the boundary. This is likely a result of the boundary being inclined with respect to the electron beam.

The macroscopic twinning commonly seen on large, oriented single-crystal samples is presumably due to these large-scale variant boundaries. On the microscopic scale, the boundaries appear to be somewhat serrated as seen in Figure 5-10, however on the macroscopic scale it is likely they would appear smooth. Thus, field-induced twin boundary motion most likely involves these kinds of large-scale boundaries between nano-twinned regions.

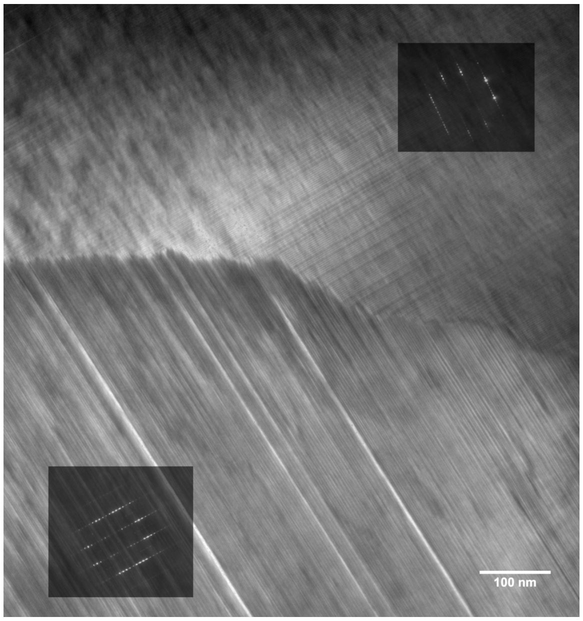

Figure 5-10: Larger-scale variant boundary showing a region of 5M stacking (upper area) and a region with 14M (lower area) taken from a sample from crystal TL8. Inset selected-area diffraction patterns indicate superstructure periodicity, B=[001].

## 5.4 Impurities — Inclusions and Precipitates

### 5.4.1 Sulfide Inclusions

Several large inclusions were observed in samples taken from two of the large single-crystal boules of TL8, which is tetragonal, and TL5, which is orthorhombic. Figure 5-12 shows a representative TEM micrograph of these inclusions. Inclusion sizes range from 200 nm to 1 $\mu$m in size and appear to be preferentially thinned during the twin-jet electropolishing used to prepare samples. From the features that remain, the inclusions seemed to have been present through the thickness as can be inferred from Figure 5-12. EDS analysis of the inclusions (Figure 5-13) reveals that they contain sulfur and are most likely sulfides. Comparison of EDS peak intensity ratios shown in Table 5.2 indicate that there is slightly more Ga in the inclusions than in the matrix suggesting the inclusions are gallium sulfides. It is difficult to draw a firm conclusion about the composition of the inclusions due to the preferential thinning and the small amount of material remaining in the thin-foil sample.

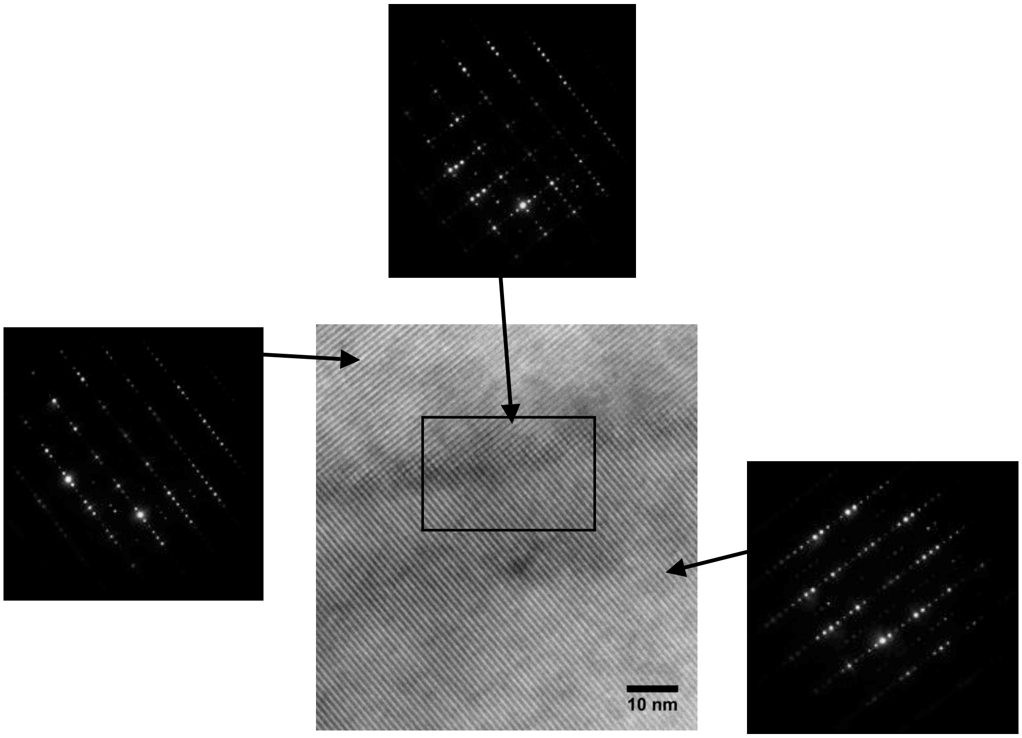

Figure 5-11: High-magnification bright-field image of martensitic variant intersection taken from a sample of crystal TL8. Selected-area diffraction patterns show 90 degree orientation relationship between the two variants.

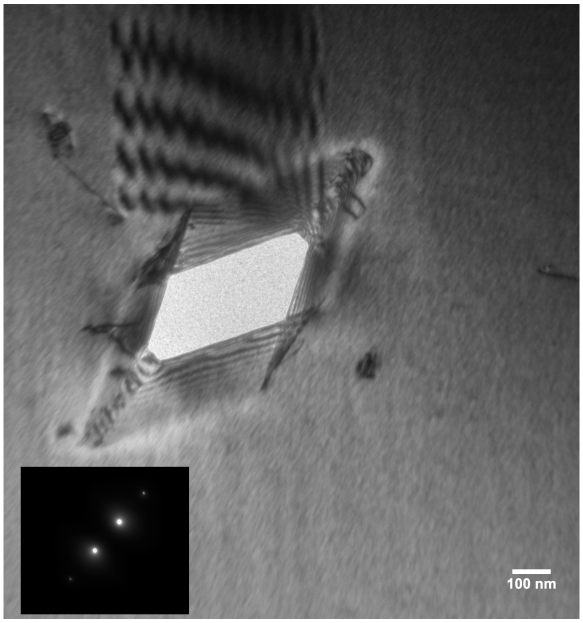

Figure 5-12: Bright-field micrograph of a large sulfide inclusion found in a sample from crystal TL5 (g = [220]). Inclusions of this type were found in both crystals TL5 and TL8.

Table 5.2: EDS peak intensity rations showing slightly higher Ga content of sulfide inclusions.

| | Mn/Ni | Ga/Ni | Ga/Mn |
|---|---|---|---|
| Matrix | 0.763 | 0.364 | 0.477 |
| Inclusion 1 | 0.771 | 0.424 | 0.549 |
| Inclusion 2 | 0.624 | 0.457 | 0.731 |

Samples taken from crystal TL5 showed a roughly ten times larger density of the sulfide inclusions as compared to TL8. It is interesting to note that all crystals cut from TL5 have not shown any field-induced strain where TL8 has yielded crystals which exhibit the maximum possible strain possible for tetragonal material, namely 6%. As discussed earlier in Chapter 2, others have shown 10% field-induced strain in orthorhombic crystals. The large number of sulfide inclusions may be the reason behind the lack of activity seen in crystal TL5. The sulfur contamination is believed to come from impurities present in the Mn used in alloy fabrication. There is no high-purity Mn available commercially so it is therefore necessary to purify the Mn to remove the sulfur (see Section 5.4.3).

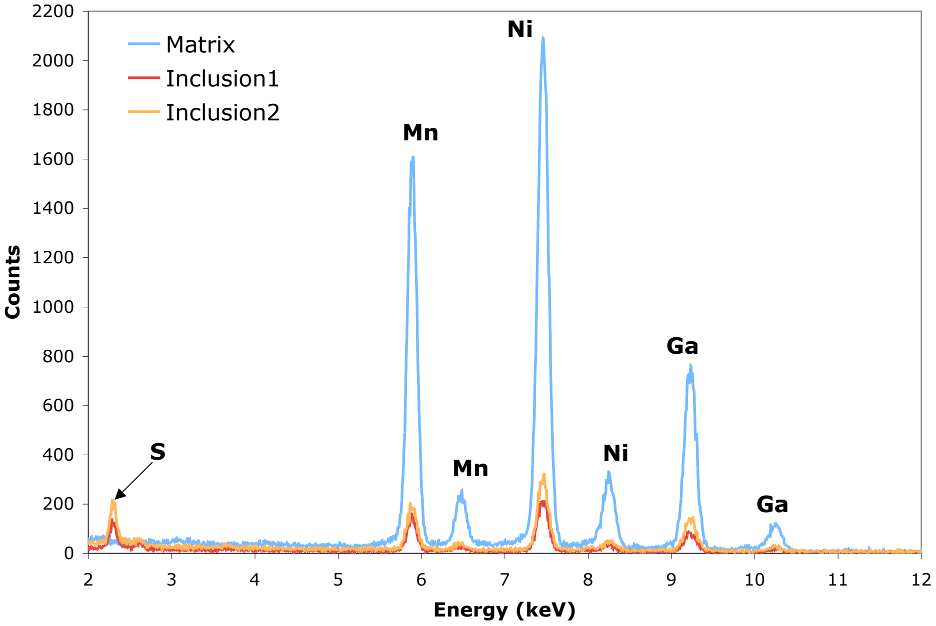

Figure 5-13: EDS spectrum obtained from large sulfide inclusions and matrix.

### 5.4.2 Ti-rich Precipitates

Upon examination of sample taken from crystal TL8, small, coherent precipitates were observed throughout the specimen. The particles were between 5–20 nm in size and typically appeared in large groups as seen in Figure 5-14. After observation of the small precipitates, a sample was annealed again at high temperature and then for a longer time (48 hours) at the lower annealing temperature (550°) in an effort to increase the precipitate size for better analysis. However, the precipitate size did not change significantly.

Figure 5-15 shows a group of precipitates from a section of TL8 that has undergone the additional annealing step. The precipitates were visible mainly due to the Ashby–Brown strain contrast arising due to the coherency strains [98, 99, 96]. The "coffee bean" shape is characteristic of this kind of contrast with the line of no contrast perpendicular to the operating $g$-vector. The dark-field image shown in Figure 5-15b was imaged using the (200) reflection and shows the precipitates as bright regions when using this reflection. The precipitates occasionally appeared aligned in rows as

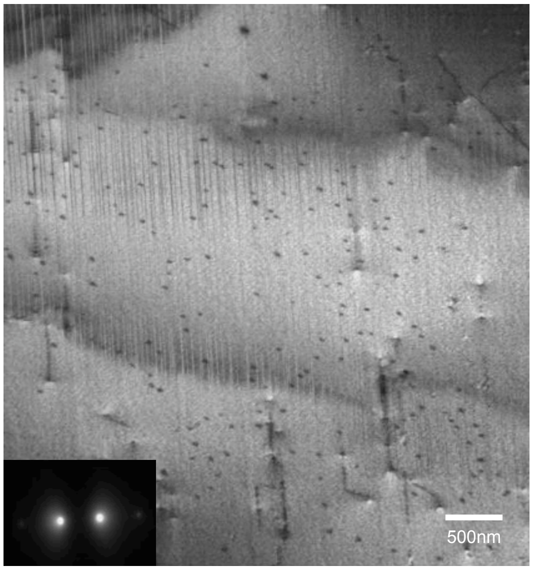

Figure 5-14: Low magnification image of region of TL8 containing a large number of precipitates. Inset shows selected-area diffraction pattern with g=[220].

seen in Figure 5-16.

Figure 5-17 displays higher magnification bright- and dark-field images of a single coherent precipitate under the same diffraction conditions as Figure 5-15. The Ashby–Brown contrast can be clearly seen along with the line of no contrast. Lattice fringes can also be observed in both images, although it is unclear if they are related to the precipitate. The precipitate is likely not present throughout the entire foil thickness and therefore there is matrix material material above and below. Again, when the (200) reflection is used for dark field imaging, the precipitate appears bright, indicating that the precipitate material is the source of this reflection.

The (200) reflection is a superlattice reflection as discussed in Chapter 4. Therefore, it was initially assumed that these precipitates were some type of ordered Ni–Mn–Ga precipitates formed during heat treatment. However, further STEM examination and composition measurements showed that the precipitates are actually a Ti-rich phase with small amounts of Mo and Nb as well. Figure 5-18 contains a STEM bright-field image of three of these precipitates along with two portions of the EDS spectrum obtained from the three precipitates and the surrounding matrix material.

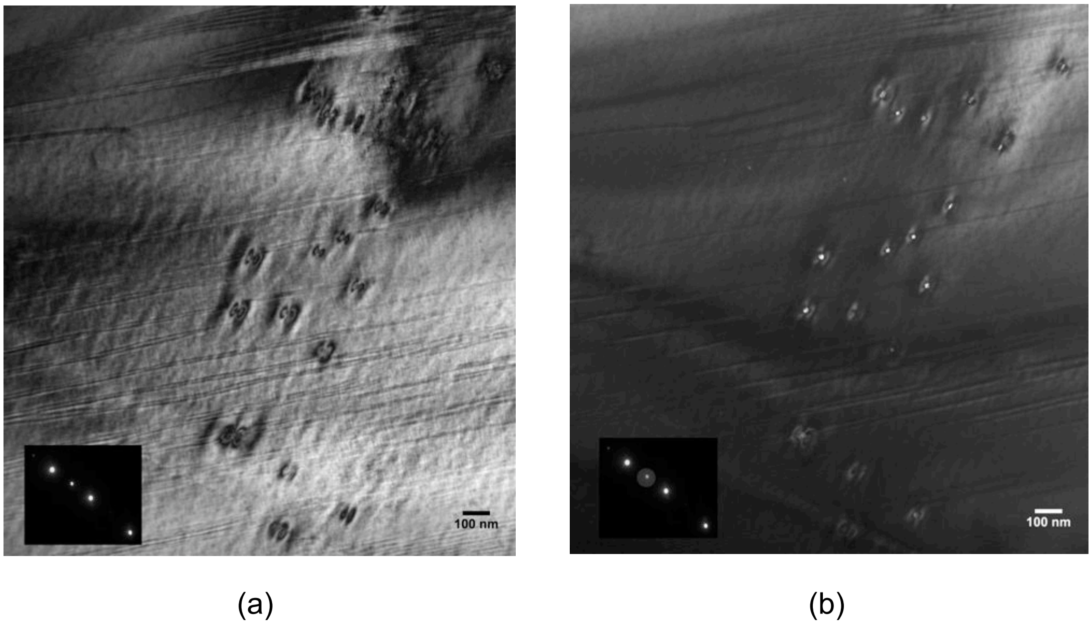

(a) (b)

Figure 5-15: Low magnification (a) bright-field and (b) dark-field micrograph of coherent precipitates found in sample TL8, g=[400].

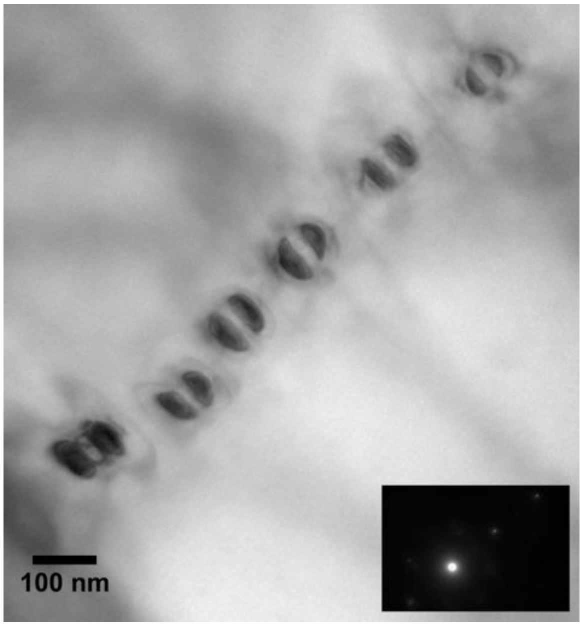

Figure 5-16: Bright-field micrograph of aligned coherent precipitates found in sample TL8 showing Ashby–Brown contrast.

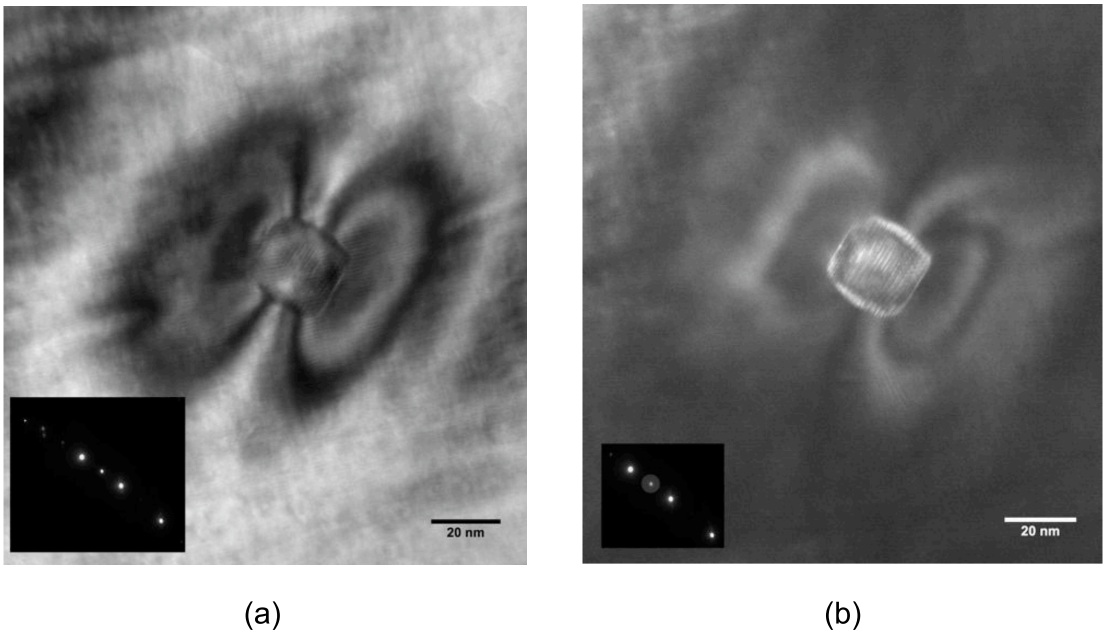

Figure 5-17: High magnification (a) bright-field and (b) dark field micrograph a coherent precipitate found in sample TL8, g=[400].

The spectrum clearly show the presence of Ti, Mo, and Nb in the precipitates but not in the matrix. It is difficult to determine the exact composition of the precipitates due to their small size. There is a large amount of matrix material above and below the precipitates, thus complicating the EDS quantization.

One possible identify for the precipitates is $Ni_3Ti$, which has a cubic phase exhibiting $L1_2$ order [100]. The lattice constant and structure of this phase would allow for the coherency observed as well as the coincidence of the (200) super-lattice reflection of Ni–Mn–Ga and the reflection originating from the precipitates thus explaining the contrast observed in the dark-field imaging. At this point, it is believed the Ti and other impurities originated from furnace contamination from a Nb–Ti alloy grown in the same furnace approximately 2 weeks earlier. It is quite surprising that such a small amount of Ti is not soluble in the matrix and forms coherent precipitates. No other crystals examined thus far have shown similar contamination or precipitate formation.

Large crystals cut from TL8 have shown field-induced twin boundary motion.

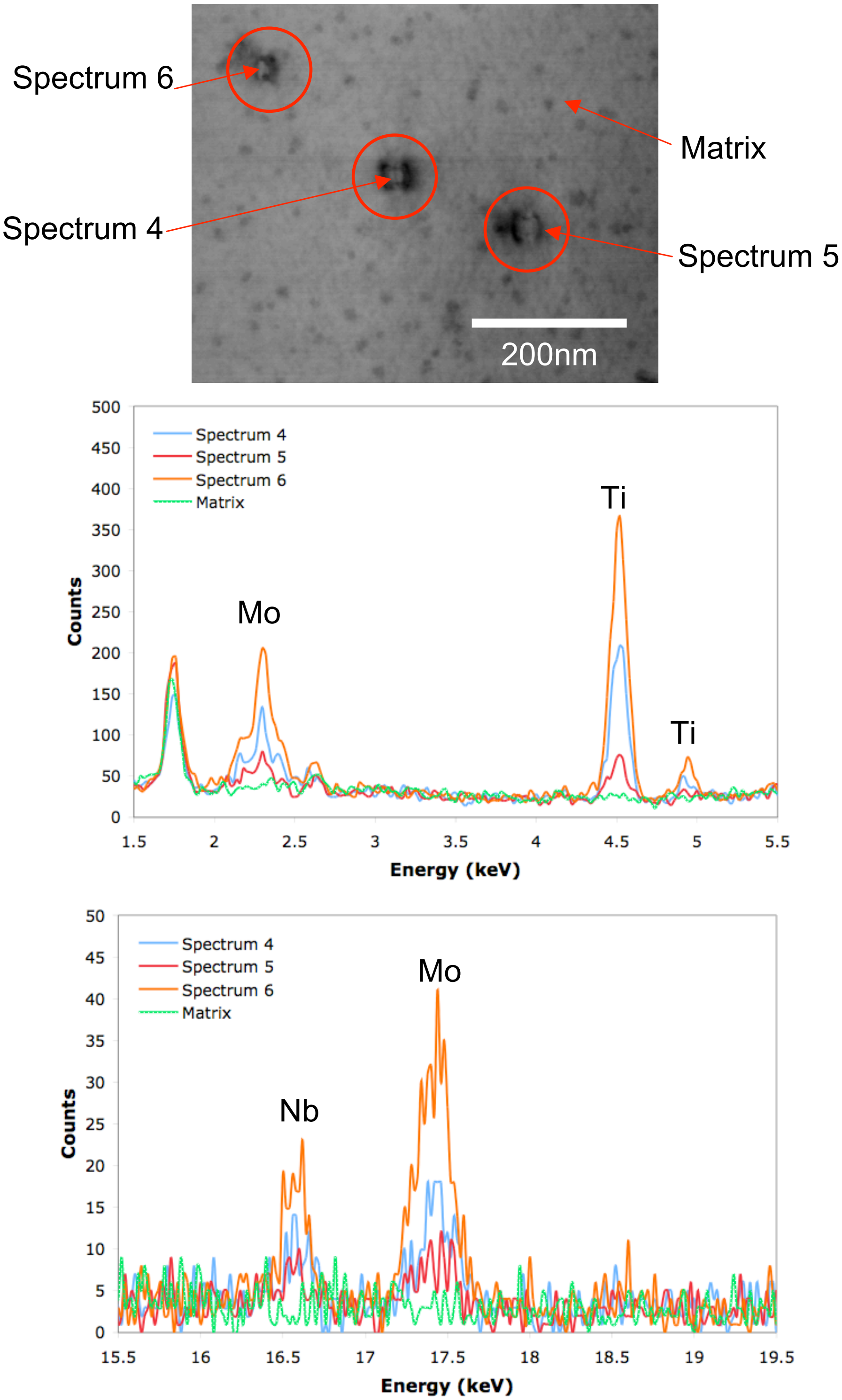

Figure 5-18: STEM bright-field image and EDS spectrum obtained from three coherent precipitates in sample TL8 and the surrounding matrix material.

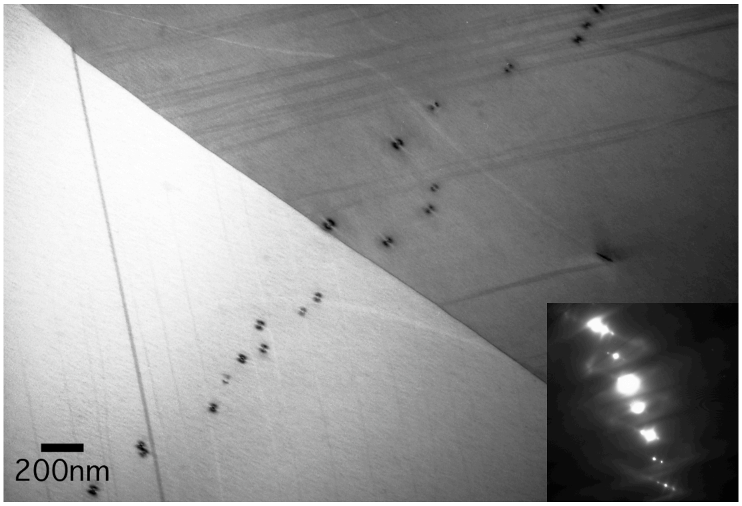

Figure 5-19: Bright-field image of Ti-rich precipitates located across a large-scale boundary in sample from crystal TL8, g=[400].

These crystals typically exhibit the 6% strain expected from the tetragonal martensitic phase. Because these precipitates are small and remain coherent with the matrix, it is possible they do not significantly inhibit twin boundary motion. Groups of these small precipitates are often located across twin boundaries as seen in Figure 5-19. Large, incoherent inclusions like the sulfides discussed previously would likely make twin boundary motion quite difficult, but these small precipitates do not seem to impact the material performance.

### 5.4.3 Inclusions in High Purity Samples

To avoid the formation of sulfides, it is possible to purify the manganese before preparing the alloys for crystal growth. The purification process takes advantage of the relatively high vapor pressure of Mn by using a sublimation process [101]. The manganese is heated in a vacuum for 48 hours and is allowed to condense on a cooled plate. Ni–Mn–Ga crystals grown from the purified material show drastic reductions in the amounts of oxygen, carbon, and most importantly sulfur.

The crystals produced with high-purity manganese showed many highly visible macroscopic twins. Some qualitative tests were performed in a magnetic field which

Table 5.3: Compositions (in atomic percent) measured with the STEM of the matrix and several inclusions found in the material produced with high-purity Mn (TL10).

| | Ni | Mn | Ga | Ta | Ti |
|---|---|---|---|---|---|
| Matrix | 49.30 | 29.70 | 20.84 | 0.14 | 0.02 |
| Inclusion 1 | 4.09 | 3.98 | 1.49 | 88.87 | 1.57 |
| Inclusion 2 | 3.78 | 3.76 | 2.12 | 88.66 | 1.69 |
| Inclusion 3 | 5.16 | 4.03 | 2.34 | 87.2 | 1.28 |
| Inclusion 4 | 5.14 | 4.43 | 2.45 | 86.59 | 1.38 |
| Inclusion 5 | 4.09 | 3.98 | 1.49 | 88.87 | 1.57 |
| Inclusion 6 | 3.78 | 3.76 | 2.12 | 88.66 | 1.69 |
| Inclusion 7 | 5.14 | 4.43 | 2.45 | 86.59 | 1.38 |

showed evidence for field-induced twin boundary motion. Several TEM samples were prepared from a crystal made with the high-purity material (TL10).

Upon examination in the TEM, the presence of large, plate-like inclusions was revealed. These inclusions were approximately 400–700 nm in size and each thin-foil sample contained anywhere from zero to ten. Figure 5-20 shows a representative micrograph of an inclusion of this type. The features appear to be present through the thickness of the foil.

Judging from the large number of dislocations and the extent of deformed material surrounding the inclusions, the second-phase regions appear to be incoherent with the matrix. The selected-area diffraction pattern taken from the inclusion shows that they are single crystalline. The particular inclusion shown in Figure 5-20 is oriented with beam along [111] while the matrix is oriented with the beam along [001]. Also of note is the absence in TL10 of sulfide inclusions like those discussed in Section 5.4.1.

STEM analysis of the inclusions revealed that they were mostly composed of tantalum with a small amount of titanium as well. A representative analysis of two inclusions is displayed in Figure 5-21. The EDS profiles taken from the matrix and inclusions show the presence of tantalum in the inclusions but not in the matrix. The compositions of several inclusions as well as the matrix is shown in Table 5.3.

One limitation of TEM analysis is the relatively small volume of material which can be observed. In order to better estimate the volume fraction of the tantalum

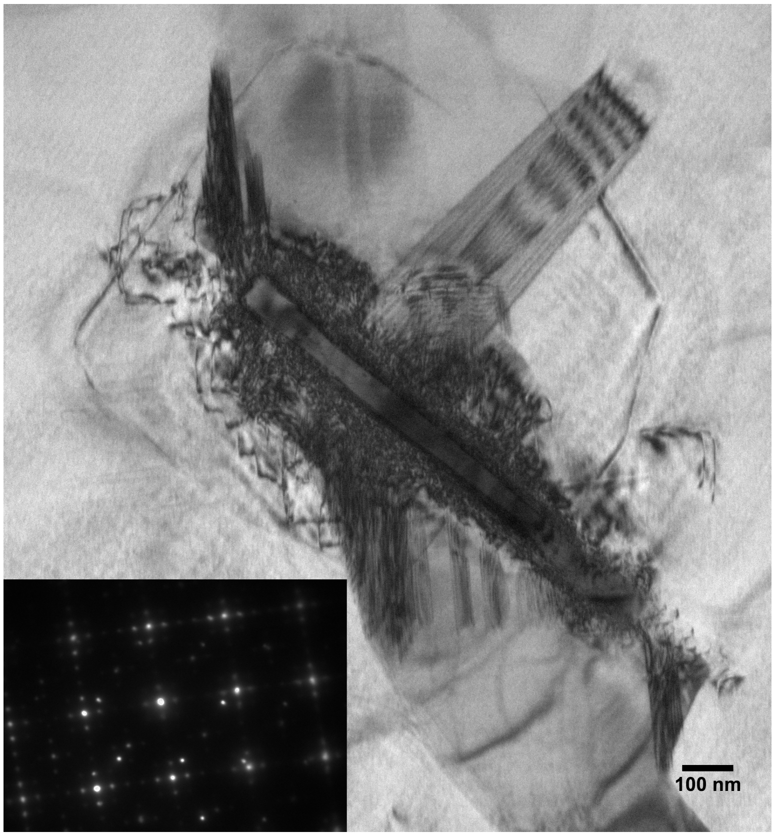

Figure 5-20: Inclusion found in a sample taken from a crystal grown with high-purity manganese (TL10). The inset electron diffraction pattern shows the matrix is oriented with B = [001] while the inclusions has B = [111].

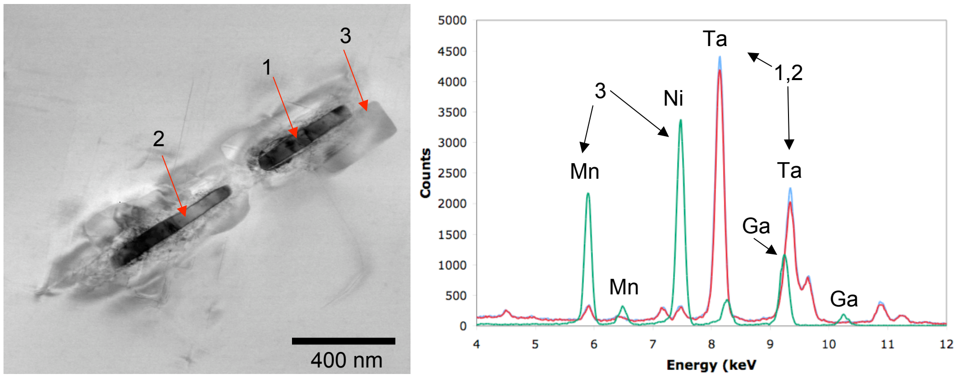

(a) (b)

Figure 5-21: (a) STEM micrograph and (b) EDS spectrums from two inclusions found in a crystal grown with high-purity manganese (TL10). The inclusions can be seen to contain mostly tantalum while the matrix contains only a trace amount of Ta.

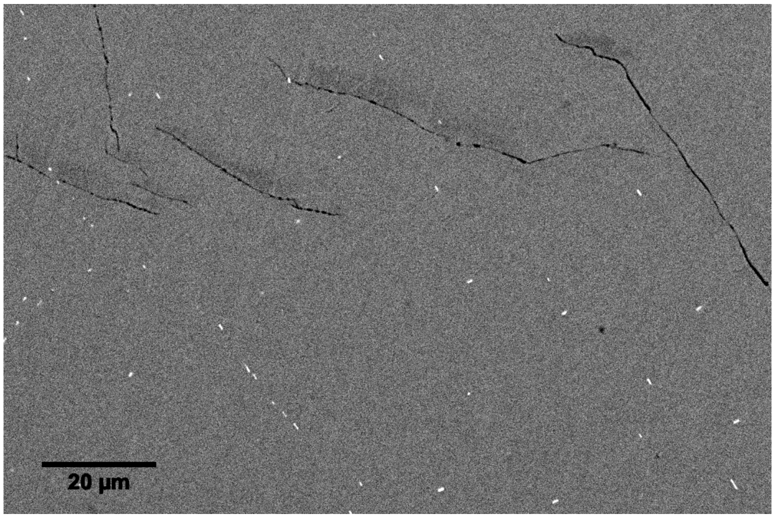

Figure 5-22: SEM micrograph imaged using backscattered electron showing bright tantalum inclusions. in a single-crystal piece of crystal TL10.

inclusions several sections were analyzed using an SEM in backscattered mode with EDS composition analysis capability. The inclusions were large enough in size to be viewed at a relatively low magnification. A SEM micrograph of a section taken from a high-purity crystal is shown in Figure 5-22. Many small, bright inclusions can be seen in this area. Tantalum has a significantly higher atomic number (Z = 73) compared to that of Ni, Mn and Ga (Z = 25, 28, 31) and thus appears much brighter when viewed within backscattered mode. Some inclusions appear to be grouped together and aligned. It is clear from this micrograph that there is a relatively small volume fraction of inclusions present in this crystal. Also, this micrograph reveals that there are large areas of material which are free of impurities and thus explains why some TEM foils did not contain any of these inclusions. It is interesting to note that much like the titanium-rich precipitates dicussed earlier there seems to be a large degree of insolubility of tantalum in the Ni–Mn–Ga matrix.

The source of the tantalum has been traced to the manganese purification process. During purification the Mn vapor is deposited on a tantalum plate and then broken off. It appears that when the manganese was removed some tantalum also broke off. Analysis of the material performed before crystal growth did not indicate a high level on tantalum [Lograsso] in the bulk material which can be attributed to the highly

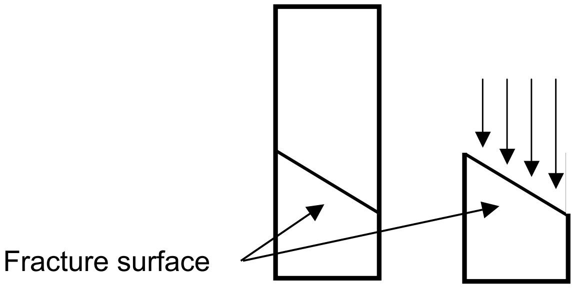

Figure 5-23: Schematic representation of the orientation of the fracture surface viewed in the SEM. Original sample faces had [100]-type normals.

localized nature of the inclusions. It is also possible that the piece analyzed by the crystal growers was not contaminated with Ta.

Several large crystals have been cut from high-purity boules TL10 and TL11. These crystals have shown field-induced strain of about 6% which is expected from the tetragonal structure. However, the crystals appear to be more susceptible to cracking and appear more brittle than other crystals cut from previous boules [102]. It is not clear yet if this behavior is due to the presence of the tantalum inclusions, but the presence of large amounts of plastic deformation around the inclusions could be a possible explanation of the observed brittle behavior. SEM observation of the fracture surface (Figure 5-23 of high-purity crystal has shown an increase in the presence of tantalum, as seen in Figures 5-24 and 5-25.

### 5.4.4 Discussion

A summary of the three types of impurities is shown in Table 5.4. It is evident that Ni–Mn–Ga alloys are extremely sensitive to impurities. Species that would be expected to have a larger degree of solubility in Ni, like Ti, appear to form second-phase particles when present in small amounts. It is therefore important to take great care in the production of Ni–Mn–Ga alloys and to characterize material sufficiently to determine the size and type of impurities that may be present.

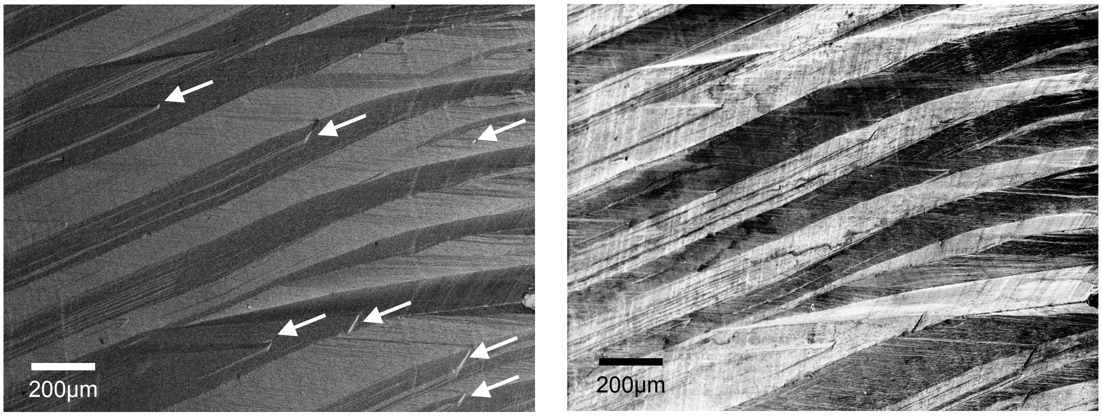

(a) (b)

Figure 5-24: (a) Backscattered (BSE) and (b) secondary (SE) electron image of the fracture surface of a high-purity crystal, TL11. Bright regions indicated with arrows in the BSE image are areas with many Ta inclusions.

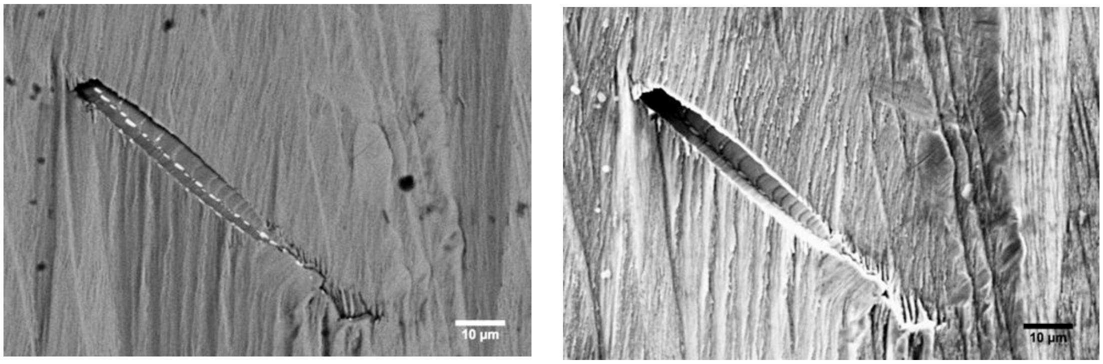

(a) (b)

Figure 5-25: (a) Backscattered (BSE) and (b) secondary (SE) electron image of a Ta-rich area on the fracture surface of a high-purity crystal, TL11. Bright regions in the BSE image are Ta inclusions.

Table 5.4: Summary of impurities present in the studied crystals.

| Impurity | Source | Size (nm) | Result of contamination |
|---|---|---|---|
| S | Mn starting material | 100–1000 | large, incoherent inclusions |
| Ti | Furnace contamination | 5–20 | small, coherent precipitates ($Ni_3Ti$) |
| Ta | Mn purification process | 400–700 | Plate-like single-crystal, incoherent surrounded by intense deformation |

From the size of the defects observed it is possible to calculate the approximate defect strength and compare the result with that of experimental observations of pinning defect strengths [47]. According to the work of Marioni, presented in Section 1.6.3, pinning site strength ranged from 0.5 $K_u$ to 0.7 $K_u$ with the most frequent site being of strength 0.56 $K_u \approx 1.06 \times 10^5$ J/m$^3$ [5]. Using the assumption that dislocations would have to loop around the inclusions in order for twin boundary motion to occur, the strength of the defect can be estimated using the Orowan approach [103, 104]. The pinning-site strength is analogous to the energy required to bend a dislocation line around obstacles. This assumption is valid for large particle sizes which would be applicable to the large S and Ta inclusions presented previously.

We can write the stress necessary for looping, analogous to a Frank-Read source, as:

$$\tau = \frac{Gb}{l} \tag{5.1}$$

where $G$ is the shear modulus, $b$ the Burgers vector, and $l$ the distance between pinning sites. The distance between two inclusions can be related to the volume fraction and radius of the second phase particles as:

$$l = \frac{r}{\sqrt{f}} \tag{5.2}$$

where $r$ is the inclusion radius and $f$ is the volume fraction of the second phase particles. By combining Equations 5.1 and 5.2, the strength of the defects can be written as a function of their radius and volume fraction:

Table 5.5: Calculated defect strength for large S and Ta inclusions assuming dislocation looping.

| Impurity | r (nm) | Approximate $f$ | Calculated Strength ($K_u$) |
|---|---|---|---|
| S in TL5 | 500 | 0.01 | 1.58 |
| S in TL8 | 500 | 0.001 | 0.50 |
| Ta in TL10 | 400 | 0.0001 | 0.63 |

$$\tau = \frac{Gb\sqrt{f}}{r} \tag{5.3}$$

Using approximate values for the necessary constants ($G = 50GPa$ [105] and $b = 3 \times 10^{-11}$ m) and the sizes and approximate volume fractions measured with the TEM, the energy required for looping can be calculated and is tabulated in Table 5.5. These values are first approximations and assume spherical inclusions. The calculated value for the sulfide inclusion in TL5 is an order of magnitude larger than that measured by Marioni. However the value for the sulfide inclusions in TL8 is on the same order as that measured due to the smaller volume fraction of the particles in TL8. Also, the Ta inclusions in TL10 are present in an even smaller fraction, and thus have a lower defect strength. Crystals from both TL10 and TL8 have shown field-induced twin-boundary motion, while crystals from TL5 have not. The inactivity of crystals cut from TL5 may be due to the presence of the large sulfide inclusions in a much higher volume fraction.

The Ti precipitates seen in TL8 are much smaller than the inclusions discussed above. Therefore, the mechanism of dislocation motion is most likely cutting through the particles as opposed to looping [103]. By cutting, the dislocations form two new interfaces, which have an associated surface energy. For small particles, like those seen in TL8, these new surfaces are small, allowing for a low-energy path for dislocation movement as compared to looping around the particles. For the case of cutting, we can write the stress needed for cutting (or the energy of the pinning site) as:

$$\tau = \frac{f\gamma}{b} \tag{5.4}$$

where $f$ is the volume fraction of the second phase, $\gamma$ is the surface energy, and $b$ is the burgers vector. Using the size measured in the TEM, an approximation for the volume faction ($1 \times 10^{-4}$) and surface energy (0.3 J/m$^2$), the defect strength can be calculated as approximately 0.53 K$_u$. This value is on the same order of magnitude as that calculated by Marioni. It would appear from these simple calculations, the the small Ti-rich precipitates may act as pinning sites which could be overcome by the application of a large enough magnetic field.

# Chapter 6

# Summary, Conclusions, and Future Work

## 6.1 Summary

The relationship between martensitic structure and composition was explored systematically with x-ray diffraction, TEM, neutron diffraction, and magnetic measurements over a large composition range. All of the compositions studied were in the martensitic phase at room temperature and exhibited a periodic superstructure. Several samples analyzed were in the tetragonal (5M) martensitic phase at room temperature and had previously exhibited magnetic field-induced strain of up to 6%. Compositions with higher Mn content were found to be orthorhombic martensite (14M), however, the orthorhombic single crystals cut from the single-crystal boule did not show any magnetic actuation. Other researchers have shown actuation in the orthorhombic phase yielding strains of up to 10%, but the 14M crystals available for this study were not active. A room-temeprature phase diagram was constructed which spanned the explored composition space.

To further characterize the powders studied by x-ray diffraction, the martensitic transformation temperature was measured magnetically on all the samples studied. These measurements revealed a marked difference between the transformation behavior of the tetragonal martensite and that of the orthorhombic phase. Samples with the tetragonal phase exhibited much sharper transition—that is, small differences between the martensite start and finish temperatures. Those samples in the orthorhombic phase had much broader transitions. This difference in transition behavior was confirmed with DSC and x-ray diffraction measurements.

Tabulation of the data from a number of samples having a range of compositions clearly showed that the change from sharper to broader transition behavior was abrupt at the tetragonal–orthorhombic boundary and did not change smoothly with composition. This leads to the conclusion that the difference in behavior is tied to the martensite structure and not chemical composition. Additionally, samples with different martensite structures that were cut from the same single-crystal boule exhibited the same differences in transformation behavior. The composition of individual samples was determined to be homogenous, further eliminating composition effects as an explanation of the observed behavior. Temperature-dependent x-ray diffraction measurements did not reveal any additional phases and confirmed that intermediate martensitic phases were not the cause of the broad transitions in the orthorhombic samples.

Building on the work of Patel and Cohen [11], a thermodynamic model was constructed for the transition from austenite to a multi-variant martensitic state in order to explain the difference in the observed transition behavior. The proposed framework adds an elastic-energy term to the free-energy expression of the martensite phase that is dependent on the fraction of material transformed. As more martensite is formed, the driving force is reduced thus requiring additional undercooling to continue the transformation. The elastic-energy effects are greater in the orthorhombic phase due to the larger transformation strain and the presence of a unique *b*-axis that leads to an additional set of twin variants that increase the probability of the formation of incompatible martensitic variants. This would in theory allow for more stress relief through twinning, however it would also lead to the intersection of variants with different orientations which would prevent further twin motion and cause the accumulation of elastic energy. Therefore, the larger strain-energy effects in the orthorhombic phase require the additional undercooling to maintain the necessary driving force and result in a broader martensitic transition.

X-ray diffraction provided a great deal of information about the martensitic structure but was shown to lack important information about the chemical ordering present in off-stoichiometry alloys. X-ray scattering factors of Ni, Mn, and Ga are too similar and thus the site occupancy information available x-ray measurements was crude. However, the limited data taken from x-ray measurements did exhibit a trend consistent with computed patterns of off-stoichiometric alloys when it was assumed that excess Mn atoms occupy Ga sites. This motivated the study of these alloys with neutron diffraction, which has the advantage of a large difference of the neutron scattering cross-sections of Ni, Mn, and Ga. Previous work with neutron diffraction was mainly limited to the austenite phase and did not address off-stoichiometric alloy compositions, especially those with nickel content greater or less than 50 atomic percent.

The preliminary analysis of the neutron data obtained from the ILL in July 2005 was consistent with the structure observed with x-ray diffraction. The additional peaks which appeared in the simulated neutron diffraction patterns did indeed appear in the neutron results. Initial modeling of the site occupations in the austenite phase was attempted with simple peak profile functions and calculated patterns using the CrystalDiffract © software. The patterns from the two samples which contained close to 50 atomic percent nickel were fit well assuming that the excess manganese occupied gallium sites, which were available due to the gallium deficiency. However, similar assumptions for the alloy containing more than 50% nickel did not lead to the pattern being fit well and the peak intensities did not agree with the simulations.

Single-crystal neutron measurements were also performed at the ILL on a single sample due to the increased time required for measurement. The crystals were prepared to ensure a single-variant martensitic state, which was confirmed by both magnetic measurements and neutron Laue diffraction. Over 400 diffraction peaks were collected in the single-variant martensitic state and the austenitic phase. Upon cooling from austenite, the samples were unconstrained and transformed into a multi-variant martensite, which was confirmed by Laue measurements. The data was not collected from the multi-variant sample due to the high complexity of the resulting structure and corresponding diffraction pattern.

Transmission electron microscopy was performed on samples taken from several different single-crystal boules having different alloy composition. Electron diffraction patterns confirmed the presence of a superstructure and were consistent with the 5M and 14M structure. High-resolution microscopy of samples taken from TL8 (5M structure) allowed for the imaging of the $(3\bar{2})$ stacking of (110)-type planes in the martensite, matching results reported by others. Some samples showed regions of non-modulated martensite, which was either a result of sample orientation relative to the electron beam or an intermartensitic transformation that took place during sample preparation.

The twinning observed with the TEM occurred on several different scales. On the finest scale, some samples displayed nanotwins which were a result of the 5M structure. These features were seen in images taken with both the conventional TEM and with a high-resolution microscope. Some samples displayed regions with perfect periodic stacking while other regions had faults which interrupted the stacking sequence. The 14M structure was also seen to exhibit the twinning on the nano-scale which resulted from the 7-layer superstructure.

On a larger scale, boundaries between nanotwinned regions were observed, forming the variant structure that is observed on the macroscale. Bright-field images of such boundaries showed the nanotwinned nature of each variant with the long-range interface spanning microns between them. The electron diffraction patterns demonstrated a nearly 90 degree orientation relationship between the adjoining regions. These boundaries appeared to have relatively smooth regions as well as areas that contained kinks and steps. It is believed that these are the types of boundaries visible as straight lines on the macroscopic scale and only appear serrated upon microscopic observation.

Regions which did not display any evidence of the superstructure occasionally contained twins 20–100 nm in thickness. When properly oriented, these twinned regions yielded electron diffraction patterns which were consistent with the twin planes being parallel to the electron beam and thus allowed the twin planes to be indexed as (220)-type planes.

TEM observation also revealed the presence of contamination from impurities in several of the single-crystal boules. Large sulfide inclusions of 200 nm to 1 micron in size were found in samples taken from crystals TL5 (14M) and TL8 (5M), with the inclusions being much more prevalent in samples from TL5. These large inclusions appeared to be preferentially thinned during sample preparation thus leaving a small amount of material for composition analysis. EDS measurements on the remaining material indicated that the inclusions may be gallium sulfides, but exact composition determination was not possible. Crystal TL8 has yielded several single-crystal specimens that have exhibited the 6% field-induced strain, which is the maximum possible for the tetragonal phase. On the other hand, samples cut from TL5, which has the 14M orthorhombic structure, contained more of the sulfides and did not show any field-induced actuation. The source of the sulfur was determined to be manganese which is not available commercially in a purified form.

Samples from TL8 contained an additional type of impurity contamination in the form of small, coherent particles of about 5 to 20 nm in size. Due to their size and coherency it was assumed that these particles were some type of ordered precipitate that formed during heat treatment. These small precipitates showed the typical Ashby-Brown contrast that is expected from small, coherent particles present in a matrix. Additional heat treatment with an extended lower-temperature anneal did not significantly increase the precipitate size. STEM microanalysis of the particles showed them to be a Ti-rich phase containing small amounts of Mo and Nb. The source of the contamination is believed to be furnace contamination from a Nb-Ti alloy previously grown in the same furnace as TL8. As previously mentioned, crystals cut from TL8 have shown field-induced strain indicating that these small precipitates do not significantly impede twin-boundary motion. No other crystals have contained similar precipitates.

Samples from crystal TL10, grown with purified manganese, were analyzed to determine if the purification process successfully removed sulfur resulting in sulfide-free single crystals. No sulfides were present in samples taken from crystal TL10. However, large, plate-like inclusions were found in these samples which were surrounded by a zone containing a large number dislocations indicative of plastic deformation arising from particle-misfit strains. The second-phase particles were determined to be single crystalline. STEM analysis revealed the inclusions to be Ta-rich precipitates with a small amount of Ti. SEM analysis confirmed the presence of these inclusions in TL10 and TL11, which were both produced using purified Mn. The Ta was believed to originate from the Ta plate on which manganese was deposited during the purification process. When the purified material was detached from the tantalum plate, small pieces of Ta must have broken off as well.

Single-crystal samples cut from TL11 for actuation experiments have been found to be more brittle than samples cut from previous crystals [102]. After several cycles of actuation, these crystals fractured easily along planes which were found to contain a large number of Ta particles. Acting as large centers of stress concentration, the Ta inclusions would be sites were cracks could form preferentially. Also, the interaction of twin boundaries with the particles and strained matrix could lead to mechanical instabilities and fracture.

## 6.2 Conclusions

The composition-structure diagram constructed using the results of the x-ray diffraction experiments will be useful in the development of alloys for specific applications. Selection of alloys with the desired structure, output stress and strain characteristics, and transformation temperature will be important in the practical use of Ni–Mn–Ga-based actuators and other devices. Also, the electrons per atom (e/a) parameter was shown to be unable to predict the martensitic structure in the composition range studied. The e/a parameter is useful in the ternary system since it can describe the composition with a single parameter and has been useful in determining the relationship between the various transformation temperatures (martensitic and Curie) and composition. However, it falls short in providing predictive power for the martensitic phase present at room temperature. In order to map the composition dependence of the martensitic structure, two of the composition parameters must be used in a manner similar to the diagram presented in Chapter 2 (Figure 2-17).

Also, the transformation behavior observed in the tetragonal and orthorhombic structure will be important to understand when designing devices for specific operating temperature ranges. It is apparent that a sharp austenite to martensite transition cannot be expected in all cases, thus requiring closer examination of operating conditions and alloy selection. This work highlights the shortcomings of characterizing the martensitic transformation with a single transformation temperature. Additional parameters are necessary in order to clearly define the width of the transformation. This information is essential when using Ni–Mn–Ga in application environments. The presence of any austenite will certainly reduce the output strain by lowering the volume fraction of active material.

The chemical ordering results presented clearly indicate that the site occupancies of alloys further away from Ni = 50% compositions are not explained by simple assumptions for the location of the excess species (Ni or Mn). The calculated patterns do not match the neutron powder diffraction experiments when the excess Ni and Mn are assumed to occupy Ga sites . This preliminary work will help to further understand the state of chemical ordering in off-stoichiometric Ni–Mn–Ga alloys. A small amount of chemical disorder may impact the actuation behavior through the creation of magnetic and structural defects that can influence the motion of twin boundaries and domain walls. Also, the degree of chemical order can effect the mode of deformation, with more disorder allowing slip to become active as opposed to twinning.

As mentioned previously, there have been no published studies of the chemical ordering of off-stoichiometry alloys. Thus the work presented here is a first step in understanding the role of chemical ordering in Ni–Mn–Ga alloys. Further studies of the mechanical and actuation properties of crystals with different states of chemical order would aide in the understanding of the connection between chemical ordering and twin-boundary motion.

Finally, the microscopy confirmed the presence of the periodic superstructure in both the orthorhombic and tetragonal material. It also revealed the presence of stacking faults in the periodic structure. It is unclear at this point if these faults impact the output-strain performance, but defects of this type may not aid in the field-induced reorganization of twin variants. On a larger scale, the variant boundaries observed appeared to contain kinks and steps, features that are quite different than the smooth lines observed on the macroscopic scale.

The impurities discovered in several of the single-crystal boules indicates the sensitivity of this alloy system to the presence of other components. The sulfide inclusions which are a result of Mn impurities seem to have a negative effect on actuation performance. Crystals from TL5 which have a far greater number of sulfide inclusions does not show any actuation response, while those from TL8 which has few sulfides generally exhibits field-induced strain up to the theoretical maximum.

The formation of precipitates of both Ta and Ti-rich phases is surprising since both Ti and Ta exhibit significant solubility in nickel. The absence of sulfides in the high-purity (sulfur-free) material was confirmed and should result in material with better performance. However, the large Ta-inclusions have been demonstrated to cause the material to become embrittled and fracture after a small number of cycles. This is in contrast to the small, Ti-rich precipitates which appear to remain coherent with the matrix and do not seem to impact actuation behavior greatly.

The approximations of the pinning site strength for the different second-phase particles can help explain the different actuation performance observed. The sulfide inclusions in TL5 have the highest defect strength and exceed the magnetocrystalline anisotropy energy. Therefore, twin boundaries pinned at these types of sites cannot be freed with an applied field. This reasoning reveals why crystals cut from TL5 have never shown any field-induced strain. In contrast, the same sulfide inclusions present in TL8 in a smaller volume fraction do not act as such strong pinning sites. The field is capable of overcoming these defects in TL8 and crystals from this boule have shown the maximum field-induced strain. Likewise, the Ti and Ta particles observed act as pinning sites but can be overcome with an applied field because the defect strength is less than the applied field.

The results presented here will be useful in future alloy development and understanding of the magnetic field-inudced strain phenomena in Ni–Mn–Ga alloys. With the data collected, it is now possible to predict the martensitic structure over a range of compositions that have shown promise for magnetic field-induced actuation. The microscopy has revealed a hieracrchial twin structure confirming the orientation of the twin planes. Also, several second-phase particles have been identified that impact twin boundary motion and thus indicate the need for high-purity components for single-crystal growth in this alloy system.

Through a better understanding of the transition behavior and the defect structure, it will be possible to create material with superior actuation properties that will allow for the design of devices and the use of this material in real-world applications. Beyond the engineering relevance of the martensitic structure, martensitic transformation, and chemical ordering explored here, the results have expanded on the fundamental understanding of the structure-property relationship in Ni–Mn–Ga alloys. The range of alloy compositions explored provide new data that will complement the other compositions explored in previous work and will be useful to other researchers in the field.

## 6.3 Proposed Future Work

### 6.3.1 Additional Observations of the Martensitic Transition

In order to better understand the difference in the transition behavior seen in the orthorhombic and tetragonal phases it would be useful to observe the transition with in-situ electron microscopy. These observations of the sample while heating and cooling through the transition would yield important information about the formation of multiple variants and the interaction between different martensite variants. Defects which may be created as a result of the transformation could also be observed. Possible limitations of this type of experiment would include the small volume which can be analyzed in the TEM as well as any artifacts arising from the essentially two-dimensional thin foil. Combining several sample observation with SEM analysis may overcome this drawback by increasing the amount of material analyzed and offering a comparison to the thin-sample results.

Observations of a single-interface transformation would also help to understand the transition process. If a single-variant martensitic phase can be nucleated through controlled cooling, the proposed effects of variant interactions would be eliminated. The kinetics of the transition under these conditions would better the understanding of the transition in the more typical multi-variant case. Also, measurements of the transition under external stressed would aide in extending the thermodynamic framework presented here.

### 6.3.2 Neutron Diffraction

Measurement of sample TL6 in the austenite phase will be an important addition to the other preliminary neutron-diffraction experiments. A nickel-poor composition such as TL6 will compliment the current data set which includes two samples near 50 nickel and one which is nickel rich. It is already clear that the site selection in the nickel-rich alloy is more complex than the simple model used in the initial fits. Having data from a nickel-poor alloy will help to further clarify the site occupancies and the degree of chemical order in the off-stoichiometry alloys.

Analysis of the single-crystal results is the next step once the powder patterns are well understood. The data from the austenite will help in understanding the structure in the absence of the complex superstructure and data taken above the Curie temperature could eliminate the magnetic scattering of the Mn. However, the room-temperature martensitic structure analysis will be extremely beneficial in the understanding of the chemical ordering. As was mentioned earlier, full analysis of the multivariant state would be quite difficult. However, data collected from several peaks of different types (II, III, and IV) spanning the transition would aid in understanding the relationship between the variant structure and the state of chemical order.

### 6.3.3 Improvement in Mn Purification Process

It is clear from the present work that the introduction of Ta from the Mn purification process yields crystals of suboptimal performance. An effort to change the material used for the condensation of Mn would help in creating material that is free of both sulfur and tantalum impurities. Working with the crystal growers, a new material and process for Mn purification should be developed. Changing from a Ta plate to a water cooled Ni and Mn substrate would help eliminate the chance of contamination. Also, the combined analysis of bulk specimens as well as investigation at the microscopic level will be instrumental in finding trace impurities in the produced alloys.

### 6.3.4 Additional Transmission Electron Microscopy

Further analysis of the defects present in material that has undergone many magnetic field-induced actuation cycles would help in understanding the fatigue properties of Ni–Mn–Ga alloys. Cylinders of homogenous composition could be cut as was done for this work and heat treated in a manner similar to single crystals used for actuation experiments. Before transforming to martensite, the cylinder would be placed under a static load in order to ensure a single-variant state. The sample could then be cut in half, with one piece serving as the control as the other half undergoes several actuation cycles under an applied magnetic field. This could be accomplished by placing the cylindrical sample in an actuation test frame used to study cyclic actuation. Another possible approach would be to attempt to nucleate a single twin boundary with a permanent magnet, and then move the boundary by hand through the sample many times. Then each sample, the control and actuated material, could be sectioned and analyzed in the TEM. Specific defects may arise due to the twin boundary motion that will be absent in the control sample. Defects that are generated by the twin boundaries could be identified as well as any defects that are present which pin boundaries.

Samples for TEM of different orientations would also be useful in understanding the relationship between twin boundaries and defects. The samples used in the work presented were limited to material cut from the single-crystal boules with [100] type normals to the sample surface. Other orientations could possibly reveal other defect structures that were not visible with the current samples. Orientation of the samples relative to the electron beams is crucial in illuminating certain defects through diffraction contrast. The current TEM sample holder allows for limited tilting in two directions. By having samples with different orientations, this limitation could be overcome.

Further STEM analysis would also provide insight into any composition inhomogeneities that might exist around defects or boundaries. With the small probe sizes available on the STEM, the composition across the boundaries could be determined and preferential distribution of the components near the boundaries would be revealed. Twin boundaries would create a zone of inhomogeneous strain and may cause excess Mn or Ni to accumulate at the boundary. If this type of atmosphere exists, it would most likely cause difficulty in twin boundary motion due to the added effect of the segregated species.

# Bibliography

[1] K. Otsuka and C. M. Wayman, editors. *Shape Memory Materials*. Cambridge University Press, 1998.

[2] A. Zheludev, S. M. Shapiro, P. Wochner, and L. E. Tanner. Precursor effects and premartensitic transformation in $Ni_2MnGa$. *Phys Rev B*, 54(21):15045, 1996.

[3] S. J. Murray, M. A. Marioni, S. M. Allen, R. C. O'Handley, and T. A. Lograsso. 6% magnetic-field-induced strain by twin-boundary motion in ferromagnetic Ni–Mn–Ga. *Appl. Phys. Lett.*, 77:886–888, 2000.

[4] C. P. Henry, D. Bono, J. Feuchtwanger, S. M. Allen, and R. C. O'Handley. AC field-induced actuation of single crystal Ni–Mn–Ga. *J Appl Phys*, 91(10):7810, 2002.

[5] M. A. Marioni, S. M. Allen, and R. C. O'Handley. Nonuniform twin-boundary motion in Ni–Mn–Ga single crystals. *Appl Phys Let*, 84(20):4071, May 2004.

[6] A. T. Zayak, P. Entel, J. Enkovaara, A. Ayuelaand, and R. M. Nieminen. First-principles investigations of homogeneous lattice-distortive strain and shuffles in $Ni_2MnGa$. *J. Phys.: Condens. Matter*, 15:159–164, 2003.

[7] J. Pons, V.A Chernenko, R. Santamarta, and E. Cesari. Long-period martensitic structures of Ni–Mn–Ga alloys studied by high-resolution transmission electron microscopy. *J. Appl. Phys.*, 97, 2005.

[8] J. Pons, V.A Chernenko, R. Santamarta, and E. Cesari. Crystal structure of martensitic phases in Ni–Mn–Ga shape memory alloys. *Acta mater.*, 48:3027–3038, 2000.

[9] V.A. Chernenko, V. L'Vov, E. Cesari, J. Pons, R. Portier, and S. Zagorodnyuk. ew aspects of structural and magnetic behaviour of martensites in Ni–Mn–Ga alloys. *Mater. Trans.*, 43(5):856, 2002.

[10] X. Jin, M. A. Marioni, D. Bono, S. M. Allen, R. C. O'Handley, and T. Y. Hsu. Empirical mapping of Ni–Mn–Ga properties with composition and valence electron concentration. *J. Appl. Phys.*, 91(10):8222 – 8224, 2002.

[11] J.R. Patel and M. Cohen. Criterion for the action of applied stress in the martensitic transformation. *Acta Met.*, 1:531–538, 1953.

[12] R. W. Overholser, M. Wuttig, and D. A. Neumann. Chemical ordering in Ni–Mn–Ga heusler alloys. *Scripta Mater.*, 40:1095–1102, 1999.

[13] The ILL Yellow Book, 2001.

[14] *Neutron News*, 3(3):29–37, 1992.

[15] L. E. Cross. Ferroelectric ceramics, mateirals and applications issues. *Ceramic Trans*, 68:15, 1996.

[16] S.E. Park, S. Wada, P.W. Rehrig, S. Liu, L.E. Cross, and T. R. Shrout. Crystallographic engineering in high-performace piezoelectric crystals. *SPIE Smart Structures and Materials*, 3675:2, 1999.

[17] R. C. O'Handley. *Modern Magnetic Materials*. John Wiley & Sons, Inc., New York, 2000.

[18] J. Van Humbeeck. Shape Memory Materials: A Material and a Technology. *Adv Eng Mater*, 3(11):837, 2001.

[19] R. D. James and M. Wuttig. Magnetostriction of martensite. *Phil. Mag. A*, 77:1273–1299, 1998.

[20] P. J. Brown, K. Ishida, R. Kainuma, T. Kanomata, K. U. Neumann, K. Oikawa, B. Ouladdiaf, and K. R. A. Ziebeck. Crystal structures and phase transitions in ferromagnetic shape memory alloys based on Co-Ni-Al and Co-Ni-Ga. *J Phys-Condes Mat*, 17(8):1301, 2005.

[21] F. Masdeu, J. Pons, C. Seguí, E. Cesari, and J. Dutkiewicz. Some features of Ni–Fe–Ga shape memory alloys under compression. *J Magn Magn Mater*, 290:816, April 2005.

[22] H.E. Karaca, B. Basaran, I. Karaman, Y.I. Chumlyakov, and H.J. Maier. Magnetic and conventional shape memory characteristics of $Co_{38}Ni_{33}Al_{29}$ and $Ni_2MnGa$ shape memory alloys. In *International Conference on Martensitic Transformations*, 2005.

[23] K. Ullakko. Large stroke and high-strength actuator materials for adaptive structures. *Third International Conference on Intelligent Materials*, Proceedings of SPIE Vol. 2779:505 – 510, 1996.

[24] K. Ullakko, P. G. Yakovenko, and V. G. Gavriljuk. New developments in actuator materials as reflected in magnetically controlled shape memory alloys and high-strength shape memory steels. *Smart Structures and Materials*, Proceedings of SPIE Vol. 2715:42 – 50, 1996.

[25] R. D. James and M. Wuttig. Alternative smart materials. *SPIE*, 2715:420–426, 1996.

[26] K. Ullakko, J. K. Huang, C. Kantner, R. C. O'Handley, and V. V. Kokorin. Large magnetic-field-induced strains in $Ni_2MnGa$ single crystals. *Appl. Phys. Lett.*, 69:1966 – 1968, 1996.

[27] S. J. Murray, M. Farinelli, C. Kantner, J. K. Huang, S. M. Allen, and R. C. O'Handley. Field-induced strain under load in Ni–Mn–Ga magnetic shape memory materials. *J. Appl. Phys.*, 83:7297–7299, 1998.

[28] S. J. Murray, M. Marioni, P. G. Tello, S. M. Allen, and R. C. O'Handley. Giant magnetic-field-induced strain in Ni–Mn–Ga crystals: experimental results and modeling. *J. Magn. Mag. Mat*, 226:945–947, 2001.

[29] A. Sozinov, A.A. Likhachev, N. Lanska, and K. Ullakko. Giant magnetic-field-induced strain in NiMnGa seven-layered martensitic phase. *Appl. Phy. Let.*, 80:1746, 2002.

[30] A. Sozinov, A. A. Likhachev, N. Lanska, K. Ullakko, and V. K. Lindroos. 10% magnetic-field-induced strain in Ni–Mn–Ga seven-layered martensite. *J. Phys. IV*, 112:955, 2003.

[31] P. Mullner, V.A. Chernenko, and G. Kostorz. Large cyclic magnetic-field-induced deformation in orthorhombic (14M) Ni–Mn–Ga martensite. *J. Appl. Phys.*, 95(3):1531, Feb 2004.

[32] P. J. Webster. Heusler alloys. *Contemp. Phys.*, 10:559–577, 1969.

[33] A. D. Boshko, A. N. Vasil'ev, V. V. Khovailo, I. E. Dikshtein, V. V. Koledov, S. M. Seletskii, A. A. Tulaikova, A. A. Cherechukin, V. G. Shavrov, and V. D. Bushel'nikov. Magnetic and structural phase transitions in the shape memory ferromagnetic alloys $Ni_{2+x}Mn_{1-x}Ga$. *J. Exp. and Theor. Phys.*, 88:954–962, 1999.

[34] I. K. Zasimchuk, V. V. Kokorin, V. V. Martynov, A. V. Tkachenko, and V. A. Chernenko. Crystal structure of martensite in Heusler alloy $Ni_2MnGa$. *Phys. Met. Metall.*, 69:104–108, 1990.

[35] V. V. Martynov and V. V. Kokorin. The crystal structure of thermally- and stress-induced martensites in $Ni_2MnGa$ single crystals. *J. Phys. III*, 2:739–749, 1992.

[36] K. Ullakko, J. K. Huang, V. V. Kokorin, and R. C. O'Handley. Magnetically controlled shape memory effect in $Ni_2MnGa$ intermetallics. *Scripta Mater.*, 36:1133–1138, 1997.

[37] M. Matsumoto, T. Tagaki, J. Tani, T. Kanomata, N. Muramatsu, and A. N. Vasil'ev. Phase transformations of Heulser type $\mathrm{Ni}_{2+x}\mathrm{Mn}_{1-x}\mathrm{Ga}_{(x=0\ \ 0.19)}$. *Mat. Sci. Eng. A*, 273 - 275:326 – 328, 1999.

[38] A. N. Vasil'ev, A. D. Boshko, V. V. Khovailo, I. E. Dikshtein, V. G. Shavrov, V. D. Bushel'nikov, M. Matsumoto, S. Suzuki, T. Takagi, and J. Tani. Structural and magnetic phase transitions in the shape memory alloys $\mathrm{Ni}_{2+x}\mathrm{Mn}_{1-x}\mathrm{Ga}$. *Phys. Rev. B*, 59:1113–1120, 1999.

[39] N. Lanska, O. Söderberg, A. Sozinov, Y. Ge, and K. Ullakko. Composition and temperature dependence of the crystal structure of Ni–Mn–Ga alloys. *J Appl Phys*, 95(12):8074, 2004.

[40] K. Ullakko. Magnetically controlled shape memory alloys: a new class of actuator materials. *J. Mat. Eng. Perf. (JMEPEG)*, 5:405 – 409, 1996.

[41] S. J. Murray, M. A. Marioni, A. M. Kukla, J. Robinson, R. C. O'Handley, and S. M. Allen. Large field-induced strain in single crystalline Ni–Mn–Ga ferromagnetic shape memory alloy. *J. Appl. Phys.*, 87:5774–5776, 2000.

[42] V. A. Chernenko, J. Pons, C. Seguí, and E. Cesari. Premartensitic phenomena and other phase transformations in Ni–Mn–Ga alloys studies by dynamical mechanical analysis and electron diffraction. *Acta Mat.*, 50:53–60, 2002.

[43] S. Y. Chu, A. Cramb, M. De Graef, D. Laughlin, and M. E. McHenry. The effect of field cooling and field orientation on the martensitic phase transformation of $\mathrm{Ni}_2\mathrm{MnGa}$ single crystal. *J. Appl. Phys.*, 87:0, 2000.

[44] R. Tickle, R. D. James, T. Shield, M. Wuttig, and V. V. Kokorin. Ferromagnetic shape memory in the NiMnGa system. *IEEE Magn. Trans.*, 35:4303–4310, 1999.

[45] R.D. James and K.F. Hane. Martensitic transformations and shape-memory materials. *Acta Mater.*, 48:197–222, 2000.

[46] M. Wuttig, K. Tsuchiya, L. Liu, , and R. James. Occurrence of ferromagnetic shape memory alloys. *J. Appl. Phys.*, 87:4707–4711, 2000.

[47] P. J. Ferreira and J. B. Vander Sande. Magnetic field effects on twin dislocations. *Scripta Mater.*, 41:117–123, 1999.

[48] R. C. O'Handley et al. Temperature dependence of field-induced strain in ferromagnetic shape memory alloys. Submitted for publication, 2005.

[49] U. Stuhr, P. Vorderwisch, V. V. Kokorin, and P. A. Lindgard. Premartensitic phenomena in the ferro- and paramagnetic phases of $Ni_2MnGa$. *Phys Rev B*, 56(22):14360, 1997.

[50] L. Mañosa, A. G. Comas, E. Obradó, and A. Planes. Premartensitic phase transformation in the $Ni_2MnGa$ shape memory alloy. *Mat. Sci. Eng. A*, 273-276:329–332, 1999.

[51] L. Mañosa, A. Gonzalez-Comas, E. Obradó, A. Planes, V. A. Chernenko, V. V. Kokorin, and E. Cesari. Anomalies related to the $TA_2$-phonon-mode condensation in the Heusler $Ni_2MnGa$ alloy. *Phys Rev B*, 55(17):11068, 1997.

[52] T. Castan, A. Planes, and A. Saxena. Modulated phases in multi-stage structural transformations. *Phys Rev B*, 67:134113, 2003.

[53] A. Zheludev, S. M. Shapiro, P. Wochner, A. Schwartz, M. Wall, and L. E. Tanner. Phonon anomaly, central peak, and microstructures in $Ni_2MnGa$. *Phys Rev B*, 51(17):11310, 1995.

[54] L. Mañosa, A. Planes, J. Zarestky, T. A. Lograsso, D. L. Schlagel, and C. Stassis. Phonon softening in Ni–Mn–Ga alloys. *Phys. Rev. B*, 64:024305, 2001.

[55] C. P. Henry, J. Feuchtwanger, D. Bono, M. A. Marioni, P. G. Tello, M. Richard, S. M. Allen, and R. C. O'Handley. AC performance and modelling of ferromagnetic shape memory actuators. In *Smart Structures and Materials*, volume Proceedings of SPIE Vol. 4333, pages 151–162, 2001.

[56] C. P. Henry. *Dynamic Actuation Properties of Ni–Mn–Ga Ferromagnetic Shape Memory Alloys.* PhD thesis, M.I.T., Cambridge, MA, May 2002.

[57] C. P. Henry, J. Feuchtwanger, D. Bono, M. A. Marioni, P. G. Tello, M. Richard, S. M. Allen, and R. C. O'Handley. AC performance and modeling of ferromagnetic shape memory actuators. In *Smart Structures and Materials 2001*, volume SPIE 4333, pages 151–161, Newport Beach, USA, 2001.

[58] B. W. Peterson, J. Feuchtwanger, J. M. Chambers, D.Bono, S. R. Hall, S.M. Allen, and R. C. O'Handley. Acoustic assisted, field-induced strain in ferromagnetic shape memory alloys. *J. Appl. Phys.*, 95:6963–6964, 2004.

[59] M. A. Marioni, R. C. O'Handley, and S. M. Allen. Pulsed magnetic field-induced actuation of ni–mn–ga single crystals. *Appl. Phys. Lett.*, 83:3966–3968, 2003.

[60] R. C. O'Handley. Model for strain and magnetization in magnetic shape-memory alloys. *J. Appl. Phys.*, 83:3263–3270, 1998.

[61] R. C. O'Handley, S. J. Murray, M. A. Marioni, H. Nembach, and S. M. Allen. Phenomenology of giant magnetic-field-induced strain in ferromagnetic shape-memory materials. *J. Appl. Phys.*, 87:4712–4717, 2000.

[62] A. Likhachev and K. Ullakko. The model development and experimental investigation of giant magneto-mechanical effects in Ni–Mn–Ga. *J. Magn. Mag. Mat*, 226:1541–1543, 2001.

[63] A. A. Likhachev and K. Ullakko. Quantitative model of large magnetostrain effect in ferromagnetic shape memory alloys. *Eur. Phys. J. B*, 14:263–267, 2000.

[64] D.I. Paul, J. Marquiss, and D. Quattrochi. Theory of magnetization: Twin boundary interaction in ferromagnetic shape memory alloys. *J Appl Phys*, 93:4561, 2003.

[65] D. I. Paul, R. C. O'Handley, and B. W. Peterson. Ferromagnetic shape memory alloys: Theory of interactions. *J Appl Phys*, 97:10M312, 2005.

[66] D.I. Paul, M. Richard, and R. C. O'Handley. Ferromagnetic shape memory alloys: Temperature dependence of twin boundary motion. Prepared for publication, 2005.

[67] D. L. Schlagel, Y. L. Wu, W. Zhang, and T. A. Lograsso. *J. Alloys Comp.*, 312:77, 2000.

[68] B. J. Wuensch. Private communication.

[69] V.V. Marynov, K. Enami, L. G. Khandros, S. Nenno, and A.V. Tkachenko. Structure of martensite phases formed in the 63.1 at% Ni–Al alloy during tension. *Phys. Met. metall.*, 55(5):982, 1983.

[70] D. Schryvers and L.E. Tanner. On the interpretation of high-resolution electron-microscopy images of premartensitic microstructures in the Ni–Al Beta-2 phase. *Ultramicroscopy*, 32(3):241, 1990.

[71] D. Schryvers. Martensitic and related transformatios in Ni–Al alloys. *J. Phys. IV*, 5(C2):225, 1995.

[72] D. L. Schlagel, Y. L. Wu, W. Zhang, and T. A. Lograsso. Chemical segregation during bulk single crystal preparation of Ni–Mn–Ga ferromagnetic shape memory alloy. *J. Alloys and Comp.*, 312:77–85, 2000.

[73] H. Lipson and H. Steeple. *Interpretation of X-Ray Powder Diffraction Patterns.* MacMillan and Co, 1970.

[74] A. Sozinov, A. A. Likhachev, N. Lanska, and K. Ullakko. Giant magnetic-field-induced strain in nimnga seven-layered martensitic phase. *Appl. Phys. Lett.*, 80:1746 – 1748, 2002.

[75] O. Heczko, L. Straka, and K. Ullakko. Relation between structure, magnetization process and magnetic shape memory effect of various martensites occurring in Ni-Mn-Ga alloys. *J. de Phys. IV*, 112:959–962, 2003.

[76] C. Seguí, V.A. Chernenko, J. Pons, and E. Cesari. Low-temperature-induced intermartensitic phase transformations in Ni–Mn–Ga single crystal. *J. Magn. Magn. Mater.*, 290:811–815, April 2005.

[77] V.A. Chernenko, E. Cesari, V. V. Khovailo, J. Pons, C. Seguí, and T. Tagaki. Intermartensitic phase transformations in Ni–Mn–Ga studied under magnetic field. *J. Magn. Magn. Mater.*, 290:871–873, April 2005.

[78] C. Seguí, V. A. Chernenko, J. Pons, and E. Cesari. Two-step martensitic transformation in Ni–Mn–Ga alloys. *J. de Phys. IV*, 112:903–906, October 2003.

[79] Z. H. Liu, G.H. Wu, W.H. Wang, J.L. Chen, L. Ao, and T.S. Chin. Effect of grind-induced internal stress on the intermartensitic transformation in the Ni–Mn–Ga alloy. *Acta Phys. Sin.*, 51(3):640–644, March 2002.

[80] J. Cui, Y. Chu, A. Ludwig, O. O. Famodu, J. Hattrick-Simpers, Y. Furuya, R.D. James, M. Wuttig, S. Thienhaus, and I. Takeuchi. Combinatorial search of thermoelastic shape-memory alloys with extermely small hysteresis width. Submitted for publication.

[81] C. M. Wayman. *Introduction to the Crystallography of Martensites.* The Macmillan Company, New York, 1964.

[82] M.T. Todinov, J.F. Knott, and M. Strangwood. An assessment of the influence of complex stress states on martensite start temperature. *Acta Mater.*, 44(12):4909–4915, 1996.

[83] E. S. Machlin and M. Cohen. *Trans Amer Inst Min (Metall) Engrs*, 191:746, 1951.

[84] J. W. Christian. *The Theory of Transformations in Metals and Alloys*, chapter 11. Pergamon Press, Oxford, 2 edition, 1975.

[85] J. Soltys. The magnetic properties of the Heusler alloy $Ni_2MnGa$. *Acta Phys. Polonica*, A46:383–384, 1974.

[86] J. Soltys. The effect of heat treatment on the atomic arrangement and the magnetic properties in $Ni_2MnGa$. *Acta Phys. Polonica*, A47:521–523, 1975.

[87] P. J. Webster, K. R. A. Ziebeck, M. S. Peak, and S.L. Town. Magnetic order and phase-transformations in $Ni_2MnGa$. *Phil. Mag. B*, 49:295, 1984.

[88] N. Glavatska, G. Mogylny, and S. Danilkin. Temperature dependence of lattice parameters in martensite and effect of the external magnetic field on martensite structure in $Ni_2MnGa$ studied in-situ with neutron diffraction. *Mater. Sci. Forum*, 443-444:397–400, 2004.

[89] R. A. Young, editor. *The Rietveld Method*. Internation Union of Crystallography Book Series. Oxford University Press, 1993.

[90] D. X. Chen, E. Pardo, and A. Sanchez. Demagnetizing factors for rectangular prisms. *IEEE T Magn*, 41(6):2077, 2005.

[91] M.H. Yoo. Plastic deofrmation of ordered intermetallic alloys: fundamental aspects. *Plasticity of Metals and Alloys — ISPMA 6 Key Engineering Materials*, 97-9:183, 1994.

[92] M. Yamaguchi, Y. Umakoshi, and T. Yamane. Plastic deofrmation of the intermetallic compound $Al_3Ti$. *Phil Mag A*, 55(3):301, 1987.

[93] D. P. Pope and J.L. Garen. The temperature dependence of the long-rang order parameter of $Ni_3Al$. *J Appl Cryst*, 10:14, 1977.

[94] B. Bhattacharya and R. K. Ray. Deformation behavior of a $Ni_3Al(B,Zr)$ alloy during cold rolling, part 1: Changes in order and structure. *Met Trans A*, 31A:3001, 2000.

[95] R. C. O'Handley, D. I. Paul, M. Marioni, C. P. Henry, M. Richard, P. G. Tello, and S. M. Allen. Micromagnetic and micromechanics of Ni–Mn–Ga actuation. *J Phys IV France*, 112:973, 2003.

[96] D.B. Williams and C.B. Carter. *Transmisson Electron Microscopy.* Plenum Press, 1996.

[97] P. Hirch, A. Howie, R.B. Nicholson, D.W. Pashley, and M.J. Whelan. *Electron Microscopy of Thin Crystals.* Robert E. Krieger Publishing, 2nd edition edition, 1977.

[98] M. F. Ashby and L. M. Brown. Diffraction contrast from spherically symmetrical coherency strains. *Phil. Mag.*, 8:1083, 1963.

[99] M. F. Ashby and L. M. Brown. On diffraction contrast from inclusions. *Phil. Mag.*, 8:1649, 1963.

[100] J.L. Murray. *ASM Handbook: Alloy Phase Diagrams (Volume 3)*, chapter Ni–Ti Binary Phase Diagram. ASM International, 1993.

[101] T. A. Lograsso and D. L. Schlagel. MURI review presentation.

[102] B. Peterson and J. Simon. Unpublished research. 2005.

[103] R. W. Hertzberg. *Deformation and Fracture Mechanics of Engineering Materials.* John Wiley and Sons, 4th edition edition, 1996.

[104] R. E. Reed-Hill and R. Abbaschian. *Physical Metallurgy Principles.* PWS Publishing Company, Boston, 3 edition, 1994.

[105] M. Stipcich, L. Mañosa, A. Planes, M. Morin, J. Zarestky, T. A. Lograsso, and C. Stassis. Elastic constants of Ni–Mn–Ga magnetic shape memory alloys. *Phys Rev B*, 70:054115, 2004.